5-24-2012

Trace Element Cycling during Iron(II)-activated Recrystallization of Iron(III) Oxide Minerals

Andrew Frierdich
Washington University in St. Louis

WASHINGTON UNIVERSITY IN ST. LOUIS

Department of Earth and Planetary Sciences

Dissertation Examination Committee:
Jeffrey G. Catalano, Chair
David A. Fike
John D. Fortner
Daniel E. Giammar
Frédéric Moynier
Jill D. Pasteris

Trace Element Cycling during Iron(II)-activated Recrystallization of Iron(III) Oxide Minerals

by

Andrew James Frierdich

A dissertation presented to the
Graduate School of Arts and Sciences
of Washington University in
partial fulfillment of the
requirements for the degree
of Doctor of Philosophy

May 2012

Saint Louis, Missouri

ABSTRACT OF THE DISSERTATION

TRACE ELEMENT CYCLING DURING IRON(II)-ACTIVATED RECRYSTALLIZATION OF IRON(III) OXIDE MINERALS

by

Andrew J. Frierdich

Doctor of Philosophy in Earth and Planetary Sciences

Washington University in St. Louis, 2012

Professor Jeffrey G. Catalano, Chairperson

Biogeochemical iron cycling initiates secondary abiotic reactions between aqueous Fe(II) and Fe(III) oxide minerals, which results in dynamic recrystallization via simultaneous Fe(II) oxidative adsorption and Fe(III) reductive dissolution. Fe(III) oxide minerals are abundant in soils, sediments, and groundwater systems, and often control the fate and transport of trace elements. A robust understanding of their reactivity with Fe(II) and how associated trace elements are affected during Fe(II)-activated recrystallization is required to predict the effect of biogeochemical processes on contaminant fate and micronutrient availability.

The main objective of the research presented in this dissertation is to characterize how Fe(II)-activated recrystallization of iron oxide minerals affects the cycling and fate of associated trace elements. The specific foci are to: 1) obtain a general description of redox-inactive trace element cycling through iron oxide minerals, 2) examine the chemical controls on net trace element release from goethite and hematite, 3) explore surface passivation and trace element release inhibition during Fe(II)-activated recrystallization of iron oxides containing insoluble elements, and 4) determine the fate

of redox-sensitive metals that are structurally incorporated in iron oxides during reaction with Fe(II).

Compositional measurements and spectroscopic results show that Ni is cycled through the minerals goethite and hematite during Fe(II)-activated recrystallization. Adsorbed Ni becomes progressively incorporated into the minerals while Ni pre-incorporated into iron oxides is released to solution. The kinetics of Ni and Zn release to solution are primarily controlled by the amount of Fe(II) sorption. Furthermore, these structurally-incorporated trace elements are mobilized from iron oxides into fluids without net iron reduction. The Fe(II)-activated release of Ni and Zn from goethite and hematite is substantially inhibited when the insoluble elements Al, Cr, and Sn are co-substituted within the mineral structures. Incorporation of Al into goethite substantially decreases the amount of Fe atom exchange between aqueous Fe(II) and Fe(III) in the mineral and, consequently, the amount of Ni release from the structure. This implies that the mechanism for trace element release inhibition, following substitution of insoluble elements, is a decrease in the amount of mineral recrystallization. Reaction of Cu(II)-, Co(III)-, and Mn(III,IV)-substituted goethite and hematite with Fe(II) results in the reduction and release of Cu, Co, and Mn to solution.

This work suggests that important proxies for ocean composition on the early Earth may be invalid, identifies new processes that affect micronutrient availability, contaminant transport, and the distribution of redox-inactive trace elements in natural and engineered systems, and shows that redox-sensitive elements are susceptible to reduction and release to solution despite being incorporated within a stable mineral structure. Furthermore, this work illustrates that naturally occurring iron oxides that contain

insoluble impurities are less susceptible to Fe(II)-activated recrystallization and exhibit a greater retention of trace elements and contaminants than pure mineral phases. These discoveries demonstrate that, in the presence of Fe(II), iron oxide minerals are not passive surfaces that merely adsorb ions but rather their entire volume equilibrates with fluids. Such advances expand our view on the potential impacts of iron cycling on the fate of trace elements and contaminants.

ACKNOWLEDGEMENTS

This dissertation was made possible through a combination of human and financial support. I am deeply indebted to my family, friends, and colleagues who have inspired me through my personal and professional life. I am especially grateful to my parents who insisted that I attend college and provided the financial means to do so, and to my wife who, at times, has sacrificed her own desires so that I can pursue mine. I would also like to thank my adviser, Jeff Catalano, who has been supportive of my research interests, introduced me to cutting-edge synchrotron techniques, and provided valuable advice, discussion, and support with research and publication. It has been an honor to work with him. Lastly, I wish to thank my committee members, my research group members, and the many others who have provided experimental assistance and valuable insight.

Financial support was provided primarily by the U.S. National Science Foundation through Grant EAR-0818354 and the American Chemical Society Petroleum Research Fund through Grant 48302-G2. I am also grateful for financial support from Washington University in the way of tuition waivers and teaching opportunities, and to my country for supporting basic science and an astonishing national laboratory system that has been critical to the success of my research.

TABLE OF CONTENTS

LIST OF TABLES

Chapter 2

Chapter 3

Chapter 4

Chapter 5

LIST OF FIGURES

Chapter 1

Chapter 2

Chapter 3

Chapter 4

Chapter 5

CHAPTER 1

INTRODUCTION

Biogeochemical Iron Cycling? Not in My Backyard!

Around 4:40 am on the morning of April 18th, 2008, residents of southern Illinois were awoken as the Wabash Valley Fault released an earthquake that registered 5.2 on the Richter scale. While damage to infrastructure was minimal, citizens within a one block area of Belleville, IL soon began to notice water seeping into their yards and basements. This emerging groundwater was accompanied by the deposition of an orange-colored material that alarmed residents and city officials who worried that the water was contaminated (Girresch, 2008). The Illinois Department of Natural Resources suggested that the water was draining from an abandoned coal mine, was not dangerous, and that the orange color was due to iron (Girresch, 2008). A series of French drains were later constructed to redirect the water into an existing paved stormwater ditch where it has been discharging and depositing iron minerals ever since (Figure 1-1). In the end, the emergence of an iron spring in Belleville, IL was more of a nuisance to residents than an environmental hazard. However, this scenario illustrates that one of the Earth's oldest and most important biogeochemical cycles is not limited to exotic, remote field sites or to reports in the scientific literature but rather can occur literally in one's own backyard.

Background

Iron is the 4th most abundant element and most abundant transition metal in the Earth's crust (Greenwood and Earnshaw, 1984). It is an essential nutrient for microorganisms, plants, and animals, limits ocean productivity (Boyd and Ellwood, 2010), and consequently, regulates atmospheric carbon dioxide levels and global climate (Martin, 1990). At near-surface conditions on Earth it exists primarily as Fe(III) and tends to occur as insoluble oxide, hydroxide, and oxyhydroxide minerals, here on collectively termed iron oxides (Cornell and Schwertmann, 2003). These minerals are ubiquitous in soils (Schwertmann and Taylor, 1989), freshwater and marine sediments (van der Zee et al., 2003), and also commonly occur as cements in clastic rocks (Boggs Jr., 2006), as coatings on the seafloor (Templeton et al., 2009), and as major ore bodies (Maynard, 1983). Iron oxide minerals are widely recognized as natural sorbents of nutrients and contaminants (Stumm, 1992; Brown et al., 1999), and as sinks for structurally compatible trace elements (Cornell and Schwertmann, 2003).

Iron oxides are generally stable at the Earth's surface. However, anoxia may occur in aqueous environments when oxygen diffusion is slower than the rate of consumption by bacteria, which can lead to partial or complete dissolution of iron oxides via microbial dissimilatory Fe(III) reduction (DIR) (Weber et al., 2006). A wide phylogenetic diversity of microorganisms are capable of DIR (Lovely, 2000), and it is now widely recognized that microbial activity is the dominant control on iron redox chemistry in most environments (Weber et al., 2006). Microbially-produced Fe(II) resulting from DIR is typically water soluble and mobile but does form Fe(II)-bearing minerals such as magnetite, siderite, and green rust when high concentrations of Fe(II),

carbonate, and phosphate are present at circumneutral to alkaline conditions (Zachara et al., 2002). Both abiotic (Millero, 1989) and biological (Emerson, 2000) Fe(II) oxidation occur readily in the presence of oxygen, resulting in the precipitation of Fe(III) oxide minerals. DIR, Fe(II) oxidation, or both, result in systems where aqueous Fe(II) and Fe(III) oxides coexist. Recent advances in spectroscopic techniques (e.g., Mössbauer spectroscopy) and high precision mass spectrometry are revealing new details about the abiotic interactions between these species.

Electron Transfer and Atom Exchange between Aqueous Fe(II) and Fe(III) Oxides

Aqueous Fe(II) readily sorbs onto iron oxide minerals at circumneutral pH (Coughlin and Stone, 1995; Strathmann and Stone, 2003). The uptake mechanism, however, involves more than just surface adsorption but also entails electron transfer into the solid (Jeon et al., 2001; Jeon et al., 2003a; Williams and Scherer, 2004; Larese-Casanova and Scherer, 2007). Studies of Fe(II) sorption on hematite have reported an unrecoverable Fe(II) fraction following a mild acid extraction (Jeon et al., 2001; Jeon et al., 2003a). This was attributed to interfacial electron transfer between aqueous Fe(II) and hematite resulting in amorphous ferric oxide precipitation and magnetite domains within the solid, although the proposed products were not actually observed. More recent work, using the ^{57}Fe specificity of Mössbauer spectroscopy, has unambiguously shown that sorption of Fe(II) on numerous iron oxide phases results in electron transfer to the solid, and that the newly formed Fe(III) is in a material that is structurally similar to the original mineral phase rather than occurring in a distinct form (Williams and Scherer, 2004; Larese-Casanova and Scherer, 2007).

Additional insight into Fe(II)-Fe(III) electron transfer was obtained through reaction of Fe(II) with ^{55}Fe-labeled iron oxides, resulting in the release of ^{55}Fe(II) to solution (Pedersen et al., 2005). Such release demonstrates electron transfer and atom exchange (ETAE) between aqueous Fe(II) and ^{55}Fe(III) in the solid. The amount of atom exchange varied among mineral phases, with complete recrystallization of ferrihydrite and poorly-crystalline lepidocrocite, moderate exchange for goethite, and no observable exchange for hematite. Ferrihydrite and lepidocrocite were transformed into more crystalline phases during the reaction (Pedersen et al., 2005). Later work has revealed that reaction of ^{57}Fe-enriched Fe(II) with goethite results in complete atom exchange and no phase transformation (Handler et al., 2009; Beard et al., 2010). The proposed mechanism for Fe(II)-Fe(III) ETAE involves simultaneous Fe(II) oxidative adsorption coupled with Fe(III) reductive dissolution (Larese-Casanova and Scherer, 2007; Yanina and Rosso, 2008; Handler et al., 2009; Mikutta et al., 2009; Beard et al., 2010; Rosso et al., 2010), with electron conduction likely occurring through the bulk structure (Yanina and Rosso, 2008; Rosso et al., 2010). For example, the driving force for electron conduction during Fe(II)-Fe(III) ETAE on hematite single crystals results from potential differences between specific crystallographic surfaces (Yanina and Rosso, 2008). A similar mechanism likely operates during the Fe(II)-activated recrystallization of other iron oxide minerals (Handler et al., 2009). The discovery of Fe(II)-Fe(III) ETAE has resulted in a paradigm shift in our understanding of the potential impacts of iron cycling on other environmental processes.

Consequences of Fe(II)-Fe(III) Electron Transfer and Atom Exchange

Reaction of aqueous Fe(II) with Fe(III) oxides has numerous geochemical and environmental consequences, such as affecting mineral transformations, iron isotope fractionation, and contaminant reduction. The role of Fe(II) in catalyzing the conversion of ferrihydrite into more crystalline iron oxides, for example, has been widely documented (Hansel et al., 2003; Hansel et al., 2004; Hansel et al., 2005; Pedersen et al., 2005) Such Fe(II)-catalyzed phase transformations lead to the repartitioning of associated trace elements by release to solution and incorporation into newly formed minerals (Fredrickson et al., 2001; Boland et al., 2011).

Another result of Fe(II)-Fe(III) ETAE is iron isotope fractionation between aqueous Fe(II) and Fe(III) oxide minerals. Such processes are indicators of biogeochemical iron cycling as some of the largest natural fractionations of stable iron isotopes occur during partial DIR of iron oxide minerals (Johnson et al., 2004). Microbially-produced Fe(II) during DIR is depleted in heavy iron isotopes (Icopini et al., 2004). The fractionation mechanism, however, is not from biologically-selective Fe(III) reduction but instead results from abiotic Fe(II)-Fe(III) ETAE as such recrystallization allows equilibrium iron isotope partitioning to occur (Crosby et al., 2005; Crosby et al., 2007). Consequently, iron isotope fractionation factors for aqueous Fe(II) and iron oxide minerals can be determined (Beard et al., 2010; Wu et al., 2011) thus providing constraints for interpreting the iron isotope variations in modern sediments and Precambrian marine sedimentary rocks (Johnson and Beard, 2006; Johnson et al., 2008; Wu et al., 2012).

Fe(II)-activated recrystallization of iron oxides also has implications for redox-sensitive species associated with these minerals. The Fe(II)-Fe(III) ETAE process described above is chemically catalytic, i.e., no net Fe oxidation or reduction occurs. When it occurs in the presence of redox-sensitive elements, however, Fe(II) may serve as a powerful reductant. A wide range of inorganic species and organic functional groups are reduced abiotically by Fe(II) on iron oxide surfaces (Haderlein and Pecher, 1999); examples include but are not limited to U(VI) (Charlet et al., 1998; Liger et al., 1999), Cr(VI) (Buerge and Hug, 1999), Pu(IV) (Felmy et al., 2011), halogenated hydrocarbons (Elsner et al., 2004), and nitroaromatics (Klausen et al., 1995; Charlet et al., 1998). While Fe(II)-mediated contaminant reduction has been examined extensively, few studies have explored the effect of Fe(II) on redox-inactive elements (e.g., Ni and Zn) associated with iron oxides or redox-sensitive elements (e.g., Cu, Co, Mn) structurally incorporated into iron oxides. Furthermore, naturally occurring iron oxides often contain impurities (e.g., Al, Cr, Sn); how such impurities affect mineral reactivity relative to pure iron oxide phases used in laboratory studies remains largely unknown.

Effect of Fe(II)-activated Recrystallization on the Fate of Trace Elements

There is currently a large knowledge gap in our understanding of how Fe(II)-Fe(III) ETAE affects the fate of trace elements associated with iron oxide minerals. The existing reports of how Fe(II) affects the speciation of redox-inactive trace elements sorbed on iron oxides are limited and contradictory and, to this author's knowledge, no prior study has examined the effect of Fe(II) on the fate of trace elements structurally incorporated within stable iron oxide phases, e.g., goethite and hematite. Zn(II)

incorporation into goethite has been postulated following microbial iron reduction of goethite containing adsorbed Zn (Cooper et al., 2000; Cooper et al., 2005); no incorporation was apparent in the absence of Fe(II) production. Similar abiotic experiments examining divalent metal [Me(II)] sorption onto goethite also suggest that Fe(II) promotes the incorporation of trace elements (Coughlin and Stone, 1995), but similar studies using hematite did not observe any Me(II) incorporation (Jeon et al., 2003b). These conflicting results may reflect differences in the extent of Fe(II)-activated recrystallization of goethite and hematite (Pedersen et al., 2005; Handler et al., 2009; Beard et al., 2010; Wu et al., 2010). However, in all studies the Me(II) species were determined using acid extractions which can cause partial surface dissolution, thereby releasing to solution metals that are incorporated in the uppermost surface layers, erasing any evidence of actual incorporation. The impact of Fe(II)-Fe(III) ETAE on the fate of redox-inactive elements is thus unclear.

An unknown variable that may affect Fe(II)-Fe(III) ETAE and, consequently the fate of trace elements, is how the reactivity of naturally occurring iron oxides may differ from those typically used in laboratory studies. To date, all studies examining Fe(II)-Fe(III) ETAE have utilized pure iron oxide phases (Williams and Scherer, 2004; Pedersen et al., 2005; Larese-Casanova and Scherer, 2007; Yanina and Rosso, 2008; Handler et al., 2009; Mikutta et al., 2009; Beard et al., 2010). Naturally occurring iron oxides, however, often contain impurities such as Al, Cr, and Sn (Singh and Gilkes, 1992; Trolard et al., 1995; Cornell and Schwertmann, 2003) which may alter iron oxide reactivity. For example, Al incorporation into iron oxides inhibits abiotic reductive dissolution (Torrent et al., 1987), microbial iron reduction (Bousserrhine et al., 1999), the

Fe(II)-induced transformation of ferrihydrite (Hansel et al., 2011), and contaminant reduction by magnetite (Jentzsch et al., 2007). The effect of insoluble substituting elements, such as Al, Cr, and Sn, on Fe(II)-Fe(III) ETAE or on other associated trace elements is unknown.

Lastly, the effect of Fe(II) on redox-sensitive metals susceptible to reduction may be quite different from its affect on redox-inactive species. Several redox-sensitive metals are known to substitute within iron oxide minerals, e.g., Cu(II) (Cornell and Giovanoli, 1988; Manceau et al., 2000), Co(III) (Cornell and Giovanoli, 1989; Pozas et al., 2004), and Mn(III,IV) (Cornell and Giovanoli, 1987; Singh et al., 2000; Singh et al., 2002). The reduction of Cu(II) by Fe(II) is known but only for the homogeneous reaction of the aqueous species (Biddle, 1901; Matocha et al., 2005) and reaction of aqueous Cu(II) with structural Fe(II)-containing green rust (O'Loughlin et al., 2003). Such reactions may control the fate of Cu in the environment and initiate the formation of native Cu deposits (Biddle, 1901; Cornwall, 1956). Similarly, the reduction of Mn(III,IV) is limited to studies of Mn oxide minerals. Such reactions can elevate Mn(II) concentrations in groundwater and separate Mn from Fe in sediments (Postma, 1985; Postma and Appelo, 2000). The reduction of Co(III) by Fe(II) is also uncertain. Microbial iron reduction of Co(III)-substituted goethite results in the release of Co(II) to solution (Bousserrhine et al., 1999; Zachara et al., 2001); microbially-mediated co-reduction of Co(III) and Fe(III) was assumed in these studies without considering the potential for Co reduction by Fe(II). Although Cu and Mn reduction by Fe(II) in aqueous solution and at minerals surfaces is recognized and some evidence suggests that structural Co may be reducible by Fe(II), the

effect of Fe(II) on Cu, Mn, and Co incorporated in iron oxide minerals is largely unexplored.

The discovery of interfacial ETAE between aqueous Fe(II) and Fe(III) oxides suggests that these minerals should no longer be considered as passive surfaces that merely adsorb ions but, instead, the entire volumes of these minerals may equilibrate with fluids and their dissolved species in the presence of Fe(II). Consequently, such reactions should substantially impact the partitioning behavior of associated trace elements and affect their speciation and mobility in the environment. A robust understanding of iron oxide mineral reactivity with Fe(II) and how associated trace elements are affected during Fe(II)-activated recrystallization is required to predict the effect of biogeochemical processes on contaminant fate and micronutrient availability.

Research Objectives

The main objective of the research presented in this dissertation is to characterize how Fe(II)-activated recrystallization of iron oxide minerals affects the cycling and fate of associated trace elements. Specific foci are to:

1) Obtain a general description of redox-inactive trace element cycling through iron oxide minerals during reaction with Fe(II).

2) Determine the chemical controls affecting net trace element release during Fe(II)-activated recrystallization of goethite and hematite.

3) Explore surface passivation and trace element release inhibition during Fe(II)-Fe(III) ETAE between aqueous Fe(II) and iron oxides containing insoluble elements.

4) Identify the fate of redox-sensitive metals that are structurally incorporated into goethite and hematite during reaction with Fe(II).

Figure 1-1. (A) In Belleville, IL, emerging groundwater is collected by French drains and discharged from a 6 inch pipe into a storm-water ditch where the precipitation of orange-colored iron oxide minerals is apparent. (B) The water flows and deposits minerals for about 0.5 miles through residential areas before entering a nearby creek.

REFERENCES

Beard, B.L., Handler, R.M., Scherer, M.M., Wu, L., Czaja, A.D., Heimann, A., Johnson, C.M., (2010). Iron isotope fractionation between aqueous ferrous iron and goethite. *Earth Planet. Sc. Lett.* **295**, 241–250.

Biddle, H.C., (1901). The deposition of copper by solutions of ferrous salts. *J. Geol.* **9**, 430-436.

Boggs Jr., S., 2006. *Principles of sedimentology and stratigraphy*, 4th ed. Pearson Prentice Hall, Upper Saddle River.

Boland, D.D., Collins, R.N., Payne, T.E., Waite, T.D., (2011). Effect of amorphous Fe(III) oxide transformation on the Fe(II)-mediated reduction of U(VI). *Environ. Sci. Technol.* **45**, 1327-1333.

Bousserrhine, N., Gasser, U.G., Jeanroy, E., Berthelin, J., (1999). Bacterial and chemical reductive dissolution of Mn-, Co-, Cr-, and Al-substituted goethites. *Geomicrobiol. J.* **16**, 245-258.

Boyd, P.W., Ellwood, M.J., (2010). the biogeochemical cycle of iron in the ocean. *Nat. Geosci.* **3**, 675-682.

Brown, G.E., Jr., Henrich, V.E., Casey, W.H., Clark, D.L., Eggleston, C., Felmy, A., Goodman, D.W., Gratzel, M., Maciel, G., McCarthy, M.I., Nealson, K.H., Sverjensky, D.A., Toney, M.J., Zachara, J.M., (1999). Metal oxide surfaces and their interaction with aqueous solutions and microbial organisms. *Chem. Rev.* **99**, 77-174.

Buerge, I.J., Hug, S., J., (1999). Influence of mineral surfaces on chromium(VI) reduction by iron(II). *Environ. Sci. Technol.* **33**, 4285–4291.

Charlet, L., Silvester, E., Liger, E., (1998). N-compound and actinide immobilisation in surficial fluids by Fe(II): The surface $Fe^{III}OFe^{II}OH^{o}$ species, as major reductant. *Chem. Geol.* **151**, 85-93.

Cooper, C.D., Picardal, F., Rivera, J., Talbot, C., (2000). Zinc immobilization and magnetite formation via ferric oxide reduction by *Shewanella* putrefaciens 200. *Environ. Sci. Technol.* **34**, 100-106.

Cooper, C.D., Neal, A.L., Kukkadapu, R.K., Brewe, D., Coby, A., Picardal, F.W., (2005). Effects of sediment iron mineral composition on microbially mediated changes in divalent metal speciation: Importance of ferrihydrite. *Geochim. Cosmochim. Acta* **69**, 1739–1754.

Cornell, R.M., Giovanoli, R., (1987). Effect of manganese on the transformation of ferrihydrite into goethite and jacobsite in alkaline media. *Clay. Clay Miner.* **35**, 11-20.

Cornell, R.M., Giovanoli, R., (1988). The influence of copper on the transformation of ferrihydrite ($5Fe_2O_3$ x $9H_2O$) into crystalline products in alkaline media. *Polyhedron* **7**, 385-391.

Cornell, R.M., Giovanoli, R., (1989). Effect of cobalt on the formation of crystalline iron oxides from ferrihydrite in alkaline media. *Clay. Clay Miner.* **37**, 65-70.

Cornell, R.M., Schwertmann, U., 2003. *The iron oxides: Structure, properties, reactions, occurrences and uses*, 2nd ed. Wiley-VCH Verlag GmbH & Co. KGaA, Weinheim.

Cornwall, H.R., (1956). A summary of ideas on the origin of native copper deposits. *Econ. Geol.* **51**, 615-631.

Coughlin, B.R., Stone, A.T., (1995). Nonreversible adsorption of divalent metal ions (Mn(II), Co(II), Ni(II), Cu(II), and Pb(II)) onto goethite: Effects of acidification, Fe(II) addition, and picolinic acid addition. *Environ. Sci. Technol.* **29**, 2445–2455.

Crosby, H.A., Johnson, C.M., Roden, E.E., Beard, B.L., (2005). Coupled Fe(II)-Fe(III) electron and atom exchange as a mechanism for Fe isotope fractionation during dissimilatory iron oxide reduction. *Environ. Sci. Technol.* **39**, 6698–6704.

Crosby, H.A., Roden, E.E., Johnson, C.M., Beard, B.L., (2007). The mechanisms of iron isotope fractionation produced during dissimilatory Fe(III) reduction by *Shewanella putrefaciens* and *Geobacter sulfurreducens*. *Geobiology* **5**, 169–189.

Elsner, M., Schwarzenbach, R.P., Haderlein, S., (2004). Reactivity of Fe(II)-bearing minerals toward reductive transformation of organic contaminants. *Environ. Sci. Technol.* **38**, 799–807.

Emerson, D., 2000. Microbial oxidation of Fe(II) and Mn(II) at circumneutral pH, in: Lovley, D.R. (Ed.), *Environmental metal-microbe interactions*. ASM Press, Washington, D.C., pp. 31-52.

Felmy, A.R., Moore, D.A., Rosso, K.M., Qafoku, O., Rai, D., Buck, E.C., Ilton, E.S., (2011). Heterogeneous Reduction of PuO_2 with Fe(II): Importance of the Fe(III) Reaction Product. *Environ. Sci. Technol.* **45**, 3952–3958.

Fredrickson, J.K., Zachara, J.M., Kukkadapu, R.K., Gorby, Y.A., Smith, S.C., Brown, C.F., (2001). Biotransformation of Ni-substituted hydrous ferric oxide by an Fe(III)-reducing bacterium. *Environ. Sci. Technol.* **35**, 703-712.

Girresch, L., (2008). Orange water caused by iron. *Belleville News Democrat*, 1A.

Greenwood, N.N., Earnshaw, A., 1984. *Chemistry of the elements*, 1st ed. Pergamon Press, Oxford.

Haderlein, S., Pecher, K., 1999. Pollutant reduction in heterogeneous Fe(II)-Fe(III) systems, in: Sparks, D.L., Grundl, T.J. (Eds.), *Mineral-water interfacial reactions: Kinetics and mechanisms*. American Chemical Society, Washington DC, pp. 342-357.

Handler, R.M., Beard, B.L., Johnson, C.M., Scherer, M.M., (2009). Atom exchange between aqueous Fe(II) and goethite: An Fe isotope tracer study. *Environ. Sci. Technol.* **43**, 1102–1107.

Hansel, C.M., Benner, S.G., Neiss, J., Dohnalkova, A., Kukkadapu, R.K., Fendorf, S., (2003). Secondary mineralization pathways induced by dissimilatory iron reduction of ferrihydrite under advective flow. *Geochim. Cosmochim. Acta* **67**, 2977-2992.

Hansel, C.M., Benner, S.G., Nico, P., Fendorf, S., (2004). Structural constraints of ferric (hydr)oxides on dissimilatory iron reduction and the fate of Fe(II). *Geochim. Cosmochim. Acta* **68**, 3217-3229.

Hansel, C.M., Benner, S.G., Fendorf, S., (2005). Competing Fe(II)-induced mineralization pathways of ferrihydrite. *Environ. Sci. Technol.* **39**, 7147–7153.

Hansel, C.M., Learman, D.R., Lentini, C.J., Ekstrom, E.B., (2011). Effect of adsorbed and substituted Al on Fe(II)-induced mineralization pathways of ferrihydrite. *Geochim. Cosmochim. Acta* **75**, 4653–4666.

Icopini, G.A., Anbar, A.D., Ruebush, S.S., Tien, M., Brantley, S.L., (2004). Iron isotope fractionation during microbial reduction of iron: The importance of adsorption. *Geology* **32**, 205-208.

Jentzsch, T.L., Chun, C.L., Gabor, R.S., Penn, R.L., (2007). Influence of aluminum substitution on the reactivity of magnetite nanoparticles. *J. Phys. Chem. C* **111**, 10247-10253.

Jeon, B.-H., Dempsey, B.A., Burgos, W.D., Royer, R.A., (2001). Reactions of ferrous iron with hematite. *Colloids Surf. A* **191**, 41-55.

Jeon, B.-H., Dempsey, B.A., Burgos, W.D., (2003a). Kinetics and mechanisms for reactions of Fe(II) with iron(III) oxides. *Environ. Sci. Technol.* **37**, 3309-3315.

Jeon, B.-H., Dempsey, B.A., Burgos, W.D., Royer, R.A., (2003b). Sorption kinetics of Fe(II), Zn(II), Co(II), Ni(II), Cd(II), and Fe(II)/Me(II) onto hematite. *Water Res.* **37**, 4135–4142.

Johnson, C.M., Beard, B.L., Roden, E.E., Newman, D.K., Nealson, K.H., (2004). Isotopic constraints on biogeochemical cycling of Fe. *Rev. Mineral. Geochem.* **55**, 359-408.

Johnson, C.M., Beard, B.L., (2006). Fe isotopes: An emerging technique for understanding modern and ancient biogeochemical cycles. *GSA Today* **16**, 4-10.

Johnson, C.M., Beard, B.L., Klein, C., Beukes, N.J., Roden, E.E., (2008). Iron isotopes constrain biologic and abiologic processes in banded iron formation genesis. *Geochim. Cosmochim. Acta* **72**, 151–169.

Klausen, J., Trober, S.P., Haderlein, S.B., Schwarzenbach, R.P., (1995). Reduction of substituted nitrobenzenes by Fe(II) in aqueous mineral suspensions. *Environ. Sci. Technol.* **29**, 2396-2404.

Larese-Casanova, P., Scherer, M.M., (2007). Fe(II) sorption on hematite: New insights based on spectroscopic measurements. *Environ. Sci. Technol.* **41**, 471–477.

Liger, E., Charlet, L., Cappellen, P.V., (1999). Surface catalysis of uranium(VI) reduction by iron(II). *Geochim. Cosmochim. Acta* **63**, 2939–2955.

Lovely, D.R., 2000. Fe(III) and Mn(IV) reduction, in: Lovley, D.R. (Ed.), *Environmental metal-microbe interactions*. ASM Press, Washington, D.C., pp. 3-30.

Manceau, A., Schlegel, M.L., Musso, M., Sole, V.A., Gauthier, C., Petit, P.E., Trolard, F., (2000). Crystal chemistry of trace elements in natural and synthetic goethite. *Geochim. Cosmochim. Acta* **64**, 3643-3661.

Martin, J.H., (1990). Glacial-interglacial CO_2 change: The iron hypothesis. *Paleooceanogr.* **5**, 1-13.

Matocha, C.J., Karathanasis, A.D., Rakshit, S., Wagner, K.M., (2005). Reduction of copper(II) by iron(II). *J. Environ. Qual.* **34**, 1539-1546.

Maynard, J.B., 1983. *Geochemistry of sedimentary ore deposits*. Springer-Verlag, New York.

Mikutta, C., Wiederhold, J.G., Cirpka, O.A., Hofstetter, T.B., Bourdon, B., Gunten, U.V., (2009). Iron isotope fractionation and atom exchange during sorption of ferrous iron to mineral surfaces. *Geochim. Cosmochim. Acta* **73**, 1795–1812.

Millero, F.J., (1989). Effect of ionic interactions on the oxidation of Fe(II) and Cu(I) in natural waters. *Mar. Chem.* **28**, 1-18.

O'Loughlin, E.J., Kelly, S.D., Kemner, K.M., Csencsits, R., Cook, R.E., (2003). Reduction of Ag^{I}, Au^{III}, Cu^{II}, and Hg^{II} by Fe^{II}/Fe^{III} hydroxysulfate green rust. *Chemosphere* **53**, 437–446.

Pedersen, H.D., Postma, D., Jakobsen, R., Larsen, O., (2005). Fast transformation of iron oxyhydroxides by the catalytic action of aqueous Fe(II). *Geochim. Cosmochim. Acta* **69**, 3967–3977.

Postma, D., (1985). Concentration of Mn and separation from Fe in sediments-I. Kinetics and stoichiometry of the reaction between biiessite and dissolved Fe(II) at 10°C. *Geochim. Cosmochim. Acta* **49**, 1023-1033.

Postma, D., Appelo, C.A.J., (2000). Reduction of Mn-oxides by ferrous iron in a flow system: Column experiment and reactive transport modeling. *Geochim. Cosmochim. Acta* **64**, 1237–1247.

Pozas, R., Rojas, T.C., Ocaña, M., Serna, C.J., (2004). The nature of Co in synthetic Co-substituted goethites. *Clay. Clay Miner.* **52**, 760–766.

Rosso, K.M., Yanina, S.V., Gorski, C.A., Larese-Casanova, P., Scherer, M.M., (2010). Connecting observations of hematite (α-Fe_2O_3) growth catalyzed by Fe(II). *Environ. Sci. Technol.* **44**, 61–67.

Schwertmann, U., Taylor, R.M., 1989. Iron oxides, in: Dixon, J.B., Weed, S.B. (Eds.), *Minerals in soil environments*, 2nd ed. Soil Science Society of America, Madison, WI, pp. 379-438.

Singh, B., Gilkes, R.J., (1992). Properties and distribution of iron oxides and their association with minor elements in the soils of south-western Australia. *J. Soil Sci.* **43**, 77-98.

Singh, B., Sherman, D.M., Gilkes, R.J., Wells, M., Mosselmans, J.F.W., (2000). Structural chemistry of Fe, Mn, and Ni in synthetic hematites as determined by extended X-ray absorption fine structure spectroscopy. *Clay. Clay Miner.* **48**, 521-527.

Singh, B., Sherman, D.M., Gilkes, R.J., Wells, M.A., Mosselmans, J.F.W., (2002). Incorporation of Cr, Mn and Ni into goethite (α-FeOOH): mechanism from extended X-ray absorption fine structure spectroscopy. *Clay Miner.* **37**, 639-649.

Strathmann, T.J., Stone, A.T., (2003). Mineral surface catalysis of reactions between Fe^{II} and oxime carbamate pesticides. *Geochim. Cosmochim. Acta* **67**, 2775–2791.

Stumm, W., 1992. *Chemistry of the solid-water interface: processes at the mineral-water and particle-water interface in natural systems*. John Wiley & Sons, Inc., New York.

Templeton, A.S., Knowles, E.J., Eldridge, D.L., Arey, B.W., Dohnalkova, A.C., M.Webb, S., Bailey, B.E., Tebo, B.M., Staudigel, H., (2009). A seafloor microbial biome hosted within incipient ferromanganese crusts. *Nat. Geosci.* **2**, 872-876.

Torrent, J., Schwertmann, U., Barron, V., (1987). The reductive dissolution of synthetic goethite and hematite by dithionite. *Clay. Miner.* **22**, 329–337.

Trolard, F., Bourrie, G., Jeanroy, E., Herbillon, A.J., Martin, H., (1995). Trace metals in natural iron oxides from laterites: A study using selective kinetic extraction. *Geochim. Cosmochim. Acta* **59**, 1285-1297.

van der Zee, C., Roberts, D.R., Rancourt, D.G., Slomp, C.P., (2003). Nanogoethite is the dominant reactive oxyhydroxide phase in lake and marine sediments. *Geology* **31**, 993–996.

Weber, K.A., Achenbach, L.A., Coates, J.D., (2006). Microorganisms pumping iron: Anaerobic microbial iron oxidation and reduction. *Nat. Rev. Microbiol.* **4**, 752-764.

Williams, A.G.B., Scherer, M.M., (2004). Spectroscopic evidence for Fe(II)-Fe(III) electron transfer at the iron oxide-water interface. *Environ. Sci. Technol.* **38**, 4782–4790.

Wu, L., Beard, B.L., Roden, E.E., Kennedy, C.B., Johnson, C.M., (2010). Stable Fe isotope fractionations produced by aqueous Fe(II)-hematite surface interactions. *Geochim. Cosmochim. Acta* **74**, 4249–4265.

Wu, L., Beard, B.L., Roden, E.E., Johnson, C.M., (2011). Stable iron isotope fractionation between aqueous Fe(II) and hydrous ferric oxide. *Environ. Sci. Technol.* **45**, 1847–1852.

Wu, L., Percak-Dennett, E.M., Beard, B.L., Roden, E.E., Johnson, C.M., (2012). Stable iron isotope fractionation between aqueous Fe(II) and model Archean ocean Fe–Si coprecipitates and implications for iron isotope variations in the ancient rock record. *Geochim. Cosmochim. Acta* **84**, 14–28.

Yanina, S.V., Rosso, K.M., (2008). Linked reactivity at mineral-water interfaces through bulk crystal conduction. *Science* **320**, 218–222.

Zachara, J.M., Fredrickson, J.K., Smith, S.C., Gassman, P.L., (2001). Solubilization of Fe(III) oxide-bound trace metals by a dissimilatory Fe(III) reducing bacterium. *Geochim. Cosmochim. Acta* **65**, 75-93.

Zachara, J.M., Kukkadapu, R.K., Fredrickson, J.K., Gorby, Y.A., Smith, S.C., (2002). Biomineralization of poorly crystalline Fe(III) oxides by dissimilatory metal reducing bacteria (DMRB). *Geomicrobiol. J.* **19**, 179–207.

CHAPTER 2

TRACE ELEMENT CYCLING THROUGH IRON OXIDE MINERALS DURING REDOX-DRIVEN DYNAMIC RECRYSTALLIZATION

This chapter has been published by the Geological Society of America:
Frierdich, A. J.; Luo, Y.; Catalano, J. G. Trace element cycling through iron oxide minerals during redox-driven dynamic recrystallization. *Geology* **2011**, *39*, 1083–1086.

ABSTRACT

Microbially-driven iron redox cycling in soil and sedimentary systems, including during diagenesis and fluid migration, may activate secondary abiotic reactions between aqueous Fe(II) and solid Fe(III) oxides. These reactions catalyze dynamic recrystallization of iron oxide minerals through localized and simultaneous oxidative adsorption of Fe(II) and reductive dissolution of Fe(III). Redox-active trace elements experience speciation changes during this process but the impact redox-driven recrystallization has on redox-inactive trace elements associated with iron oxides is uncertain. Here we demonstrate that Ni is cycled through the minerals goethite and hematite during redox-driven recrystallization. X-ray absorption spectroscopy demonstrates that during this process adsorbed Ni becomes progressively incorporated into the minerals. Kinetic studies using batch reactors containing aqueous Fe(II) and Ni pre-incorporated into iron oxides display substantial release of Ni to solution. We conclude that iron oxide recrystallization activated by aqueous Fe(II) induces cycling of Ni through the mineral structure, with adsorbed Ni overgrown in regions of Fe(II) oxidative adsorption and incorporated Ni released in regions of reductive dissolution of structural Fe(III). The redistribution of Ni among the mineral bulk, mineral surface, and aqueous solution appears to be thermodynamically-controlled and catalyzed by Fe(II). Our work suggests that important proxies for ocean composition on the early Earth may be invalid, identifies new processes controlling micronutrient availability in soil, sedimentary, and aquatic ecosystems, and points towards a mechanism for trace element mobilization during diagenesis and enrichment in geologic fluids.

INTRODUCTION

Detrital and authigenic iron oxides commonly occur in soil, sedimentary, and aqueous systems as primary grains, overgrowths, cements, ooids, concretions, and major ore bodies (Cornell and Schwertmann, 2003). Microbially-mediated iron redox cycling may occur during sediment burial, diagenesis, hydrocarbon fluid migration, and changes in soil hydrologic state (Van Cappellen and Wang, 1996; Beitler et al., 2003; Thompson et al., 2006; Weber et al., 2006), resulting in secondary abiotic reactions between aqueous Fe(II) and solid Fe(III) oxides. Such reactions are known to induce the phase transition of ferrihydrite to goethite, fractionate iron isotopes, and modify crystalline iron oxide surface structures (Viollier et al., 2000; Icopini et al., 2004; Crosby et al., 2005; Hansel et al., 2005; Catalano et al., 2010; Rosso et al., 2010). These processes are largely driven by electron transfer and atom exchange between Fe(II) in solution and iron oxide surfaces (Williams and Scherer, 2004; Pedersen et al., 2005; Handler et al., 2009; Rosso et al., 2010). The mechanism responsible involves oxidative adsorption of Fe(II) coupled to the reductive dissolution of Fe(III) at a spatially-separated surface site, with an electron conducting across the surface or through the bulk structure (Yanina and Rosso, 2008). The resulting dynamic mineral recrystallization is largely independent of macroscopic Fe(II) adsorption (Catalano et al., 2010), indicating that Fe(II) plays a catalytic role and is not consumed during the process. This facilitates continued iron oxide recrystallization even after the fluid composition suggests that equilibrium has been reached.

Iron cycling occurring in such systems promotes the redox transformations of trace elements and contaminants. These include the reduction of U(VI), Cr(VI), and halogenated hydrocarbons and the oxidation of As(III) (Buerge and Hug, 1999; Liger et

al., 1999; Elsner et al., 2004; Amstaetter et al., 2010). However, the recently identified dynamic recrystallization of iron oxides catalyzed by aqueous Fe(II) (Williams and Scherer, 2004; Pedersen et al., 2005; Yanina and Rosso, 2008; Handler et al., 2009; Catalano et al., 2010; Rosso et al., 2010) suggests that these processes may alter the fate and bioavailability of redox-inactive elements, especially those that may adsorb on (Brown et al., 1999) or incorporate in (Cornell and Schwertmann, 2003) iron oxides. Since the redox-driven dynamic recrystallization of iron oxides involves simultaneous spatially-separated growth and dissolution, we hypothesize that adsorbed species are overgrown and incorporated during growth and preexisting incorporated species are released during dissolution, thus cycling elements through the iron oxide structure.

Here we evaluate this potential trace element cycling through the iron oxide minerals goethite and hematite by separately investigating the incorporation and release of Ni(II). First, pure synthetic goethite and hematite were reacted with a Ni solution in the presence and absence of aqueous Fe(II), with the solid-phase Ni distribution between adsorbed and incorporated states determined by X-ray absorption fine-structure (XAFS) spectroscopy. Second, the temporal release of Ni from synthetic goethite and hematite containing pre-incorporated structural Ni (~2 mol%) was monitored in batch reactors in the presence or absence of aqueous Fe(II). These distinct experimental approaches were employed as each is optimized for investigating the process of interest. While wet chemical measurements and mass balance constraints can clearly demonstrate release of structural Ni to solution, XAFS measurements are required to distinguish between Ni adsorption and incorporation. However, such measurements are only feasible in systems

lacking a substantial pre-existing structural Ni content, which produces a large background Ni signal.

METHODS

General Experimental Methods

All experiments were conducted under anoxic conditions in an anaerobic chamber (Coy Laboratory Products, Inc.) containing a 3% H_2/97% N_2 atmosphere with a Pd catalyst to eliminate residual O_2. Doubly deionized water (18.2 MΩ cm) was sparged with ultra-high purity N_2 gas prior to being brought into the anaerobic chamber. Trace oxygen levels in the chamber atmosphere were further lowered by a secondary oxygen trap; the chamber atmosphere was bubbled in sequence through a 15% pyrogallol/ 50% KOH solution and deionized water. The KOH solution also served to remove trace amounts of CO_2 from the chamber. The filtered gas stream was used to re-sparge and further deoxygenate the deionized water and any solution not prepared in the chamber. Dissolved oxygen content of the deionized water was estimated colorimetrically (CHEMetrics test kit K-7511) and all analyses were below the detection limit of 1 μg/L. Fe(II) stock solutions were prepared from deoxygenated deionized water and reagent-grade $FeCl_2$•$4H_2O$. Fe(II) solutions were filtered (0.2 μm, MCE) then stored in amber plastic bottles (to prevent photooxidation) prior to use.

Fe(II)-catalyzed Ni Incorporation into Goethite and Hematite

Pure goethite and hematite were prepared according to standard methods (Schwertmann and Cornell, 2000). Ni incorporation experiments were performed in 40

mL polypropylene reaction vials containing goethite and hematite suspensions (4 g/L) in a pH 7.5 solution buffered by 10^{-3} M EPPS in a 10^{-2} M NaCl electrolyte. Twelve suspensions were spiked with Ni(II) (as $NiCl_2$) and differing initial aqueous Fe(II) concentrations (as $FeCl_2$) (Table 2-1). After pH readjustment to 7.5 (± 0.05 pH unit), the sample vials were wrapped in foil and placed on an end-over-end rotator. The pH was checked two hours later and adjusted if necessary. After reaction for either 5 or 82 days, the solid was separated from the supernatant through ultracentrifugation under anaerobic conditions. The supernatant was then removed with a syringe, filtered (0.2 μm, MCE), and immediately acidified (HNO_3, trace metal grade) inside the anaerobic chamber for Ni and Fe analysis by inductively-coupled plasma optical emission spectrometry (ICP-OES, Perkin-Elmer Optima 7300DV). The remaining supernatant was decanted and discarded while the solid was collected as a wet paste and sealed in polycarbonate sample holders using 25 μm Kapton™ tape. These were then heat sealed in polyethylene to preserve anaerobic conditions, and were analyzed within 5 days. The solid samples were then transported to the Advanced Photon Source where Ni K-edge X-ray absorption fine-structure (XAFS) spectroscopy measurements were made.

XAFS Data Collection and Analysis

Bulk XAFS measurements, including both extended X-ray absorption fine-structure (EXAFS) and X-ray absorption near-edge structure (XANES) measurements, were performed at The Advanced Photon Source at Argonne National Laboratory on beamline 20-BM (PCN-CAT) using a Si(111) double-crystal monochromator. Ni K-edge data were collected in fluorescent yield mode using a 12-element energy dispersive

Ge array detector. The harmonic content of the X-ray beam was reduced by detuning the second crystal of the monochromator by 10% and by insertion of a Rh-coated harmonic rejection mirror 1 m before the sample set to a cutoff energy of approximately 16 keV. The incident X-ray beam was also focused both vertically and horizontally to an approximately 700 by 700 μm size using a toroidal mirror coated with Pt and a 10 nm Al_2O_3 overcoat; the focusing mirror is located 2 m past the monochromator.

The X-ray beam energy was calibrated by setting the maximum in the first derivative of the XANES spectra of a Ni metal foil to 8333 eV for the Ni K-edge. XAFS spectral scans were averaged using the Athena (Ravel and Newville, 2005) interface to IFEFFIT (Newville, 2001) while normalization and background subtraction of averaged data was performed using SixPACK (Webb, 2005). The k^3-weighted EXAFS spectra of Ni were quantitatively analyzed in SixPACK using phase and amplitude functions generated from the structures of goethite [α-FeOOH] (Gualtieri and Venturelli, 1999) and hematite [α-Fe_2O_3] (Blake et al., 1966) using FEFF 7.02 (Ankudinov et al., 1998). Coordination number (N), interatomic distance (R), and σ^2 (a Debye–Waller-type factor based on a Gaussian distribution of interatomic distances), were refined using a nonlinear least-squares fitting routine. The amplitude reduction factor, S_0^2, was fixed to 0.9 for spectral fitting.

Preparation of Ni-substituted Goethite and Hematite

Ni(II)-substituted goethite and hematite samples used for kinetic release experiments were prepared using modified previously reported methods (Schwertmann and Cornell, 2000). Ni-goethite was synthesized by slowly adding 125 mL of a solution

containing 0.98 M ferric nitrate and 0.02 M nickel(II) chloride to 225 mL of 5 M NaOH. The slurry was then diluted to 1 L and placed in an oven at 70 °C for 5 days. Ni-hematite was prepared by slowly adding 600 mL of a solution containing 0.196 M ferric nitrate and 0.004 M nickel(II) chloride to 360 mL of 1 M NaOH. The pH of this slurry was then adjusted to 8.5 by dropwise addition of 1.0 or 0.1 M NaOH. The suspension was then placed in an oven set to 98 °C for 11 days. Once removed from the oven and cooled to room temperature, both materials were treated with 0.25 M HCl for 2 hr using a solid to solution ratio of 1:100. This acid treatment was employed to remove residual adsorbed cations and amorphous Ni-containing iron oxides. The materials were then washed with DI water by centrifugation until a pH >5 was achieved. The solids were resuspended into 250 mL of DI water and stored as a suspension until further use.

An aliquot was removed and oven dried at 70 °C to obtain powder that was used for sample characterization. Mineral surface area was determined by collecting nitrogen B.E.T. adsorption isotherms at 77 K using a Quantachrome instruments Autosorb-1 and found to be 39.0 and 13.0 $m^2\ g^{-1}$ for Ni-goethite and Ni-hematite, respectively. X-ray diffraction (Rigaku Geigerflex D-MAX/A diffractometer using Cu-Kα radiation) confirmed that the Ni-substituted Fe oxides consisted of goethite or hematite and contained no other crystalline impurities. Bulk Ni content was measured by ICP-OES after digestion of the solid in a 20% HNO_3:5% HCl (trace metal grade, Fisher Scientific) mixture and found to be 1.4 and 1.9 mol% for Ni-goethite and Ni-hematite, respectively.

Fe(II)-catalyzed Ni Release from Goethite and Hematite

The release of Ni was monitored by aging synthetic Ni-substituted goethite and hematite samples in the dark in 0 or 10^{-3} M Fe(II) solutions at pH 7 [10^{-3} M 4-Morpholinepropanesulfonic acid (MOPS)] in a 10^{-2} M NaCl electrolyte under anoxic, CO_2-free conditions. The suspensions were filtered (0.2 μm) at times between 0 and 15 days (each time point represents a single reactor) and the liquid aliquot was acidified for analysis by ICP-OES.

RESULTS

XANES spectra of Ni reacted with hematite and goethite in the presence of aqueous Fe(II) show progressive changes as a function of aging time and Fe(II) concentration (Figure 2-1). Spectral comparison of the samples reacted with 10^{-3} M Fe(II) for 82 days with the spectra of end-member conditions, Ni adsorbed on and incorporated in iron oxides, show clear isosbestic points (Figure 2-2), indicating two-component mixing. Principal component analysis of each series of spectra supports the presence of two primary components (Appendix). Target transformation analyses demonstrate that Ni-adsorbed and Ni-substituted iron oxides are excellent matches for the actual components contributing to these spectra. Least-squares linear-combination fitting of the hematite and goethite spectra using these end-member states demonstrates that up to 39.0±0.8% and 46.1±0.8% of the solid-associated Ni (i.e., incorporated + adsorbed) is incorporated into hematite and goethite, respectively, in the presence of aqueous Fe(II) (Figure 2-2B). Incorporation increases with Fe(II) concentration and reaction time, with little incorporation seen in the absence of Fe(II) even after 82 days (Table 2-2). The

corresponding series of EXAFS spectra agrees with this assessment (Figure 2-3, Table 2-2).

Reaction of aqueous Fe(II) with goethite and hematite containing preexisting incorporated Ni shows substantially elevated Ni release to solution compared to Fe(II)-free control experiments (Figure 2-4). Ni concentration increases according to a 2nd order rate law and model fit parameters (Table 2-3) yield calculated first half lives of 2.7 and 1.1 days for goethite and hematite, respectively. Kinetic model fits suggest that ca. 9% of the incorporated Ni in goethite, and 2% in hematite, is released into solution at equilibrium (Table 2-3). Fe(II) adsorption is rapid ($t_{1/2}$ ~ minutes; Figure 2-4) and aqueous Fe(II) concentrations remain approximately constant for most of the reaction. Ni release thus occurs on a timescale that is substantially longer than for Fe(II) adsorption but is similar to what has been observed for Fe isotope equilibration between aqueous Fe(II) and goethite (Pedersen et al., 2005; Handler et al., 2009). This suggests that release is not due to displacement of surface-associated Ni by Fe(II) but instead associated with redox-driven recrystallization of iron oxide minerals.

We propose that dynamic recrystallization of iron oxide minerals catalyzed by aqueous Fe(II) facilitates Ni cycling through the mineral structure (Figure 2-5), and that this process reflects a thermodynamically-controlled repartitioning of Ni between the mineral solid, mineral surface, and aqueous solution. This process involves localized, simultaneous growth and dissolution of iron oxide surfaces at spatially separate sites (Williams and Scherer, 2004; Pedersen et al., 2005; Yanina and Rosso, 2008; Handler et al., 2009; Catalano et al., 2010; Rosso et al., 2010). Surface-adsorbed Ni near regions experiencing oxidative growth becomes progressively overgrown and incorporated into

structural sites while existing Ni substituting in iron oxides is released into solution from regions experiencing reductive dissolution. This mechanism implies that the rates of Ni incorporation and release are partially controlled by the rate of recrystallization. The distinct directionality of Ni repartitioning observed in each component of the present work coupled with the slowing and incomplete release of Ni with increasing reaction time suggests that an equilibrium relationship between Ni in the aqueous solution and mineral phase controls this partitioning. Fe(II) thus appears to catalyze equilibration by promoting dynamic recrystallization of the iron oxides that is otherwise kinetically slow. The quantitative differences in Ni incorporation and release between hematite and goethite may reflect the relative thermodynamic stability of Ni substituted into the structure of each phase and differences in the portion of the mineral actively involved in recrystallization. The latter is supported by isotopic studies that demonstrate complete atom exchange between goethite and aqueous Fe(II) (Handler et al., 2009; Beard et al., 2010), while only a small fraction of the Fe atoms in hematite participate in exchange under similar conditions (Wu et al., 2010).

IMPLICATIONS

This previously unrecognized element cycling mechanism has implications for trace element availability and fate on the early and modern Earth. Stable Fe isotope records from banded iron formations (BIFs) indicate that Fe(II)-Fe(III) redox cycling occurred as early as the Archean (Johnson et al., 2008; Severmann et al., 2008). Iron oxides formed during BIF deposition in the Fe(II)-dominated Archean and Paleoproterozoic oceans (Anbar and Knoll, 2002) would have undergone Fe(II)-activated

surface restructuring and recrystallization during settling. The trace element cycling described in the present work would redistribute any sorbed trace elements from the surface to the interior of the particle, thereby reducing desorptive loss before lithification and enhancing trace element concentrations in the BIF. This suggests that trace element concentrations (e.g., Ni) in BIFs may not reflect micronutrient availability in the ancient ocean but instead are sensitive to the ferrous iron content of seawater. The hypothesis that a nickel famine led to the decline in atmospheric methane, facilitating the rise of atmospheric oxygen (Konhauser et al., 2009), thus lacks support as BIF Ni contents are likely not proxies for seawater Ni concentrations when the dominant redox state of the ocean changes, as occurred at the end of the Paleoproterozoic. Related proxies based on BIF composition, such as for oceanic phosphate concentrations (Bjerrum and Canfield, 2002; Konhauser et al., 2007), likewise need revisiting as large changes in seawater ferrous iron content should alter the partitioning and preservation of indicator elements.

In modern ecosystems trace elements are typically bound in solid forms such as in iron oxides that occur from oxidative weathering; these minerals commonly contain high concentrations (mol%) of incorporated trace metals (Singh and Gilkes, 1992). Fe reducing bacteria (FeRB) reductively dissolve nanocrystalline Fe(III) oxides (e.g., ferrihydrite) but more crystalline phases (e.g., goethite and hematite), which comprise the dominant pool of Fe(III) in most sediments and soils, are difficult for these organisms to metabolize; only partial reduction is observed even in nutrient-rich laboratory settings (Weber et al., 2006). However, the present work demonstrates that limited formation of biogenic Fe(II) leads to substantial release of substituting trace metals without the need for full dissolution of the iron oxide. Such excess release was previously observed during

reductive dissolution of homogeneously-substituted Co- and Ni-goethite by FeRB (Zachara et al., 2001), although the mechanism responsible was unknown at the time. Organisms with critical needs for trace elements may thus not require the ability to reduce iron or to even associate with FeRB as long as dissolved Fe(II) is present, such as from fluid migration, and micronutrient availability in modern and early Earth systems may not necessarily correlate with the activity of FeRB.

Redox-driven dynamic recrystallization of iron oxides also may provide indicators of past redox cycling and fluid migration. Trace element repartitioning between aqueous solutions and iron oxides in soils and sediments that have experienced numerous redox cycles will likely show different trace element distributions than those minerals in environments that remain consistently oxic. The distribution of trace elements in iron oxide particles may thus serve as an indicator of the extent of iron redox cycling during sediment diagenesis and in soils experiencing changing hydrologic conditions. In addition, carbonaceous substances, such as crude oil and bitumen, typically contain elevated levels of trace elements (e.g., Ni and V); these metals have been applied to oil-source rock correlation studies (Mossman, 1999). Trace element enrichment in hydrocarbon fluids may result from reduction and dissolution of iron oxides (e.g., sandstone bleaching) during fluid migration. The present work suggests that trace element release will occur predominantly during the early stages of iron oxide reductive dissolution, raising the possibility of correlating hydrocarbon metal content with initial fluid flow through a sedimentary formation. Furthermore, migration of hydrocarbons or other reducing fluids that generate only partial reduction of sedimentary iron oxides will selectively remove trace elements. The spatial variation of the trace element contents of

these minerals may thus serve as an indicator of past fluid transport that lacked the capacity or migrated too quickly to fully reduce iron oxides in the unit.

ACKNOWLEDGEMENTS

Funding was provided by the U.S. National Science Foundation through Grant EAR-0818354 and the American Chemical Society Petroleum Research Fund through Grant 48302-G2. PNC/XOR facilities at the Advanced Photon Source, and research at these facilities, are supported by the US Department of Energy - Basic Energy Sciences, a Major Resources Support grant from NSERC, the University of Washington, Simon Fraser University and the Advanced Photon Source. Use of the Advanced Photon Source is also supported by the U. S. Department of Energy, Office of Science, Office of Basic Energy Sciences, under Contract DE-AC02-06CH11357. ICP-OES analyses were performed at the Nano Research Facility at Washington University in St. Louis, which is supported by the National Science Foundation under award no. ECS-0335765. The authors wish to thank Steve Heald, Dale Brewe, Chengjun Sun, Yujie Xiong, Kate Nelson, Patty Wurm, and Alison Beehr for support with data collection.

Table 2-1. Reaction conditions for samples examined by XAFS spectroscopy and final solution concentrations of Ni and Fe after specified reaction time. All reactions were performed at pH 7.5 (10^{-3} M EPPS) in 10^{-2} M NaCl electrolyte.

Sample ID	Iron Oxide	$[Ni(II)]_0$ (M)	$[Fe(II)]_0$ (M)	Reaction Time (d)	$[Ni(II)]_{final}$ (M)	$[Fe(II)]_{final}$ (M)
goe-no-Fe-5d[a]	Goethite	2×10^{-4}	0	5	1.1×10^{-4}	-[b]
goe-low-Fe-5d	Goethite	2×10^{-4}	2×10^{-4}	5	9.2×10^{-5}	5.7×10^{-6}
goe-high-Fe-5d	Goethite	2×10^{-4}	10^{-3}	5	1.1×10^{-4}	4.9×10^{-4}
goe-no-Fe-82d	Goethite	2×10^{-4}	0	82	1.0×10^{-4}	-
goe-low-Fe-82d	Goethite	2×10^{-4}	2×10^{-4}	82	1.0×10^{-4}	8.0×10^{-6}
goe-high-Fe-82d	Goethite	2×10^{-4}	10^{-3}	82	9.3×10^{-5}	3.8×10^{-4}
hem-no-Fe-5d[a]	Hematite	2×10^{-4}	0	5	1.1×10^{-4}	-
hem-low-Fe-5d	Hematite	2×10^{-4}	2×10^{-4}	5	1.1×10^{-4}	8.1×10^{-5}
hem-high-Fe-5d	Hematite	2×10^{-4}	10^{-3}	5	1.3×10^{-4}	7.5×10^{-4}
hem-no-Fe-82d	Hematite	2×10^{-4}	0	82	1.1×10^{-4}	-
hem-low-Fe-82d	Hematite	2×10^{-4}	2×10^{-4}	82	1.1×10^{-4}	1.2×10^{-4}
hem-high-Fe-82d	Hematite	2×10^{-4}	10^{-3}	82	1.4×10^{-4}	7.9×10^{-4}

[a] Samples serve as surface-adsorbed Ni standards for linear combination fitting.
[b] Dash (-) indicates analyte was below detection limit.

Table 2-2. Linear combination fitting results of Ni K-edge XANES and EXAFS spectra using Ni-adsorbed and Ni-incorporated end-member spectral states for goethite and hematite.

Initial [Fe(II)] (M)	Reaction Time (d)	XANES	EXAFS
		% Incorporated	% Incorporated
Goethite			
2×10^{-4}	5	3(1)[a]	18(6)
10^{-3}	5	17(1)	20(9)
0	82	14.8(7)	22(6)
2×10^{-4}	82	19.7(8)	28(8)
10^{-3}	82	46.1(8)	49(8)
Hematite			
2×10^{-4}	5	0.0(5)	5(5)
10^{-3}	5	5.2(6)	7(6)
0	82	0.3(6)	4(5)
2×10^{-4}	82	20.2(7)	18(5)
10^{-3}	82	39.0(8)	22(5)

[a] Statistical uncertainties in the last digit are reported in parentheses at the 95% confidence level.

Table 2-3. Properties of Ni-substituted iron oxides and fitting parameters for Ni release and Fe(II) adsorption.

Parameter	Ni-goethite	Ni-hematite
Property		
Ni content (mol% of metal sites)	1.4	1.9
BET surface area (m^2 g^{-1})	39.0	13.0
Ni Release		
$[Ni]_{eq}$ (μM): 1 mM Fe(II)	13.8(8)[a]	4.9(5)
$[Ni]_{eq}$ (μM): 0 mM Fe(II)	0.32(4)	0.7(1)
Ni released from solid at equilibrium (% total): 1 mM Fe(II)	8.6(5)	2.0(3)
2^{nd} order rate constant (μmol L^{-1} d^{-1}): 1 mM Fe(II)	0.027(6)	0.2(1)
2^{nd} order rate constant (μmol L^{-1} d^{-1}): 0 mM Fe(II)	34(34)	12(11)
Fe(II) Adsorption		
$[Fe]_0$ (mM)	0.93(2)	0.94(2)
$[Fe]_{eq}$ (mM)	0.84(1)	0.87(1)
$[Fe]_{ads}$ (mM)	0.09(2)	0.07(2)
1^{st} order rate constant (d^{-1})	37(20)	17(12)

[a] Statistical uncertainties in the last digit are reported in parentheses at the 95% confidence level.

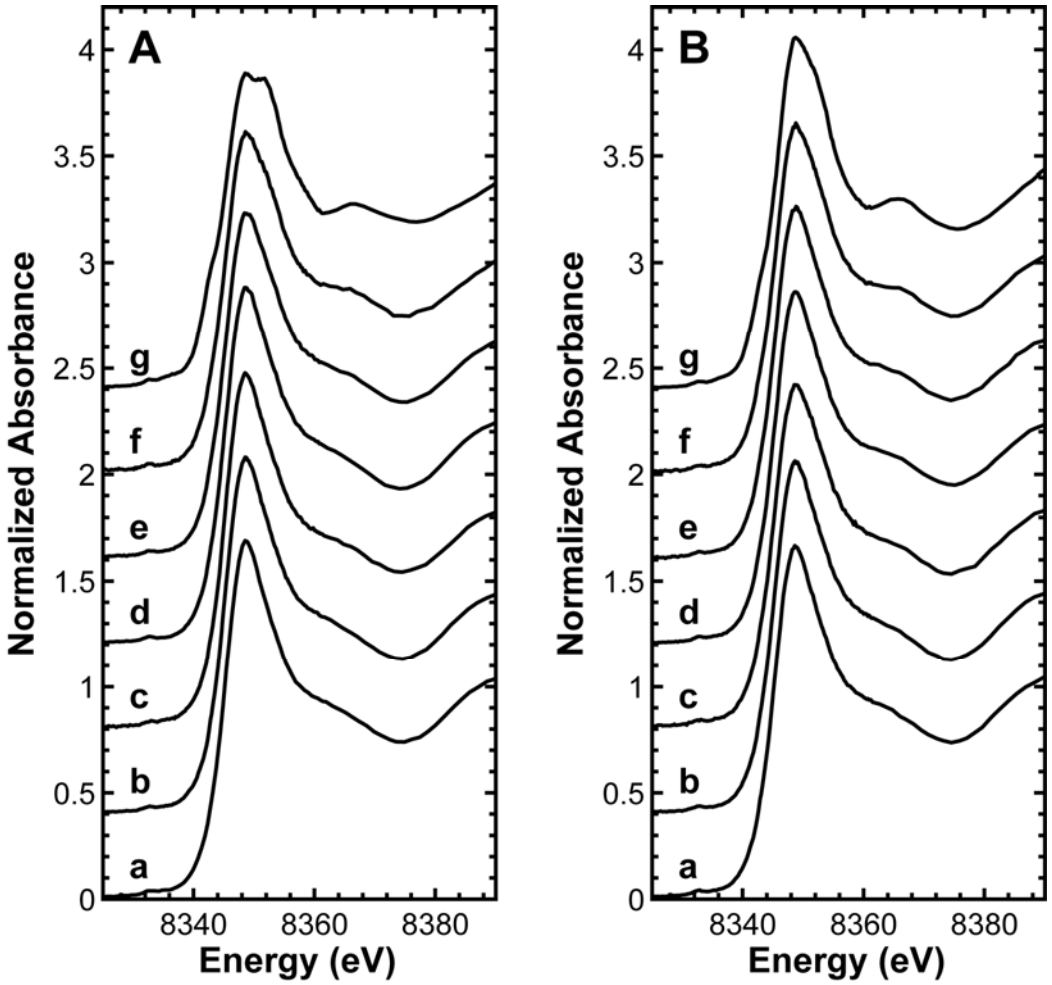

Figure 2-1. XANES spectra of Ni associated with (A) hematite and (B) goethite. Each series consists of the mineral reacted with 2×10^{-4} M Ni and varying amounts of Fe(II) at different reaction times (Table 2-1): (a) noFe-5d, (b) lowFe-5d, (c) highFe-5d, (d) noFe-82d, (e) lowFe-82d, (f) highFe-82d. Ni-substituted hematite and goethite standards are also shown (g).

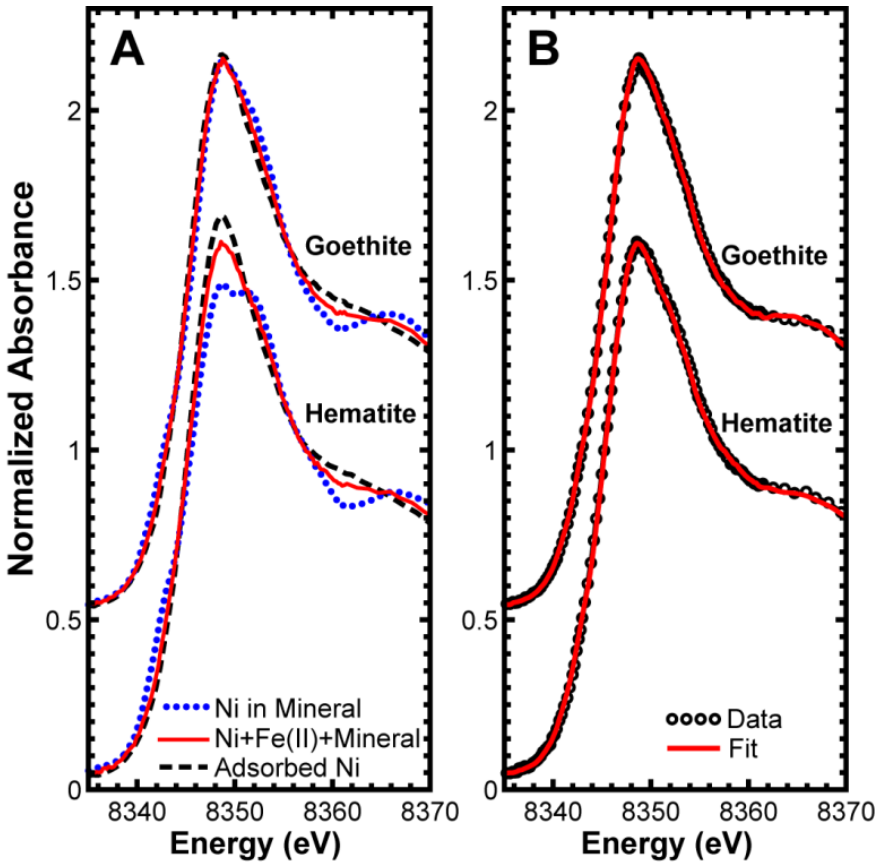

Figure 2-2. Ni K-edge X-ray absorption near-edge structure spectra of iron oxides exposed to 2×10^{-4} M Ni(II) and 10^{-3} M aqueous Fe(II) for 82 days. (A) Comparison to spectra of standard Ni-speciation end-members (i.e., Ni adsorbed on and incorporated in iron oxide). (B) Linear-combination fitting using model end-member spectra.

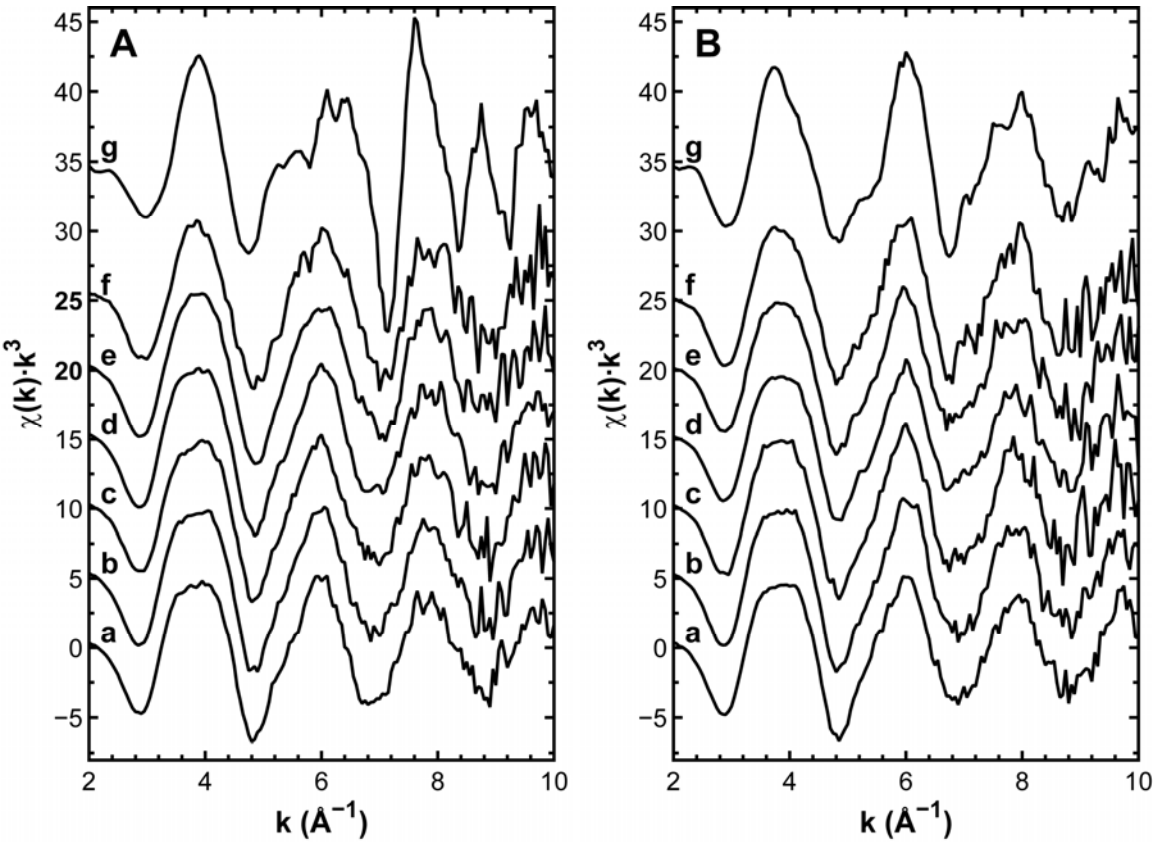

Figure 2-3. EXAFS spectra of Ni associated with (A) hematite and (B) goethite. Each series consists of the mineral reacted with 2×10^{-4} M Ni and varying amounts of Fe(II) at different reaction times (Table 2-1): (a) noFe-5d, (b) lowFe-5d, (c) highFe-5d, (d) noFe-82d, (e) lowFe-82d, (f) highFe-82d. Ni-substituted hematite and goethite standards also shown (g).

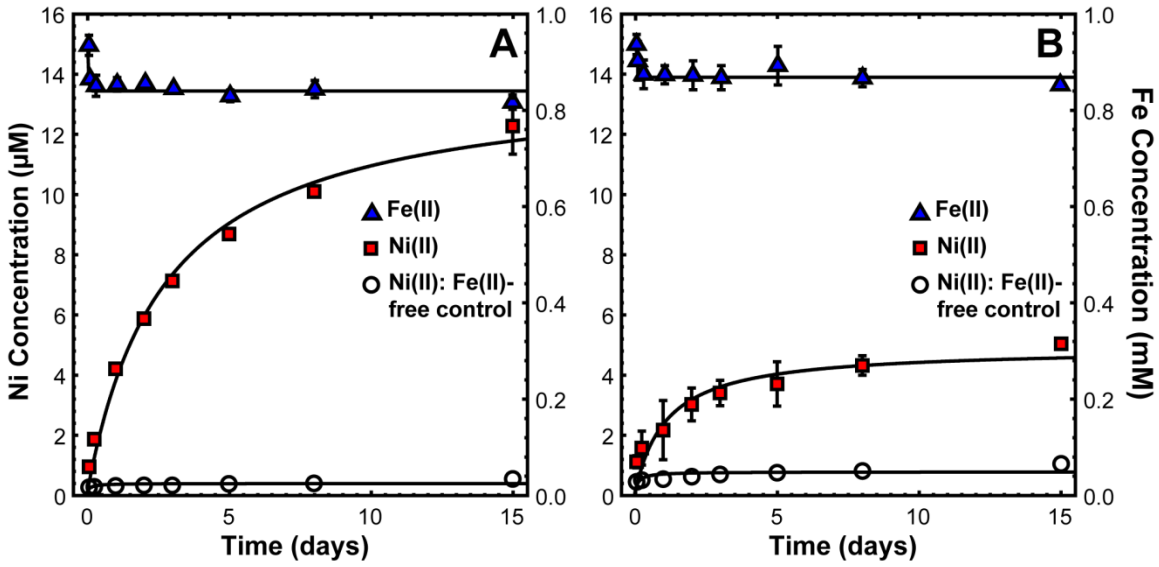

Figure 2-4. Fe(II)-catalyzed Ni release from Ni(II)-substituted iron oxides. Evolution of aqueous Fe and Ni concentrations during reaction of (A) Ni-substituted goethite and (B) Ni-substituted hematite with 10^{-3} M Fe(II). Ni release in Fe(II)-free control experiments also shown; no soluble Fe is observed in the absence of added Fe(II). Lines show 2nd order model fit for Ni release and 1st order model fit for Fe adsorption. All reactions contain 1 g/L of solid. Data points generated by reaction with Fe(II) represent mean values calculated from triplicate samples. Error bars represent standard deviation of the mean and are smaller than the symbol if not shown. Ni data points produced in absence of Fe(II) were run as single experiments.

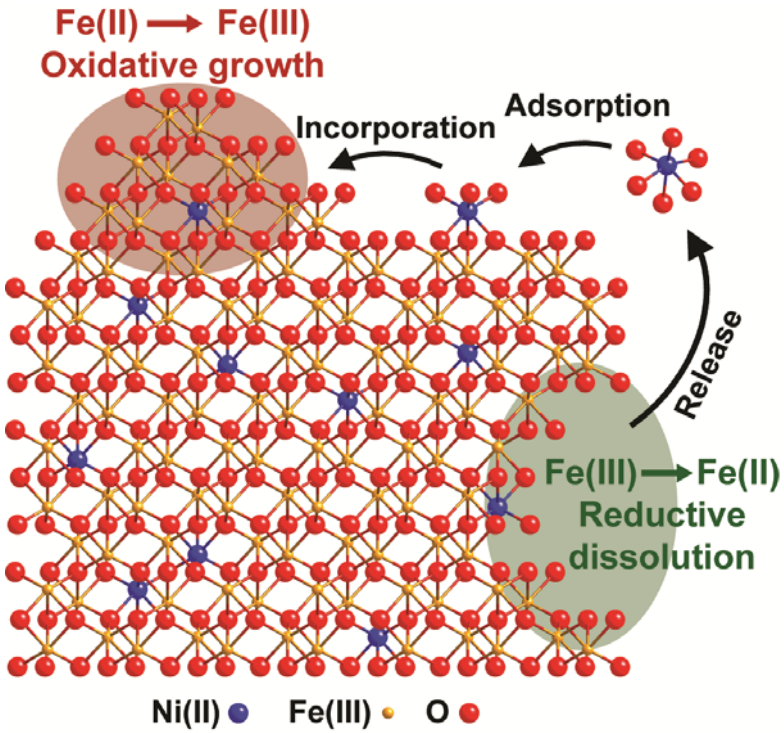

Figure 2-5. Mechanistic illustration of Fe(II)-induced recrystallization of Ni-substituted hematite. Aqueous Fe(II) catalyzes the simultaneous growth and dissolution on a single crystal. Areas of oxidative Fe(II) adsorption lead to localized surface growth and cause incorporation of adsorbed Ni. Regions exhibiting Fe(III) reductive dissolution cause the release of Ni. Fe(II) is not shown but assumed to be present in excess on the solid and in solution. View is along [100].

CHAPTER 2 APPENDIX

SECTION A1: XAFS RESULTS

EXAFS Analysis of Potential End-Member Samples

Local structural models were refined to the EXAFS spectra of the Ni-substituted goethite and hematite samples as well as the samples containing Ni sorbed to each mineral for 5 days in the absence of aqueous Fe(II). The Ni-substituted samples are well fit (Figure A2-1) with a local structural model consisting of Ni occupying an Fe site in each mineral structure (Table A2-1). The Ni-sorbed samples likewise are well fit (Figure A2-1) by structural models consistent with Ni in an adsorbed state (Table A2-2). Each spectrum was modeled as having Fe neighbors at two distinct distances that suggests the presence of corner sharing surface complexes (Arai, 2008).

Principle Component Analysis

Principle component analysis of the XANES spectra (Figure 2-1) yield IND values (Malinowski, 1977) suggestive of one primary component for the goethite series and two primary components for the hematite series (Table A2-3). For goethite, the spectral reconstruction was poor when using only one component, with major features not reproduced, but was substantially improved using two components. Given the spectral reconstruction results and the clear signature of two-component mixing in the XANES spectra for the high-Fe-82d samples (Figure 2-2), two components were selected for use in target transformation analysis. This analysis was employed to statistically justify the choice of end-member spectra for use in quantitative analysis. Target

transformation yielded SPOIL (Malinowski, 1978) values (Table A2-4) that indicate Ni-substituted and Ni-adsorbed goethite or hematite were excellent candidates for real spectra components for each respective mineral series. Principle component and target transformation analyses of the EXAFS spectra (Figure 2-3) yielded similar results (Tables A2-3 and A2-4), although the numerical parameters obtained differed because of the higher noise level in EXAFS spectra.

Quantitative Analysis of Ni Speciation

Quantitative analysis of the Ni speciation was performed using linear combination fitting, with the spectra end-members identified through target transformation analysis serving as standards. Fits to the XANES spectra demonstrate that increased Fe(II) concentrations lead to increased Ni incorporation in the mineral structure at both reaction times (Table 2-2). Furthermore, there is a substantial increase in incorporation at the longer reaction time. Incorporation into hematite after extensive aging in the absence of aqueous Fe(II) is negligible but minor incorporation into goethite is observed. Similar analyses of the corresponding EXAFS spectra agree with the relative incorporation trends. These analyses yield larger uncertainties because of the elevated noise level common in EXAFS spectra derived from fluorescence-yield measurements. The EXAFS analysis suggesting greater incorporation into goethite is likely an artifact caused by systematic errors in the data and the small spectral variation in the data series. In contrast, the lower level of incorporation of Ni into hematite obtained in the EXAFS analysis may indicate the presence of fewer Fe neighbors than occurs for Ni in the bulk hematite structure. Incorporation into a surface layer on hematite would generate a

similar electronic structure as Ni in the bulk structure but with fewer of the more distant Fe neighbors, producing the observed effects in the XANES and EXAFS spectra. This would be consistent with past observation of only minor isotopic exchange between aqueous Fe(II) and hematite (Pedersen et al., 2005; Wu et al., 2010) and the formation of a second hematite component with slightly different magnetic properties after reaction with Fe(II) (Larese-Casanova and Scherer, 2007; Rosso et al., 2010).

Table A2-1. EXAFS spectra structural fitting results for Ni-substituted iron oxides.

	EXAFS						Structure[a]
Sample	**Shell**	***N*[b]**	***R* (Å)**	**σ^2 (Å^2)**	**ΔE_0 (eV)**	**χ_ν^2**	***R* (Å)**
Ni-Hematite	O	3	1.99(2)[c]	0.002(3)	-3(2)	12.8	1.946
	O	3	2.11(2)	0.002(3)	-3(2)		2.116
	Fe[d]	4	2.92(2)	0.009(1)	-3(2)		2.953
	Fe	3	3.40(2)	0.006(2)	-3(2)		3.364
	Fe	6	3.68(2)	0.010(3)	-3(2)		3.705
Ni-Goethite							
	O	3	2.00(2)	0.001(3)	-2(3)	6.5	1.937
	O	3	2.11(2)	0.001(3)	-2(3)		2.088
	Fe	2	2.99(3)	0.005(3)	-2(3)		3.013
	Fe	2	3.18(3)	0.004(3)	-2(3)		3.292
	Fe	4	3.53(7)	0.017(4)	-2(3)		3.431

[a] Interatomic distances derived from the crystal structures of the iron oxides.
[b] Fixed to crystallographic values
[c] Statistical uncertainties in the last digit are reported in parentheses at the 95% confidence level. Parameters with no listed uncertainties were not varied during the analysis.
[d] Represents multiple unresolvable neighbors.

Table A2-2. EXAFS spectra structural fitting results for Ni-sorbed iron oxides after 5 days of reaction.

Sample	Shell	*N*	*R* (Å)	σ^2 (Å^2)	ΔE_0 (eV)	χ_ν^2
Hematite	O	6	2.06(1)[a]	0.0066(8)	-2(2)	3.3
	Fe	1.4(5)	3.42(5)	0.008	-2(2)	
	Fe	1.7(6)	3.61(5)	0.008	-2(2)	
Goethite						
	O	6	2.05(1)	0.0061(8)	-4(2)	3.9
	Fe	0.4(4)	3.4(1)	0.01	-4(2)	
	Fe	1.4(6)	3.98(6)	0.01	-4(2)	

[a] Statistical uncertainties in the last digit are reported in parentheses at the 95% confidence level. Parameters with no listed uncertainties were not varied during the analysis.

Table A2-3. Principle component analysis results.

	XANES		EXAFS	
Component	**Variance**	**IND**	**Variance**	**IND**
Hematite				
1	0.981	0.01941	0.637	0.86224
2	0.011	0.01650	0.134	1.24685
3	0.004	0.02038	0.087	2.59311
4	0.001	0.06494	0.078	9.09722
5	0.001	-	0.062	-
Goethite				
1	0.984	0.01405	0.697	0.62127
2	0.007	0.01794	0.089	1.03801
3	0.004	0.02760	0.088	2.02963
4	0.002	0.06214	0.065	7.69192
5	0.001	-	0.059	-

Table A2-4. Target transformation results using two principle components.

Standard	SPOIL (XANES)	SPOIL (EXAFS)
Hematite Dataset		
Ni-Hematite	1.25	3.67
Ni Adsorbed on Hematite	1.06	1.84
Ni-Goethite	2.81	4.99
Goethite Dataset		
Ni-Goethite	0.29	2.91
Ni Adsorbed on Goethite	0.41	1.80
Ni-Hematite	1.92	9.42

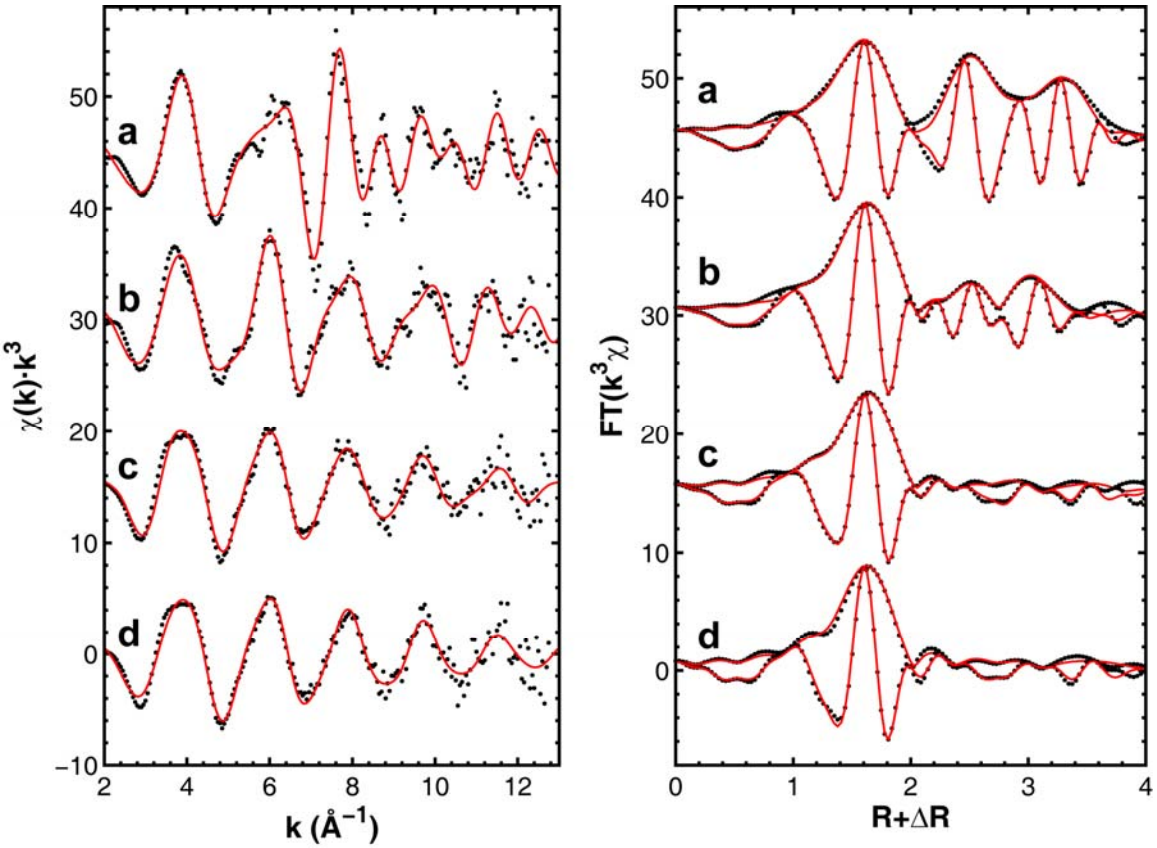

Figure A2-1. EXAFS spectra (points) and local structural model fits (lines) for (a) Ni-substituted hematite, (b) Ni-substituted goethite, and Ni adsorbed on (c) hematite or (d) goethite with 5 days reaction time.

REFERENCES

Amstaetter K., Borch T., Larese-Casanova P., and Kappler A. (2010) Redox transformation of arsenic by Fe(II)-activated goethite (α-FeOOH). *Environ. Sci. Technol.* **44**, 102–108.

Anbar A. D. and Knoll A. H. (2002) Proterozoic ocean chemistry and evolution: A bioinorganic bridge? *Science* **297**, 1137-1142.

Ankudinov A. L., Ravel B., Rehr J. J., and Conradson S. D. (1998) Real-space multiple-scattering calculation and interpretation of x-ray-absorption near-edge structure. *Phys. Rev. B* **58**, 7565–7576.

Arai Y. (2008) Spectroscopic evidence for Ni(II) surface speciation at the iron oxyhydroxides-water interface. *Environ. Sci. Technol.* **42**, 1151-1156.

Beard B. L., Handler R. M., Scherer M. M., Wu L., Czaja A. D., Heimann A., and Johnson C. M. (2010) Iron isotope fractionation between aqueous ferrous iron and goethite. *Earth Planet. Sc. Lett.* **295**, 241–250.

Beitler B., Chan M. A., and Parry W. T. (2003) Bleaching of Jurassic Navajo Sandstone on Colorado Plateau Laramide highs: Evidence of exhumed hydrocarbon supergiants? *Geology* **31**, 1041-1044.

Bjerrum C. J. and Canfield D. E. (2002) Ocean productivity before about 1.9 Gyr ago limited by phosphorus adsorption onto iron oxides. *Nature* **417**, 159-162.

Blake R. L., Hessevick R. E., Zoltai T., and Finger L. W. (1966) Refinement of the hematite structure. *Am. Mineral.* **51**, 123-129.

Brown G. E., Jr., Henrich V. E., Casey W. H., Clark D. L., Eggleston C., Felmy A., Goodman D. W., Gratzel M., Maciel G., McCarthy M. I., Nealson K. H., Sverjensky D. A., Toney M. J., and Zachara J. M. (1999) Metal oxide surfaces and their interaction with aqueous solutions and microbial organisms. *Chem. Rev.* **99**, 77-174.

Buerge I. J. and Hug S., J. (1999) Influence of mineral surfaces on chromium(VI) reduction by iron(II). *Environ. Sci. Technol.* **33**, 4285–4291.

Catalano J. G., Fenter P., Park C., Zhang Z., and Rosso K. M. (2010) Structure and oxidation state of hematite surfaces reacted with aqueous Fe(II) at acidic and neutral pH. *Geochim. Cosmochim. Acta* **74**, 1498–1512.

Cornell R. M. and Schwertmann U. (2003) *The iron oxides: Structure, properties, reactions, occurrences and uses*. Wiley-VCH Verlag GmbH & Co. KGaA.

Crosby H. A., Johnson C. M., Roden E. E., and Beard B. L. (2005) Coupled Fe(II)-Fe(III) electron and atom exchange as a mechanism for Fe isotope fractionation during dissimilatory iron oxide reduction. *Environ. Sci. Technol.* **39**, 6698–6704.

Elsner M., Schwarzenbach R. P., and Haderlein S. (2004) Reactivity of Fe(II)-bearing minerals toward reductive transformation of organic contaminants. *Environ. Sci. Technol.* **38**, 799–807.

Gualtieri A. and Venturelli P. (1999) In situ study of the goethite-hematite phase transformation by real time, synchrotron powder diffraction. *Am. Mineral.* **84**, 895–904.

Handler R. M., Beard B. L., Johnson C. M., and Scherer M. M. (2009) Atom exchange between aqueous Fe(II) and goethite: An Fe isotope tracer study. *Environ. Sci. Technol.* **43**, 1102–1107.

Hansel C. M., Benner S. G., and Fendorf S. (2005) Competing Fe(II)-induced mineralization pathways of ferrihydrite. *Environ. Sci. Technol.* **39**, 7147–7153.

Icopini G. A., Anbar A. D., Ruebush S. S., Tien M., and Brantley S. L. (2004) Iron isotope fractionation during microbial reduction of iron: The importance of adsorption. *Geology* **32**, 205-208.

Johnson C. M., Beard B. L., and Roden E. E. (2008) The iron isotope fingerprints of redox and biogeochemical cycling in modern and ancient earth. *Annu. Rev. Earth Planet. Sci.* **36**, 457–493.

Konhauser K. O., Lalonde S., Amskold L., and Holland H. D. (2007) Was there really an Archean phosphate crisis? *Science* **315**, 1234.

Konhauser K. O., Pecoits E., Lalonde S. V., Papineau D., Nisbet E. G., Barley M. E., Arndt N. T., Zahnle K., and Kamber B. S. (2009) Oceanic nickel depletion and a methanogen famine before the Great Oxidation Event. *Nature* **458**, 750–753.

Larese-Casanova P. and Scherer M. M. (2007) Morin transition suppression in polycrystalline ^{57}hematite (α-Fe_2O_3) exposed to ^{56}Fe(II). *Hyperfine Interact.* **174**(1-3), 111–119.

Liger E., Charlet L., and Cappellen P. V. (1999) Surface catalysis of uranium(VI) reduction by iron(II). *Geochim. Cosmochim. Acta* **63**, 2939–2955.

Malinowski E. R. (1977) Determination of number of factors and experimental error in a data matrix. *Analytical Chemistry* **49**, 612-617.

Malinowski E. R. (1978) Theory of error for target factor-analysis with applications to mass spectrometry and nuclear magnetic resonance spectrometry. *Analytica Chimica Acta* **103**, 339-354.

Mossman D. J. (1999) Carbonaceous substances in mineral deposits: Implications for geochemical exploration. *J. Geochem. Explor.* **66**, 241-247.

Newville M. (2001) IFEFFIT: interactive EXAFS analysis and FEFF fitting. *J. Synchrotron Rad.* **8**, 322-324.

Pedersen H. D., Postma D., Jakobsen R., and Larsen O. (2005) Fast transformation of iron oxyhydroxides by the catalytic action of aqueous Fe(II). *Geochim. Cosmochim. Acta* **69**, 3967–3977.

Ravel B. and Newville M. (2005) ATHENA, ARTEMIS, HEPHAESTUS: data analysis for X-ray absorption spectroscopy using IFEFFIT. *J. Synchrotron Rad.* **12**, 537--541.

Rosso K. M., Yanina S. V., Gorski C. A., Larese-Casanova P., and Scherer M. M. (2010) Connecting observations of hematite (α-Fe_2O_3) growth catalyzed by Fe(II). *Environ. Sci. Technol.* **44**, 61–67.

Schwertmann U. and Cornell R. M. (2000) *Iron oxides in the laboratory: Preparation and characterization*. Wiley-VCH.

Severmann S., Lyons T. W., Anbar A., McManus J., and Gordon G. (2008) Modern iron isotope perspective on the benthic iron shuttle and the redox evolution of ancient oceans. *Geology* **36**, 487-490.

Singh B. and Gilkes R. J. (1992) Properties and distribution of iron oxides and their association with minor elements in the soils of south-western Australia. *J. Soil Sci.* **43**, 77-98.

Thompson A., Chadwick O. A., Rancourt D. G., and Chorover J. (2006) Iron-oxide crystallinity increases during soil redox oscillations. *Geochim. Cosmochim. Acta* **70**, 1710–1727.

Van Cappellen P. and Wang Y. F. (1996) Cycling of iron and manganese in surface sediments: A general theory for the coupled transport and reaction of carbon, oxygen, nitrogen, sulfur, iron, and manganese. *American Journal of Science* **296**, 197-243.

Viollier E., Inglett P. W., K. Hunter A. N. R., and Cappellen P. V. (2000) The ferrozine method revisited: Fe(II)/Fe(III) determination in natural waters. *Appl. Geochem.* **15**, 785-790.

Webb S. M. (2005) SIXPack: a Graphical User Interface for XAS Analysis Using IFEFFIT. *Physica Scipta* **T115**, 1011-1014.

Weber K. A., Achenbach L. A., and Coates J. D. (2006) Microorganisms pumping iron: Anaerobic microbial iron oxidation and reduction. *Nat Rev Microbiol* **4**, 752-764.

Williams A. G. B. and Scherer M. M. (2004) Spectroscopic evidence for Fe(II)-Fe(III) electron transfer at the iron oxide-water interface. *Environ. Sci. Technol.* **38**, 4782–4790.

Wu L., Beard B. L., Roden E. E., Kennedy C. B., and Johnson C. M. (2010) Stable Fe isotope fractionations produced by aqueous Fe(II)-hematite surface interactions. *Geochim. Cosmochim. Acta* **74**, 4249–4265.

Yanina S. V. and Rosso K. M. (2008) Linked reactivity at mineral-water interfaces through bulk crystal conduction. *Science* **320**, 218–222.

Zachara J. M., Fredrickson J. K., Smith S. C., and Gassman P. L. (2001) Solubilization of Fe(III) oxide-bound trace metals by a dissimilatory Fe(III) reducing bacterium. *Geochim. Cosmochim. Acta* **65**, 75-93.

CHAPTER 3

CONTROLS ON IRON(II)-ACTIVATED TRACE ELEMENT RELEASE FROM GOETHITE AND HEMATITE

This chapter has been published by the American Chemical Society:
Frierdich, A. J.; Catalano, J. G. Controls on Fe(II)-activated trace element release from goethite and hematite. *Environ. Sci. Technol.* **2012**, *46*, 1519−1526.

ABSTRACT

Electron transfer and atom exchange (ETAE) between aqueous Fe(II) and Fe(III) oxides induces surface growth and dissolution that affects trace element fate and transport. We have recently demonstrated Ni(II) cycling through goethite and hematite (adsorbed Ni incorporates into the mineral structure and pre-incorporated Ni releases to solution) during Fe(II)-Fe(III) ETAE. However, the chemical parameters affecting net trace element release remain unknown. Here, we examine the chemical controls on Ni(II) and Zn(II) release from Ni- and Zn-substituted goethite and hematite during reaction with Fe(II). Release follows a rate law consistent with surface reaction limited mineral dissolution and suggests release occurs near sites of Fe(III) reductive dissolution during Fe(II)-Fe(III) ETAE. Metal substituent type affects reactivity; Zn release is more pronounced from hematite than goethite whereas the opposite trend occurs for Ni. Buildup of Ni or Zn in solution inhibits further release but this resumes upon fluid exchange, suggesting that sustained release is possible under flow conditions. Mineral and aqueous Fe(II) concentrations as well as pH strongly affect sorbed Fe(II) concentrations, which directly control the reaction rates and final metal concentrations. Our results demonstrate that structurally-incorporated trace elements are mobilized from iron oxides into fluids without abiotic or microbial net iron reduction. Such release may affect micronutrient availability, contaminant transport, and the distribution of redox-inactive trace elements in natural and engineered systems.

INTRODUCTION

Biogeochemical iron cycling initiates secondary abiotic reactions between aqueous Fe(II) and Fe(III) oxide minerals. Such reactions are largely driven by electron transfer and atom exchange (ETAE) between aqueous Fe(II) and the Fe(III) oxide surface via a mechanism involving simultaneous Fe(II) oxidative adsorption coupled to Fe(III) reductive dissolution (Williams and Scherer, 2004; Larese-Casanova and Scherer, 2007; Yanina and Rosso, 2008; Handler et al., 2009; Catalano et al., 2010; Rosso et al., 2010). Fe(III)-bearing clays have been shown to undergo similar ETAE with aqueous Fe(II) (Schaefer et al., 2011) and existing data suggests a comparable process occurs between aqueous Mn(II) and Mn(III,IV) oxides (Bargar et al., 2005; Zhu et al., 2010), with such reactions influencing contaminant reduction (Hofstetter et al., 2003) and trace element contents (Frierdich et al., 2011a). Fe(III) oxide minerals are abundant in soils, sediments, and groundwater systems (Cornell and Schwertmann, 2003), and often control the fate and transport of trace elements (Brown et al., 1999). A robust understanding of their reactivity with Fe(II) and how associated trace elements are affected during ETAE is required to predict the effect of biogeochemical processes on contaminant fate and micronutrient availability.

Reaction of Fe(II) with Fe(III) oxides initiates redox transformations of associated trace elements and contaminants, including the reduction of halogenated hydrocarbons, nitroaromatic compounds, chromate, selenate, pertechnetate, and uranyl (Haderlein and Pecher, 1998; Buerge and Hug, 1999; Liger et al., 1999; Elsner et al., 2004; Boland et al., 2011) and the oxidation of arsenite (Amstaetter et al., 2010). Fe(II)-induced trace element incorporation into iron oxides has been suggested from experiments involving redox-

inactive divalent metal [Me(II)] adsorption onto goethite in the presence of Fe(II) (Coughlin and Stone, 1995), but similar studies using hematite did not observe any Me(II) incorporation (Jeon et al., 2003). These conflicting results may reflect differences in the extent of Fe(II)-activated recrystallization of goethite and hematite (Pedersen et al., 2005; Handler et al., 2009; Beard et al., 2010; Wu et al., 2010). However, in both studies Me(II) fractions were determined using acid extractions and such conditions can cause partial surface dissolution, thereby releasing incorporated metals in the uppermost surface layers. Consequently, the impact of Fe(II)-Fe(III) ETAE on the fate of redox-inactive elements is unclear.

We have already demonstrated that reaction of goethite and hematite with aqueous Fe(II) causes both adsorbed Ni to progressively incorporate into the mineral structures and Ni pre-incorporated into goethite and hematite to release into solution (Chapter 2). This previously unrecognized trace element cycle may substantially affect contaminant fate and micronutrient availability during biogeochemical iron cycling. The chemical controls (e.g., Fe(II) concentration, pH, product inhibition) on redox-inactive metal release from Fe oxide minerals during Fe(II)-Fe(III) ETAE are, however, currently unknown. Here we examine the parameters controlling the release of Ni(II) and Zn(II) during reaction of aqueous Fe(II) with Ni(II)- and Zn(II)-substituted goethite and hematite. We present kinetic data for Ni and Zn release in closed- and open-systems, examine the effect of mineral surface site concentration, Fe(II) concentration, and pH on release, and develop an extended kinetic model to predict trace element release under variable Fe(II) and mineral surface site concentrations.

MATERIALS AND METHODS

Metal-substituted Fe Oxide Preparation

Ni- and Zn-substituted goethite and hematite (here on termed NiGoe, ZnGoe, NiHem, and ZnHem, or collectively MeGoe and MeHem) were prepared by modified standard methods (Schwertmann and Cornell, 2000); full details are reported in Chapter 2. After preparation, all materials were treated with 0.25 M HCl for 2 h using a solid to solution ratio of 1:100 (m/m) to remove residual adsorbed cations and amorphous metal hydroxides and washed free of electrolytes by deionized (DI) water (>18.2 MΩ cm). The solids were then resuspended in 250 mL of DI water and stored as a suspension until further use. An aliquot was removed and oven dried at 70°C for sample characterization.

Mineral Characterization

Quantitative mineral compositions were determined using inductively-coupled plasma optical emission spectrometry (ICP-OES, Perkin-Elmer Optima 7300DV) after solid digestion in a 20% HNO_3:5% HCl mixture (trace metal grade, Fisher Scientific) at 70°C. Dissolution stoichiometry was determined separately by adding 10 mg of Me-substituted iron oxide to 100 mL of 4 M HCl at 70°C; samples were collected periodically then filtered, diluted, and analyzed by ICP-OES. X-ray diffraction (XRD) was performed on a Rigaku Geigerflex D-MAX/A diffractometer using Cu-Kα radiation. Crystal morphology and particle size were examined using a JEOL JSM-7001F field emission scanning electron microscope (SEM) operated at 30 keV. BET surface area was measured by N_2 adsorption using a Quantachrome Instruments Autosorb-1. Zn K-edge extended X-ray absorption fine structure (EXAFS) spectra were collected at the

Advanced Photon Source in fluorescence yield at beamline 20-BM to determine the metal substitution mechanism. Detailed experimental protocol and data analysis procedures are described elsewhere (Appendix Section A1) and corresponding Ni EXAFS data were reported previously (Chapter 2).

Kinetic Reactions

Anoxic conditions were maintained for all experiments using an anaerobic chamber (4% H_2/96% N_2 atmosphere) and Pd catalyst to eliminate residual O_2. Trace O_2 and CO_2 in the chamber were further lowered by passing the atmosphere in sequence through a 15% pyrogallol-50% KOH solution and DI water. DI water used for experiments was deoxygenated using procedures described in Chapter 2. Dissolved oxygen was measured colorimetrically and always below the detection limit of 1 μg/L (CHEMetrics test kit K-7511). Fe(II) stock solutions were prepared from reagent-grade $FeCl_2$•$4H_2O$, then filtered (0.2 μm, MCE) and stored in amber plastic bottles (to prevent photo-oxidation) prior to use.

Kinetic experiments were performed in 15 mL polypropylene reactors, with each serving as a single time point. Unless stated otherwise, all reaction conditions were 1 g/L of solid, 10^{-3} M initial Fe(II), 10^{-2} M NaCl, and 10^{-3} M 3-(N-Morpholino)propanesulfonic acid (MOPS) at pH 7. Variable solution pH values of 8, 5.5, and 4 were maintained with 10^{-3} M MOPS, 10^{-3} M 2-(N-Morpholino)ethanesulfonic acid (MES), or HCl, respectively. pH drift was minimal (± 0.1 pH unit) throughout the reaction. Fe(II), electrolyte, and buffer were added from a concentrated stock solution and diluted accordingly. A kinetic experiment was initiated by spiking the reactor solution with the target Me-substituted Fe

oxide from a concentrated aqueous stock suspension, bringing the final reactor volume to 10 mL. Reactors were then wrapped in foil and placed on an end-over-end rotator. Samples were collected at defined intervals by removing the entire suspension with a syringe and immediately filtering (0.2 μm, MCE) the aliquot to remove the iron oxide particles and stop the reaction. The filtrate was then acidified (HNO_3, trace metal grade) inside the anaerobic chamber. Metal concentrations were measured by ICP-OES; blanks, reference standards (TraceCERT®, Sigma-Aldrich), and check standards were run with each sample set. All soluble iron was assumed to be exclusively Fe(II) as Fe(III) solubility is below the ICP-OES detection limit. No dissolved Fe was detected in any sample in which no Fe(II) was added.

Additional experiments examined if Me release from MeGoe and MeHem continues following product removal by fluid exchange. Me-substituted iron oxides were reacted in triplicate in 40 mL batch reactors. The suspensions were centrifuged (under anoxic conditions) after two weeks and aqueous samples were collected, filtered, then analyzed by ICP-OES. The remaining liquid was decanted and discarded, while the solid was resuspended in a fresh 10^{-3} M Fe(II) solution buffered at pH 7. This cycle was repeated seven times. Additional control reactors with the same conditions were not centrifuged or sampled until the end of the seventh cycle.

Kinetic Data Analysis

Fe(II)-activated Ni release follows second-order kinetics and is proposed to occur during iron oxide surface dissolution (Chapter 2). Therefore, each kinetic time-series in this study was modeled by a second-order rate law for mineral dissolution (Berner, 1978;

Zhang and Nancollas, 1990), in which the rate of Me release is proportional to the square of the undersaturation Me concentration:

$$Rate = \frac{d[Me]}{dt} = k_{obs}([Me]_{eq} - [Me])^2 \quad (1)$$

where t is time (days), $[Me]$ is metal concentration (μM) at time t, $[Me]_{eq}$ is the equilibrium Me concentration (μM), and k_{obs} is a pseudo second-order rate constant ($\mu M^{-1}\ d^{-1}$). At time $t = 0$, $[Me] = 0$ and the initial rate ($\mu M\ d^{-1}$) is:

$$Rate_0 = k_{obs}[Me]_{eq}^{\ 2} \quad (2)$$

Integration of eq 1 with the boundary condition $[Me] = 0$ at $t = 0$, yields the time-dependent Me concentration:

$$[Me] = \frac{[Me]_{eq}^{\ 2} k_{obs} t}{1 + [Me]_{eq} k_{obs} t} \quad (3)$$

Reaction order of Me release was verified by the integral method (Brantley and Conrad, 2008).

RESULTS

Characteristics of Me-substituted iron oxides

Bulk Me contents in NiGoe, ZnGoe, NiHem, and ZnHem are 1.4, 2.1, 1.9, and 1.7 mol%, respectively. Congruent release of Ni and Zn during complete acid dissolution of MeHem materials suggests they are homogeneously distributed throughout the particles (Figure 3-1). In contrast, slight incongruent dissolution of Ni and Zn occurs for MeGoe, suggesting minor Me enrichment near the periphery of the crystals (Figure 3-1) (Cornell et al., 1992; Cornell and Schwertmann, 2003). XRD patterns indicate all materials are free of crystalline impurities (Figure 3-2). SEM images reveal similar crystal morphology

and particle size among iron oxide phases regardless of the substituting metal (Figure 3-3). BET specific surface areas for NiGoe, ZnGoe, NiHem, and ZnHem are 39.0, 42.6, 13.0, and 13.1 m^2/g, respectively. SEM, BET, and XRD data demonstrate that Me-substituted iron oxides of the same phase are physically similar and only differ by the type and quantity of substituting Me. EXAFS spectroscopy demonstrates that Ni substitution into goethite and hematite (Chapter 2) and Zn substitution into goethite occurs by replacement of an Fe(III)-octahedral site (Appendix Section A1). The EXAFS data for ZnHem shows that Zn is tetrahedrally coordinated in hematite, and does not exists as a separate Zn phase. However, the exact crystallographic location of Zn cannot be fully resolved although it is consistent with Zn occupying an Fe site in the structure (See Appendix, Section A1).

Fe(II)-promoted Trace Element Release

All Me-substituted iron oxides were exposed to Fe(II) and Fe(II)-free solutions under similar conditions to determine how mineral phase and substituent type affects trace element release. Each material exhibits enhanced Me release in an Fe(II) solution compared to an Fe(II)-free control (Figure 3-4A,B). Me concentrations follow a second-order kinetic rate law, suggesting that release is surface reaction limited rather than diffusion controlled (Berner, 1978) and is consistent with mineral dissolution (Zhang and Nancollas, 1990). These results are in-line with our previous proposed release mechanism: release occurs from reductive dissolution during Fe(II)-Fe(III) ETAE (Chapter 2). Zn and Ni release differ, however, and appear to depend on the mineral phase and quantity of substituting element involved in the reaction (Figure 3-4A,B), with

the less abundant trace element in a given mineral phase exhibiting greater release. Kinetic fit parameters (Table 3-1) yield calculated first half lives of 2.7 and 3.0 days for NiGoe and ZnGoe, and 1.1 and 1.7 days for NiHem and ZnHem, respectively. Kinetic fits demonstrate that approximately 9%, 2%, 2%, and 6% of the incorporated Me in NiGoe, ZnGoe, NiHem, and ZnHem, respectively, is released into solution at equilibrium (Table 3-1).

As discussed previously (Chapter 2), Me release kinetics appear unrelated to the rate of Fe(II) adsorption and appear to be controlled by recrystallization during Fe(II)-Fe(III) ETAE. Control experiments confirm that metal release is not associated with an adsorbed species or mineral contaminant (See Appendix, Section A2). No secondary phases (e.g., magnetite or Me-ferrites) are detected in the solids by XRD after prolonged exposure to Fe(II) (Figure 3-5).

Sequential Release Studies

Me concentrations appear to approach equilibrium in closed-system reactors but this could also indicate that surface passivation has occurred. If this behavior is an equilibrium control then removal of aqueous Me would perturb the system and reinitiate release. This was tested by reacting MeGoe and MeHem with Fe(II) over a 14 week period while replacing the fluid biweekly. The cumulative fraction of trace element release from Me-substituted iron oxides is substantially higher when the aqueous phase is periodically exchanged compared to closed-system reactors where products remain in the system (Figure 3-4C,D). Cumulative Me release declines with each solution-exchange cycle and follows a second-order kinetic rate law (Figure 3-4C,D), which suggests our

experimental set-up behaves like a flow-through column reactor operated at solution-solid equilibrium conditions. The declining release with each fluid exchange may be a thermodynamic effect caused by a reduction in the mol% of Ni or Zn remaining in the active portion of the mineral or from buildup of adsorbed Ni and Zn that remains in the system.

Data fit parameters (Table 3-1) predict that about 28, 16, 7, and 15% of the incorporated Me in NiGoe, ZnGoe, NiHem, and ZnHem, respectively, is released into solution with continued fluid exchange (cf. 9%, 2%, 2%, and 6% for closed-system reactions). Aqueous Fe(II) concentrations measured at the end of each cycle show little change. Fit parameters (Table 3-1) also demonstrate that each material releases Me at a different rate, as indicated by the declining release after each step. MeHem nears completion of Me release faster than MeGoe but releases less Me overall. Our sequential release studies demonstrate that product formation exhibits a negative feedback on further release and affects the final Me distribution among the mineral solid and aqueous solution. Furthermore, they suggest that sustained release is possible under flow conditions, resulting in a greater fraction of trace element removal from the mineral.

Effect of pH

Solution pH varies widely in natural and engineered systems, affects ion adsorption and metal solubility, and thus likely has a strong influence on the rate and extent of Ni and Zn release to solution. The effect of pH on release was examined by reacting NiGoe and ZnHem in Fe(II) and Fe(II)-free solutions buffered at a series of pH values. Increasing pH decreases Me release in Fe(II)-free control experiments whereas

increasing pH increases the rate and the quantity of Me release during reaction of NiGoe and ZnHem with Fe(II) (Figure 3-6). An exception exists for reactions at pH 8 as release occurs more rapidly, but the amounts released after two weeks is less than that at pH 7; this likely results from either enhanced adsorption or reduced Ni and Zn solubility at pH 8. Release in Fe(II)-free solutions at low pH likely reflects increased Fe solubility and a larger pool of mobile Fe atoms which should produce more recrystallization and thus greater metal release. The pH dependent Me release trends observed in Fe(II) solutions suggests that Fe(II) sorption is a major control on release. Sorbed Fe(II) may enhance Fe(II)-activated recrystallization or compete with released Ni and Zn for surface sites, thereby preventing re-adsorption and raising the final concentration in solution.

Effect of Surface Site and Fe(II) Concentrations on Me Release

Fe(II) activates trace element release but the concentration range in which this occurs and the mechanistic controls are unknown. The effect of Fe(II) on Me release was examined by varying the surface site and Fe(II) concentrations in order to probe a potential reaction mechanism. A series of reactors containing increasing amounts of NiGoe and ZnHem, while adding 10^{-3} M Fe(II) and holding pH constant, results in progressively increasing Me release (Figures 3-7A,B). Me release also increases with the amount of Fe(II) added to solution while surface site concentration and pH are held constant (Figure 3-7C,D). Second-order kinetics (eq 3) describe the data well for all conditions.

Both kinetic fitting parameters (i.e., $[Me]_{eq}$ and k_{obs}) vary as functions of surface site and Fe(II) concentrations. These parameters also covary, with $[Me]_{eq}$ being directly

proportional to the inverse of k_{obs} (Figure 3-7E), and thus their product is constant (i.e., $[Me]_{eq} \times k_{obs} = k$, with k (d^{-1}) representing a master rate constant). $[Me]_{eq}$ shows a relationship to surface site (Figure 3-7F) and equilibrium Fe(II) concentrations ($[Fe(II)]_{eq}$); the latter is well described by a Freundlich isotherm (Figures 3-7G). This apparent isotherm-like relationship between $[Me]_{eq}$ and $[Fe(II)]_{eq}$ suggests that $[Me]_{eq}$ is proportional to the amount of Fe(II) sorbed to the mineral ($[Fe(II)]_{sorb}$). We estimated $[Fe(II)]_{sorb}$ in each experiment by fitting a first order curve to the Fe(II) concentration data and then subtracting the $[Fe(II)]_{eq}$ from the initial Fe(II) concentration for each kinetic experiment. Direct comparison of $[Me]_{eq}$ to $[Fe(II)]_{sorb}$ shows a correlation between these parameters (Figure 3-7H) but there is substantial scatter in the data because the studies were not designed to precisely measure Fe(II) sorption. In addition, minor experimental errors can produce large systematic errors in the Fe(II) sorption data because of the small fraction of Fe(II) that sorbs under the experimental conditions.

Initial Me release rates, calculated from eq 2 using the extracted fit parameters for each condition, show a linear dependence on mineral surface area (Figure 3-8A). This further suggests that the reaction rate is not diffusion or mass transfer limited but instead is directly proportional to the concentration of surface sites. Initial Me release rates also vary with added Fe(II) but instead follow a Freundlich adsorption isotherm as $[Fe(II)]_{eq}$ increases (Figure 3-8B). This behavior is consistent with a surface-mediated reaction (Vannice, 2005), and implies that a maximum Me release rate is obtained at conditions of maximum Fe(II) sorption and that the release rate is directly proportional to $[Fe(II)]_{sorb}$. Substitution of the experimentally-determined relationship $[Me]_{eq} \times k_{obs} = k$ into eq 2 shows that the initial release rate is directly proportional to $[Me]_{eq}$. The isotherm-like

dependence of initial release rate on $[Fe(II)]_{eq}$ further supports the apparent proportionality between $[Me]_{eq}$ and $[Fe(II)]_{sorb}$.

Additional insight into the interfacial controls on metal release is gained from examining how $[Me]_{eq}$ or $[Fe(II)]_{sorb}$ normalized by mineral concentration varies with $[Fe(II)]_{eq}$ (Figure 3-9). The data points from the variable mineral concentration experiments do not all fall on the same curve, as would be expected for a simple adsorption relationship. These normalized values decrease with increasing mineral concentration and thus with an increasing concentration of surface sites. This behavior is consistent with competitive adsorption in systems where the number of surface sites is being varied; competitive adsorption also produces a surface coverage dependence on concentration that follows a Freundlich isotherm-like curve rather than a Langmuir isotherm. This thus supports $[Me]_{eq}$ being proportional to $[Fe(II)]_{sorb}$ and further indicates that the system is influenced by competitive adsorption between Me and Fe(II).

This relationship can be described by a competitive Langmuir isotherm (Vannice, 2005):

$$[Fe(II)]_{sorb} = \frac{n\, m\, K_{Fe}[Fe(II)]_{eq}}{1 + K_{Fe}[Fe(II)]_{eq} + K_{Me}[Me]_{eq}} \quad (4)$$

where n is surface site density (μmol/g), m is mineral concentration (g/L), and K_{Fe} and K_{Me} are unitless Langmuir adsorption constants for Fe(II) and Me, respectively. If $[Me]_{eq}$ is proportional to $[Fe(II)]_{sorb}$ (i.e., $[Me]_{eq} = [Fe(II)]_{sorb} \times a$, where a is a unitless constant) then:

$$[Me]_{eq} = \frac{S\, m\, K_{Fe}[Fe(II)]_{eq}}{1 + K_{Fe}[Fe(II)]_{eq} + K_{Me}[Me]_{eq}} \quad (5)$$

where $S = n \times a$ and represents the mass-normalized amount of Me released at Fe(II) surface saturation (μmol/g). As competitive effects increase with increasing $[Me]_{eq}$, high $[Me]_{eq}$ reduces $[Fe(II)]_{sorb}$; because these are proportional, competitive adsorption between Me and Fe(II) serves as a negative feedback on Me release.

Given this quantitative relationship between $[Me]_{eq}$ and $[Fe(II)]_{eq}$, an extended kinetic model to predict Ni or Zn concentration with time for any given mineral and equilibrium Fe(II) concentration was derived. K_{Fe} cannot be determined accurately from the kinetic data because of competitive adsorption, so it was determined from Fe(II) sorption data on Me-free goethite and hematite prepared using similar methods (data not shown). K_{Fe} values of 25.1 and 55.5 were determined for goethite and hematite, respectively. Since $[Me]_{eq}$ and k_{obs} covary (i.e., $[Me]_{eq} \times k_{obs} = k$) under changing Fe(II) and mineral concentrations (Figure 3-7E), eq 3 simplifies to

$$[Me] = \frac{k[Me]_{eq}t}{1 + kt} \tag{6}$$

Solving eq 5 for $[Me]_{eq}$ results in a quadratic equation with a positive root that can be substituted into eq 6 to model Me release as a function of time for the entire NiGoe or ZnHem data sets (all experiments with varying surface site and Fe(II) concentrations) using only three parameters: K_{Me}, k, and S. Me release is well predicted (R^2=0.981 for NiGoe and R^2=0.982 for ZnHem) using the extended kinetic model (Figure 3-10A,B). Furthermore, the competitive adsorption Langmuir model using the refined fitting parameters (Table 3-2) closely predicts the $[Me]_{eq}$ values obtained from fitting the individual data sets (Figure 3-10C,D). The resulting model provides a framework for predicting Me concentrations in solution based solely on Fe(II) and mineral concentrations. This may be generalized to more complex systems containing additional

metals or mineral phases if an extensive pH-dependent data set is coupled to aqueous speciation and surface complexation models.

DISCUSSION

Reaction Mechanism

We have shown that both the rate and extent of trace element release are proportional to the concentration of sorbed Fe(II). This is consistent with Fe(II)-Fe(III) ETAE, which must involve sorbed Fe(II) as an intermediate. Since trace element release observed in this study likely occurs following Fe(III) reductive dissolution, it should closely reflect the actual Fe(II)-Fe(III) ETAE process. The dependence of the extent and rate of trace element release on sorbed Fe(II) thus suggests that the amount of sorbed Fe(II) is also the primary control on ETAE and that by increasing aqueous Fe(II), a greater proportion of the mineral particles are recrystallized.

Application of the extent of trace element release as a proxy for the extent of Fe(II)-Fe(III) ETAE may provide useful insight regarding the reactivity of various Fe(III) oxide minerals. Caution must be used, however, as readsorption and reincorporation of trace elements can occur simultaneously with release (Chapter 2). Nevertheless, the extent of trace element release does indicate the minimum amount of recrystallization of the mineral particles that has occurred and relative comparisons can be made. This suggests that in the closed-system and sequential release reactions about 10% and 30%, respectively, of the particle volume of NiGoe have undergone atom-exchange. Given this approach, sequential release studies suggest that a greater proportion of goethite undergoes atom-exchange compared to hematite (Figure 3-4, Table 3-1). This is

consistent with previous studies examining atom-exchange using stable Fe isotope equilibration techniques (Pedersen et al., 2005; Handler et al., 2009; Beard et al., 2010; Wu et al., 2010), although there is substantial variability is past work regarding the absolute amount of atom-exchange, with complete (Handler et al., 2009; Beard et al., 2010) to <10% percent (Pedersen et al., 2005; Mikutta et al., 2009) exchange being reported for goethite and little (Wu et al., 2010) (<1%) to no (Pedersen et al., 2005) exchange reported for hematite. The substantial quantities of Ni and especially Zn released from hematite in our study suggests that a greater proportion of hematite may recrystallize during ETAE than has been previously observed (Pedersen et al., 2005; Wu et al., 2010). Direct comparisons between studies are difficult, however, as different approaches and experimental conditions were used. Even so, our results suggest that the incorporation of trace elements into the iron oxide structure either affects the reactivity of these minerals or Ni and Zn exhibit differing repartitioning behavior during mineral recrystallization, as differing quantities of elements are released to solution depending on mineral phase and substituent type (Figure 3-4).

These opposite release trends observed for Ni and Zn (Figure 3-4) cannot be explained by differences in Me adsorption or by the quantity or distribution of Me within the crystal structure. Metal oxide minerals consistently show greater adsorption affinity for Zn than Ni (Brown and Parks, 2001). However, the pH was buffered at the same value for all experiments and the specific surface area did not vary significantly with metal substituent for either goethite or hematite and thus differences in Me adsorption following release from the bulk structure cannot explain the Me release trends. Differences in net Me content also cannot be the origin of the Me release trends as the

materials with less incorporated Me actually release more Me to solution (Figure 3-4, Table 3-1). Similarly, Me release does not correlate with the spatial distribution of Me substitution within the iron oxide structure, as bulk dissolution experiments show homogeneous Me distribution within MeHem, and MeGoe materials exhibit similar, slightly non-stoichiometric dissolution behavior (Figure 3-1). EXAFS spectroscopy, however, clearly shows that Ni (Chapter 2) and Zn (Appendix Section A1) coordination in hematite differs, and while both Ni and Zn appear to substitute into goethite by replacement of an iron site, the exact charge balancing mechanism is unknown. Differences in the substitution and charge balancing mechanisms should alter the stability of the metal in the structure and, consequently, the repartitioning behavior during Fe(II)-activated recrystallization. This element specific repartitioning behavior in goethite and hematite or the extent of mineral recrystallization likely explains the differences in Ni and Zn release.

Implications for Trace Element Mobility

This study demonstrates that the speciation of redox-inactive trace elements is substantially affected by Fe(II)-activated recrystallization, with structurally-incorporated elements released to solution. This recrystallization may preferentially mobilize elements in ways not expected based on pH-dependent adsorption or mineral stability, an example being preferential Zn release from hematite (Figure 3-4). While there is incorporation of surface-adsorbed elements into iron oxide particles during Fe(II)-Fe(III) ETAE (Chapter 2), net incorporation may not be possible when an Fe(II)-containing fluid comes into contact with existing iron oxide minerals rich in trace elements. Ultimately, the net

directionality of trace element repartitioning will vary among environments but should be thermodynamically controlled and dependent on the relative activities of trace elements in solution, adsorbed on the surface, and incorporated within the mineral structure. Sequential release studies suggest that sustained trace element release will occur under natural flow conditions (e.g., subsurface groundwater flow and soil draining). Advective removal of released metals allows continued reaction and greater net release than occurs in closed-systems where equilibrium between the solid and fluid is quickly reached. Sediments undergoing periodic redox cycling have the potential for sustained trace element release even if these elements are nominally sequestered in iron oxide mineral structures.

ACKNOWLEDGEMENTS

This work was supported by the National Science Foundation (NSF) through Grant No. EAR-0818354. ICP-OES analyses were performed at the Nano Research Facility at Washington University in St. Louis, which is supported by the NSF under award ECS-0335765. PNC/XSD facilities and research at the Advanced Photon Source are supported by the US Department of Energy (contract DE-AC02-06CH11357), a Major Resources Support grant from NSERC, the University of Washington, Simon Fraser University, and the Advanced Photon Source.

Table 3-1. Fitting parameters for Me release from reaction of Me-substituted iron oxides (1 g/L) in the presence and absence of 1 mM Fe(II) at pH 7.

Reaction System	NiGoe	ZnGoe	NiHem	ZnHem
Closed-Fe(II)[a]				
$[Me]_{eq}$ (μM)	13.8(8)[b]	3.7(4)	4.9(5)	12(1)
k_{obs} (μM^{-1} d^{-1})	0.027(6)	0.09(4)	0.2(1)	0.05(2)
Total release (%)	8.6(5)	1.5(2)	2.0(3)	5.7(5)
Closed-No Fe(II)[a]				
$[Me]_{eq}$ (μM)	0.32(4)	-[c]	0.7(1)	-
k_{obs} (μM^{-1} d^{-1})	34(34)	-	12(11)	-
Total release (%)	0.20(3)	-	0.29(4)	-
Sequential Release				
Total release (%)	27.6(2)	16(2)	6.6(1)	14.9(7)
Constant ($\%^{-1}$ $cycle^{-1}$)	1.53(5)	0.7(2)	6.3(4)	4.3(8)
Total release (%): No fluid exchange	11.2	1.4	2.0	8.7

[a] Data for NiGoe and NiHem is from Chapter 2.
[b] Statistical uncertainties in the least significant digit(s) are reported in parentheses at the 95% confidence level.
[c] Dash (-) indicates analyte was below detection limit and thus no fitting parameters were obtained.

Table 3-2. Extended kinetic model fitting results.

	Fitting Parameters				
Mineral	K_{Fe} [a]	K_{Me}	k (d^{-1})	S ($\mu mol\ g^{-1}$)	R^2
NiGoe	25.1	41(2)[b]	0.39(3)	31(2)	0.981
ZnHem	55.5	23(2)	0.77(7)	11.7(4)	0.982

[a] Values fixed during fit.
[b] Statistical uncertainties in last digit reported in parentheses at 95% confidence level.

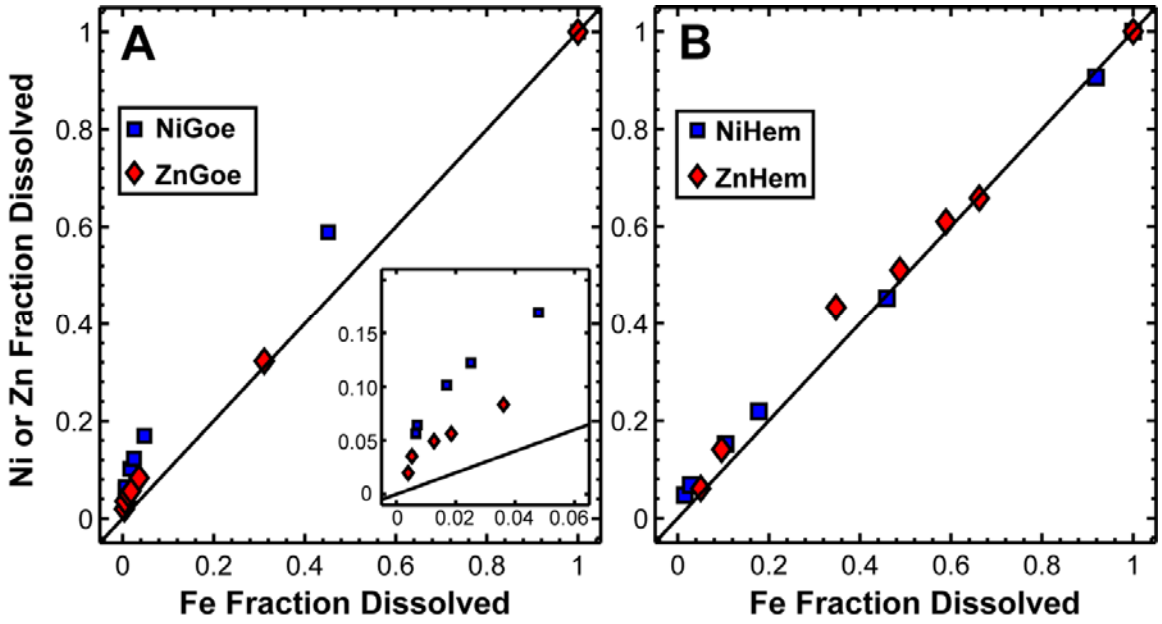

Figure 3-1. Fraction of Ni or Zn dissolved during complete acid dissolution of Ni- and Zn-substituted goethite and (B) hematite. Solid line represents 1:1 dissolution.

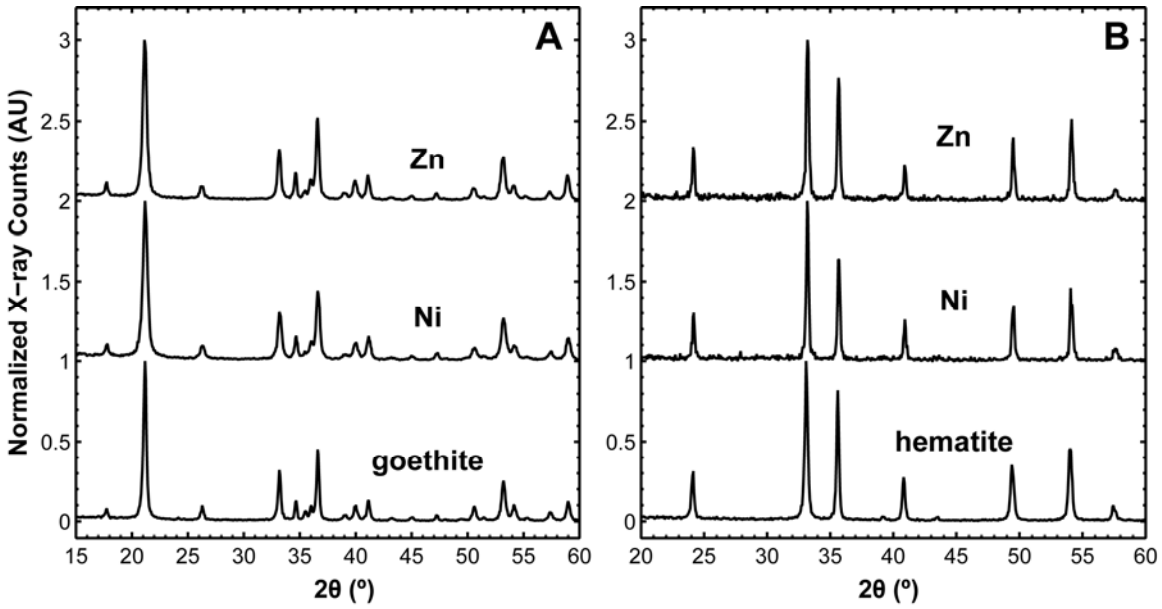

Figure 3-2. (A) XRD patterns of Me-free goethite, 1.4 mol% Ni-substituted goethite, and 2.1 mol% Zn-substituted goethite. (B) XRD patterns of Me-free hematite, 1.9 mol% Ni-substituted hematite, and 1.7 mol% Zn-substituted hematite.

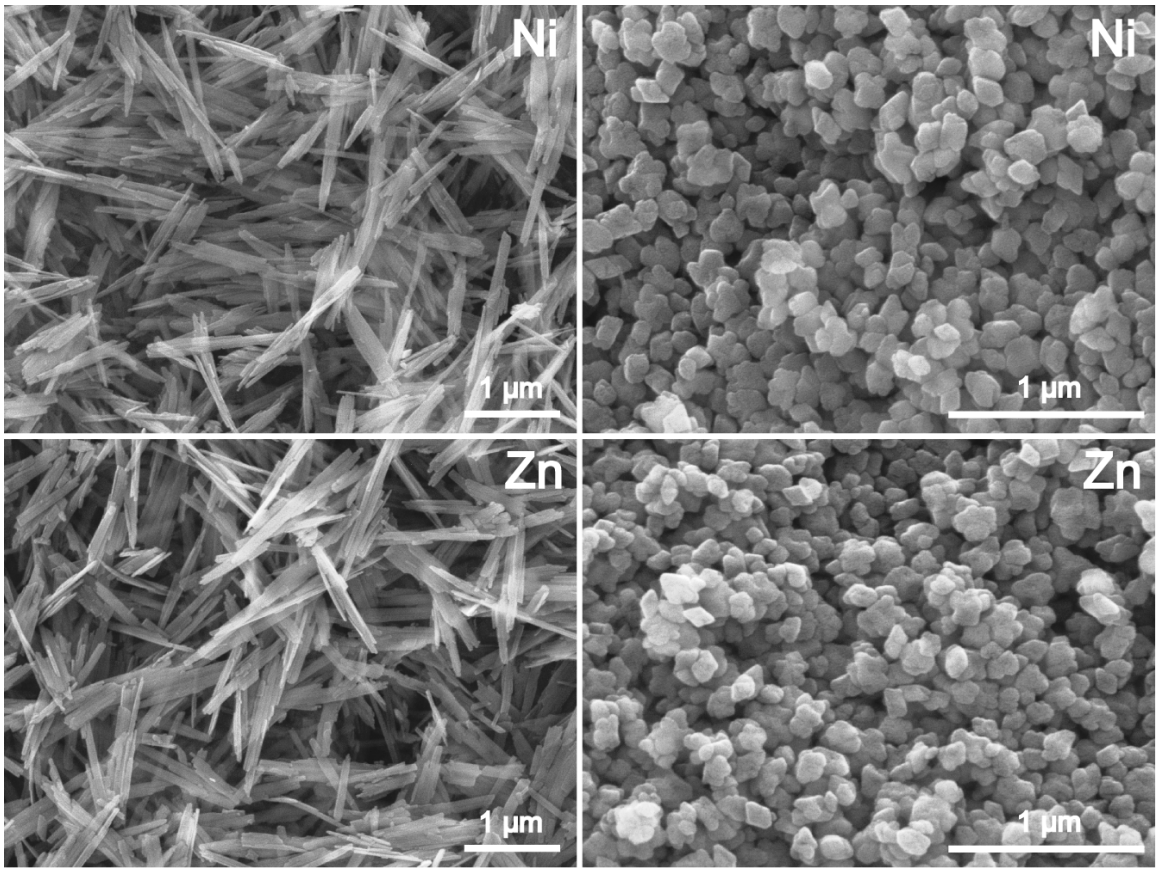

Figure 3-3. SEM images of **(left)** MeGoe and **(right)** MeHem particles. Samples were coated with gold by plasma deposition (Cressington Sputter Coater 108) to improve image quality.

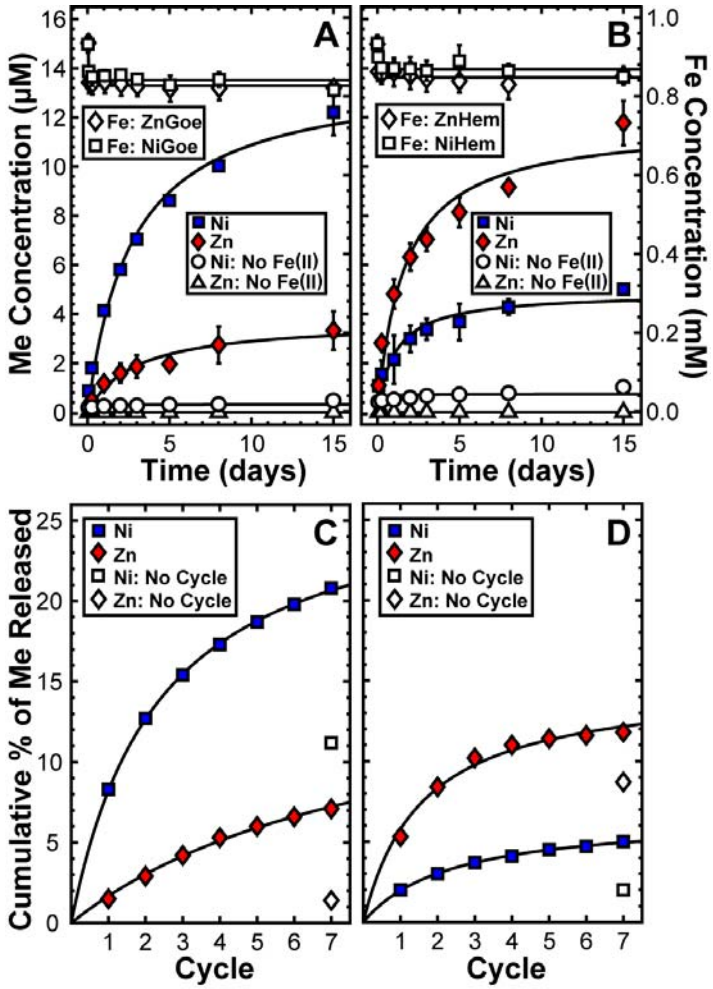

Figure 3-4. Evolution of aqueous Fe, Ni, and Zn concentrations during reaction of (A) MeGoe and (B) MeHem with 10^{-3} M Fe(II) at pH 7. Ni and Zn release in Fe(II)-free control experiments also shown; no soluble Fe is observed in the absence of added Fe(II). Lines show second-order kinetic fits for Me release and 1st order kinetic fit for Fe adsorption. Error bars represent standard deviation of the mean from triplicate samples and are smaller than the symbol if not shown. Fe(II)-free experiments were not run in triplicate. Data for Ni release previously reported (Chapter 2). Percent of Me content released from (C) MeGoe and (D) MeHem during sequential release studies whereby the aqueous phase is exchanged with a Me-free Fe(II) solution every 2 weeks (i.e., 1 cycle) while the solid remains for further reaction. Open symbols represent Ni or Zn concentrations in reactors without fluid exchange over the entire 14 week period. Solid lines show data fits.

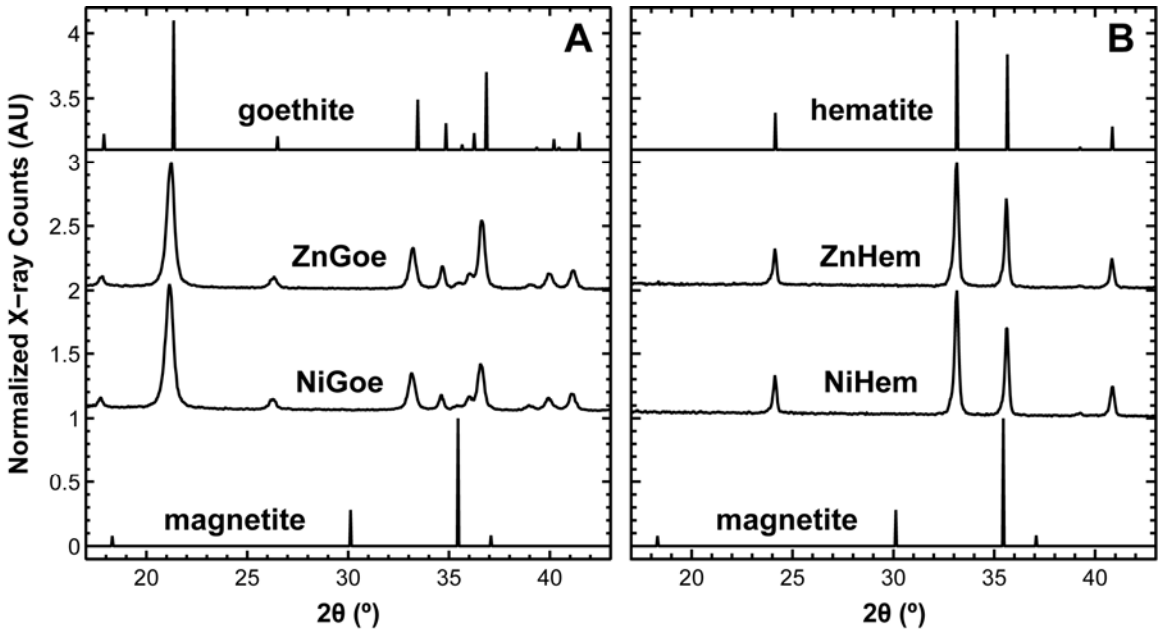

Figure 3-5. XRD patterns of **(A)** MeGoe and **(B)** MeHem after reaction with 1 mM Fe(II) for 14 weeks at pH 7. Calculated XRD line positions and relative intensities for goethite, hematite, and magnetite are also shown for comparison.

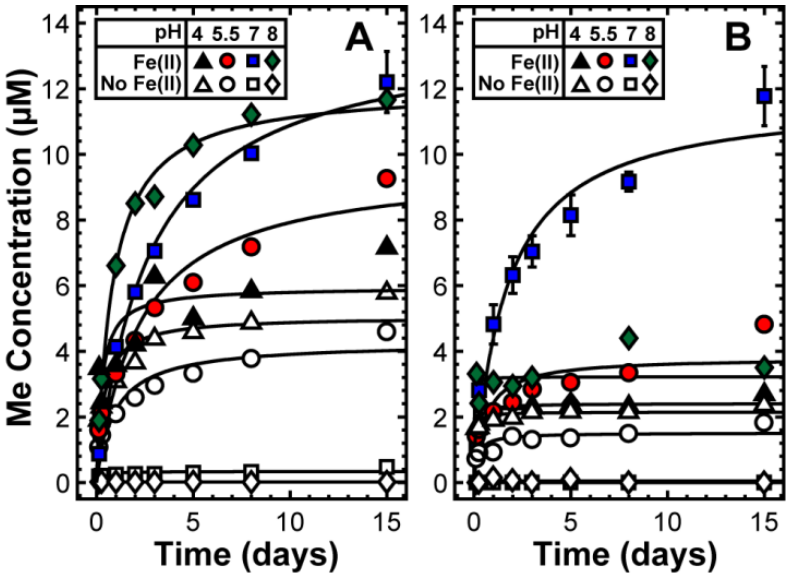

Figure 3-6. Ni and Zn release from (A) NiGoe and (B) ZnHem in buffered solutions of varying pH in the presence and absence of 10^{-3} M Fe(II). Lines show second-order kinetic fits.

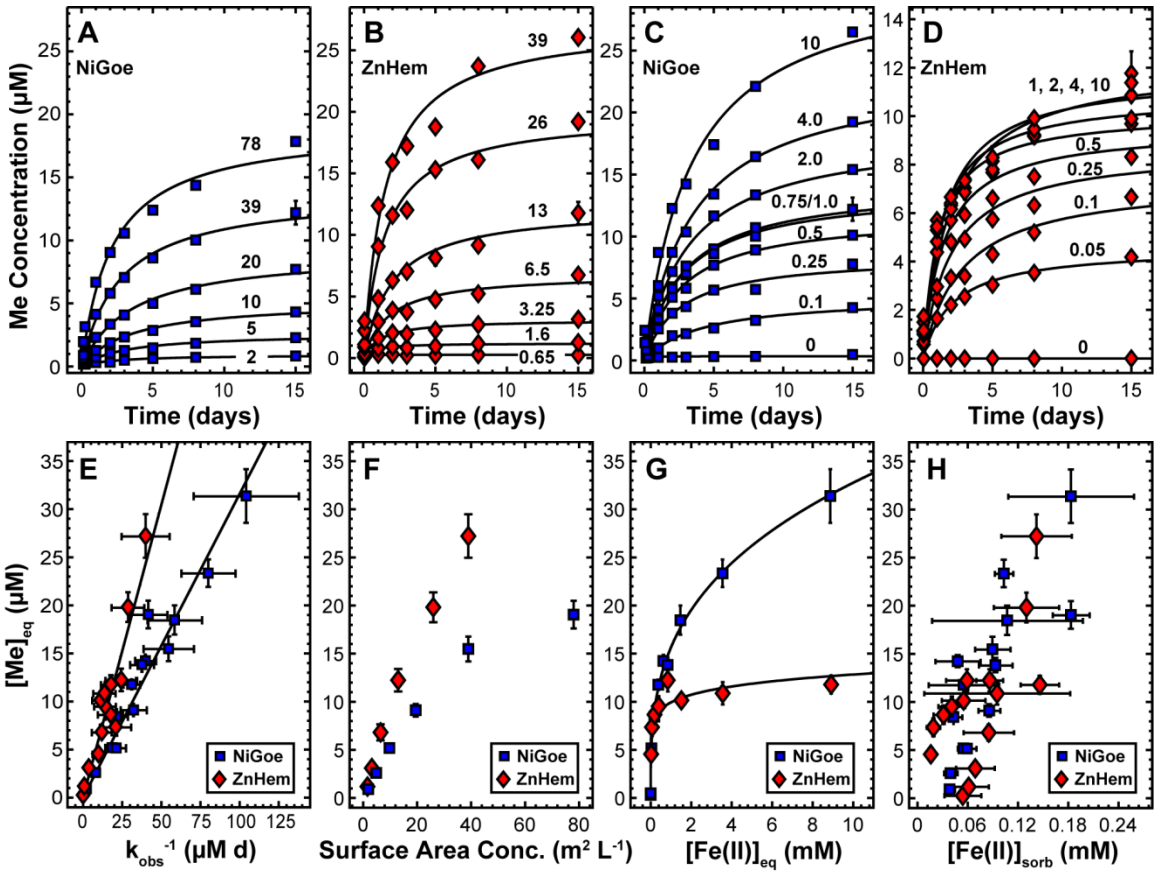

Figure 3-7. Time-dependent Ni (squares) and Zn (diamonds) release at pH 7 from NiGoe and ZnHem with (A,B) variable mineral surface area concentration (m^2 L^{-1}) and 10^{-3} M initial Fe(II), and (C,D) variable initial Fe(II) concentrations (mM) with a constant surface area concentration (39 and 13 m^2 L^{-1} for NiGoe and ZnHem, respectively). Solid lines represent second-order kinetic fits. Equilibrium Me concentrations plotted against the inverse of k_{obs} after reaction of (E) NiGoe and ZnHem at variable surface site and Fe(II) concentrations. $[Me]_{eq}$ and k_{obs} were extracted from kinetic fits in Figs. 3A-D. Dependence of Ni and Zn equilibrium concentrations on (F) surface area, (G) equilibrium Fe(II), and (H) Fe(II) sorbed concentrations. Solid lines in (E) and (G) represent linear fits and Freundlich isotherm fits, respectively.

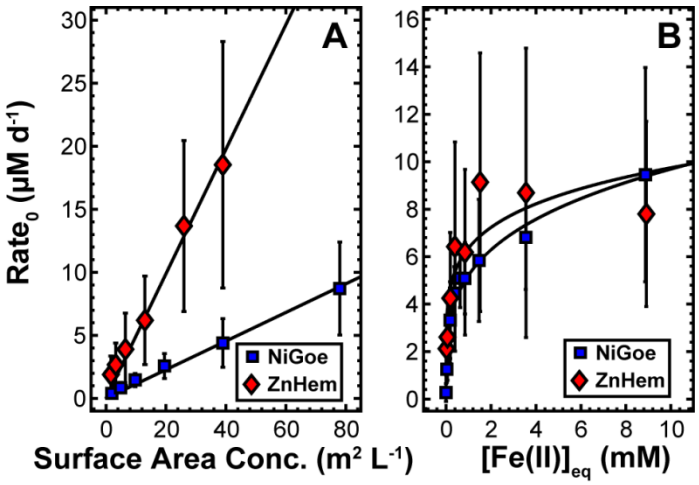

Figure 3-8. Dependence of initial Me release rate (calculated from second-order fit parameters and eq 2) on (A) mineral surface area and (B) Fe(II) equilibrium concentration. Solid lines in (A) and (B) represent linear fits and Freundlich isotherm fits, respectively.

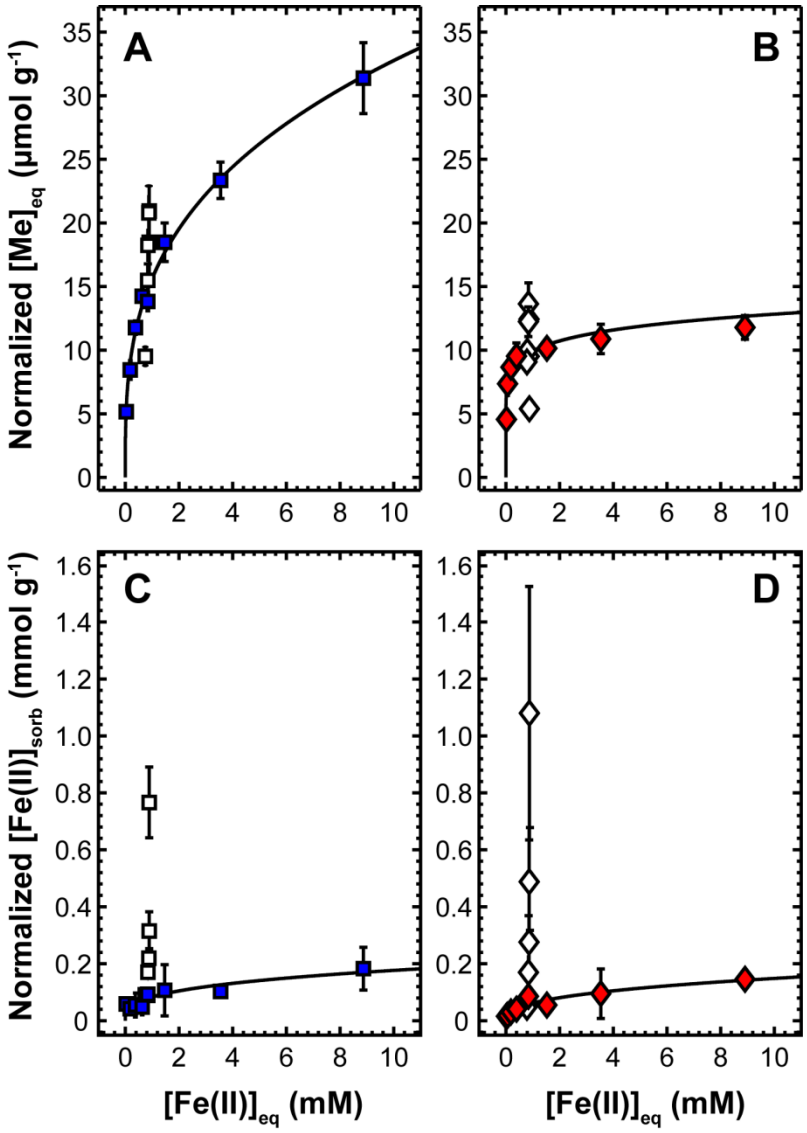

Figure 3-9. Equilibrium **(A)** Ni and **(B)** Zn concentrations (µM), and sorbed Fe(II) concentrations (mM) on **(C)** NiGoe and **(D)** ZnHem, normalized by the mineral concentration (g/L) in each experiment as a function of equilibrium Fe(II) concentration. Filled symbols are from experiments in which initial Fe(II) concentration was varied while pH and surface site concentration were constant. Open symbols are from experiments in which initial Fe(II) concentration and pH was constant but the surface site concentration was varied.

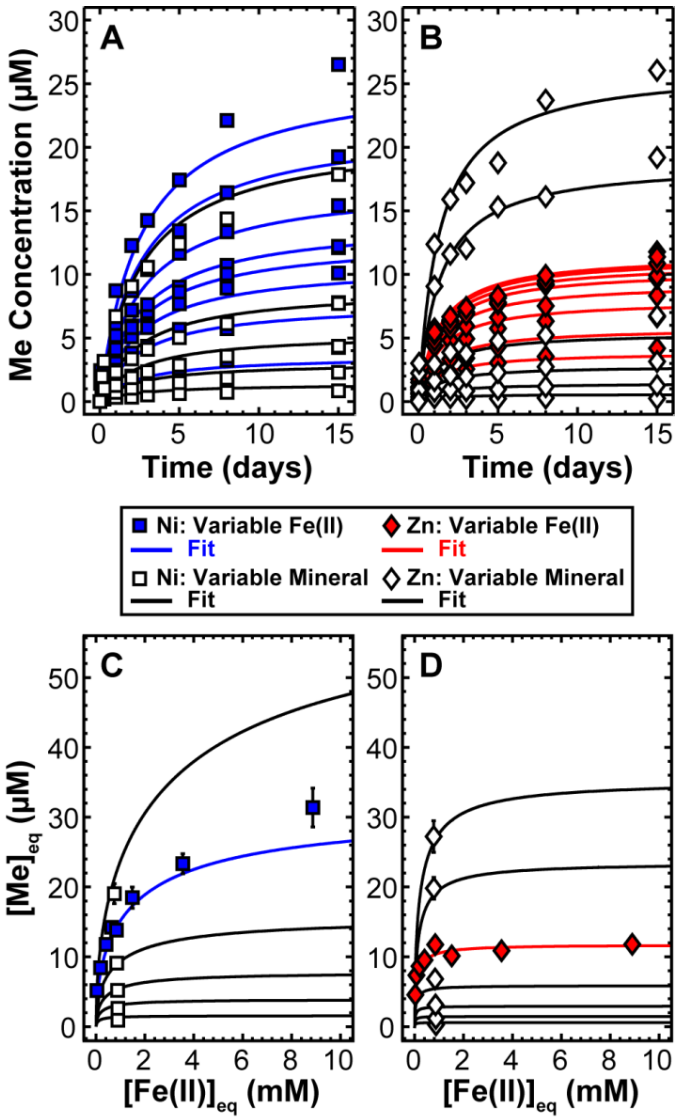

Figure 3-10. Time dependent trace element release for (A) NiGoe and (B) ZnHem with variable initial Fe(II) (filled symbols) and mineral (open symbols) concentrations along with extended model fit (lines). Equilibrium (C) Ni and (D) Zn concentrations as a function of equilibrium Fe(II) concentration for each kinetic series with variable initial Fe(II) and variable mineral loading. Calculated curves show model predictions based on the Langmuir competitive adsorption model and refined fitting parameters (SI Table S3) obtained by fitting the complete data sets (A,B).

CHAPTER 3 APPENDIX

SECTION A1: EXAFS SPECTROSCOPY ANALYSIS OF ZINC SUBSTITUTION IN GOETHITE AND HEMATITE

Data Collection and Analysis

Bulk EXAFS measurements and spectral fitting were performed following methods previously described (Chapter 2). Briefly, data collection was done on beamline 20-BM (PNC/XSD) at the Advanced Photon Source at Argonne National Laboratory in fluorescent yield mode. Beam energy was controlled using a Si(111) double-crystal monochromator, and harmonic content of the X-ray beam was reduced by detuning the second crystal of the monochromator by 10% and by insertion of a Rh-coated harmonic rejection mirror (cutoff energy of ~16 keV) 1 m before the sample. The beam was focused both vertically and horizontally to a size of 700 μm; focusing was primarily done to increase the usable X-ray flux of the beamline.

The X-ray energy was calibrated by setting the maximum in the first derivative of the X-ray absorption near-edge structure spectrum of a Zn metal foil to 9659 eV for the Zn K-edge. The normalized and background subtracted k^3-weighted EXAFS spectra of Zn were quantitatively analyzed in SixPACK using phase and amplitude functions generated from the structures of goethite [α-FeOOH] (Gualtieri and Venturelli, 1999) and hematite [α-Fe_2O_3] (Blake et al., 1966) using FEFF 7.02. (Ankudinov et al., 1998) Coordination number (N), interatomic distance (R), and σ^2 (a Debye–Waller-type factor based on a Gaussian distribution of interatomic distances), were refined using a nonlinear

least-squares fitting routine. The amplitude reduction factor, S_0^2, was fixed to 0.9 for spectral fitting.

Results

The Zn-substituted goethite sample is well fit (Figure A3-1) with a local structural model consisting of Zn occupying an iron site (Table A3-1). These results are similar to those previously reported for Ni-substituted goethite (Chapter 2). The Ni substitution mechanism in hematite also involves replacement of an iron site (Chapter 2). Zn substitution in hematite, however, appears to involve a different substitution mechanism. The Fourier transform (FT) of the Zn EXAFS for ZnHem exhibits a zinc-oxygen shell with a reduced amplitude and negative shift relative to ZnGoe, and is suggestive of tetrahedral coordination (Figure A3-1). Fitting parameters for the oxygen shell (Table A3-1) reveal a coordination number (4±1) and interatomic distance (1.99±2) consistent with tetrahedral Zn (Waychunas et al., 2002). The presence of a substantial second shell in the Fourier transform is clear evidence of structurally incorporated Zn. Neither the EXAFS spectrum nor the resulting interatomic distances agree with the structures of secondary Zn phases such as franklinite or zincite (Waychunas et al., 2002). Attempts to model Zn as being present in the tetrahedral site of a ferrihydrite cluster (Michel et al., 2007) were also unsuccessful. While there is firm evidence for tetrahedrally coordinated Zn within hematite, we cannot conclusively identify its crystallographic location within the hematite structure. Substitution within an otherwise vacant tetrahedral site would necessitate several iron vacancies as the tetrahedral site in hematite is face-sharing with two iron octahedra. In addition, the iron shells are inconsistent with Zn located in a

tetrahedral site even with the aforementioned iron vacancies. However, the first two iron shells used in the fit both yield coordination numbers and interatomic distances that are excellent matches for Zn substitution in an iron site (Table A3-1). The overall fit was substantially improved by inclusion of a third iron shell, though it yielded both a coordination number and interatomic distance substantially less than the theoretical value for an element located in the iron site (Table A3-1). Furthermore, tetrahedral Zn substitution into an iron site would locally distort the structure and necessitate oxygen vacancies and lower coordination of neighboring Fe atoms. An unambiguous conclusion about the substitution mechanism cannot be made due to these discrepancies. Nevertheless, it is clear that Zn is tetrahedrally coordinated, structurally incorporated into hematite, and is not present as a secondary mineral phase.

SECTION A2: CONTROL EXPERIMENTS TO ASSESS THE SOURCE OF RELEASED METAL

Oxalate Washed NiGoe and Ni-ferrihydrite Preparation

An additional Ni-substituted goethite material was prepared as described in Chapter 2 except that it was washed with a 0.2 M ammonium oxalate buffer solution (pH 3) for 2 hrs in the dark at 25°C using a solid to solution ratio of 1:100 (Schwertmann, 1964). This material was then washed with 1 M NaOH followed by 1 M HCl for 2 hr each in an attempt to remove residual oxalate, and lastly, the material was washed free of electrolytes as described above. Particle aggregation, suggestive of residual surface-bound oxalate, prevented full suspension of this material in DI water and so it was

separated from solution by vacuum filtration, dried at 70°C, and stored as a powder until use.

Ni-ferrihydrite was synthesized by the slow addition of 125 mL of a solution containing 0.98 M ferric nitrate and 0.02 M Ni(II) chloride to 225 mL of 5 M NaOH. The slurry was then washed with DI water by centrifugation until circumneutral pH was achieved. This material was used for kinetic experiments within less than 1 week of preparation.

Results

Control experiments confirm that metal release is associated with the substituting element and not an adsorbed species or mineral contaminant. NiGoe exposed to 1 mM aqueous Zn(II), using the same conditions as reactions with Fe(II), results in small amounts of Ni release (Figure A3-2). However, several lines of evidence suggest that the mechanism for this Zn-induced Ni release is not from displacement of surface bound Ni. Zn-induced Ni release from NiGoe occurs on a different timescale than Zn adsorption (Figure A3-2B) onto the solid but on a similar timescale as Ni release promoted by reaction with Fe(II). Zn adsorption is rapid and occurs at a rate similar to Fe(II) adsorption described previously (Figure 3-4). Additionally, the quantity of Ni release from reaction of NiGoe with 1 mM Zn is less than the amount of Ni released by reaction of NiGoe with 0.1 mM Fe(II), all else being constant (Figure A3-2). This suggests that Fe(II) is necessary for substantial metal release. Also, for an equal amount of added Zn or Fe(II), more Zn adsorbs at a given pH. Therefore, if surface displacement were a

contributing mechanism for Ni release, Zn would drive off more Ni than Fe(II); this is not observed.

Residual ferrihydrite also cannot account for the metal release observed in this study. Coprecipitation of additional metals with Fe(III) retards the recrystallization of ferrihydrite to goethite, potentially leaving behind Me-rich ferrihydrite in the final goethite material (Cornell et al., 1992; Giovanoli and Cornel, 1992). Residual ferrihydrite, with or without coprecipitated divalent metals, can be selectively removed from crystalline iron oxides by an oxalate extraction (Schwertmann, 1964; Cornell et al., 1992; Giovanoli and Cornel, 1992). The NiGoe washed with oxalate instead of 0.25 M HCl is used as a comparison for Ni release. Reaction of oxalate washed NiGoe with 10^{-3} M Fe(II) releases Ni at a similar rate and with final Ni concentrations comparable to the HCl washed material (ca. 15% difference). Bulk digestion of the oxalate washed material reveals a Ni content of 1.2 mol% (cf. 1.4% for HCl washed material), 15% less than the HCl-washed material synthesized separately. This suggests that the difference in Ni release is a matter of bulk Ni content rather than an issue related to ferrihydrite contamination. Bulk metal content may not determine the extent of release when comparing different materials (e.g., NiGoe vs. ZnGoe), but changes in metal content in a single solid will result in different amounts of release. Furthermore, reaction of Ni-ferrihydrite (2.0 mol%) with 10^{-3} M Fe(II) at pH 7 exhibits different release kinetics than NiGoe (Figure A3-3). Ni release from Ni-ferrihydrite could not be modeled with a 1st or 2nd order rate law, but instead was modeled using the sum of two 2nd order rates as the majority of the release occurs during an initial fast step, which is followed by a slower release step at longer reaction times. This likely reflects the fact that Fe(II) catalyzes the

complete phase transformation of ferrihydrite to goethite at pH 7 (Figure A3-4) (Hansel et al., 2005). First half-lives of Ni release from ferrihydrite were found to be 2-3 orders of magnitude faster than from NiGoe (Table A3-2).

Table A3-1. XAFS spectra structural fitting results for Zn-substituted iron oxides.

Sample	XAFS						Structure[a]	
	Shell	***N*[b]**	***R* (Å)**	**σ^2 (Å^2)**	**ΔE_0 (eV)**	**χ_ν^2**	***N***	***R* (Å)**
ZnHem	O	4(1)[c]	1.99(2)	0.010(3)	-3(3)	10.3	3, 3	1.946, 2.116
	Fe[d]	4(2)	2.95(2)	0.009(4)[e]	-3(3)		4	2.953
	Fe	3(2)	3.33(3)	0.009(4)	-3(3)		3	3.364
	Fe	1(1)	3.62(7)	0.009(4)	-3(3)		6	3.705
ZnGoe	O	6[f]	2.07(1)	0.0087(6)	-0(2)	6.1	3, 3	1.937, 2.088
	Fe	2	3.01(1)	0.008(1)	-0(2)		2	3.013
	Fe	2	3.29(2)	0.012(3)	-0(2)		2	3.292

[a] Coordination numbers and interatomic distances from iron site derived from the crystal structures of the minerals.
[b] Fixed to crystallographic values for ZnGoe.
[c] Statistical uncertainties in the last digit are reported in parentheses at the 95% confidence level. Parameters with no listed uncertainties were not varied during the analysis.
[d] Represents multiple unresolvable neighbors.
[e] σ^2 fixed for all Fe shells.
[f] Two oxygen shells could not be resolved and a better fit was obtained with a single shell.

Table A3-2. Kinetic fit parameters for Ni release from 2.0 mol% Ni-ferrihydrite in pH 7 fluid.

Parameter	0.2 g/L	1 g/L
Ni Release: Fe(II)-free control		
$[Ni]_{eq}$ (μM)	2.2(1)[a]	1.79(9)
Percent released	6.0(2)	1.0(7)
2nd order rate constant (μmol L^{-1} d^{-1})	-[b]	-
Ni Release: 1 mM Fe(II)		
$[Ni]_{eq}$ (μM)[c]	28(1)	74(7)
Percent released to solution	75(3)	40(4)
2nd order rate constant, fast (μmol L^{-1} d^{-1})	26(6)	37(31)
2nd order rate constant, slow (μmol L^{-1} d^{-1})	0.11(3)	0.07(4)

[a] Statistical uncertainties in the least significant digit(s) are reported in parentheses at the 95% confidence level.
[b] Rate constant could not be calculated because of low release.
[c] Sum of concentrations from fast and slow rate.

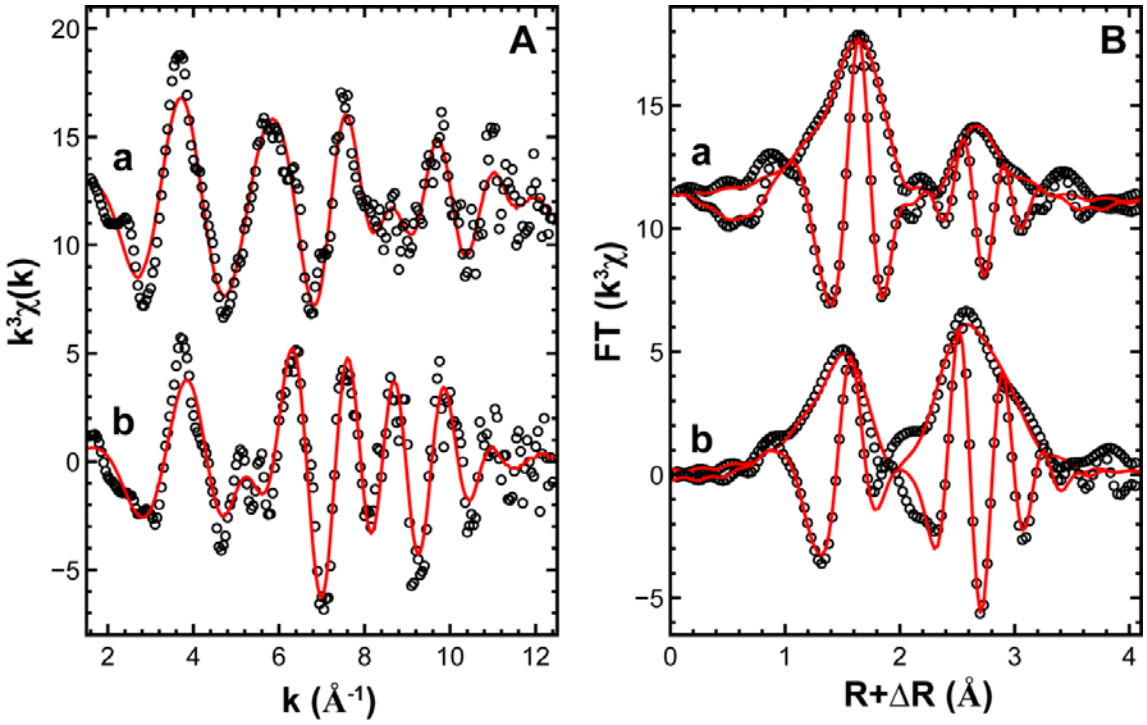

Figure A3-1. (A) Zn K-edge XAFS spectra (points) and structural model fits (lines) for (a) Zn-substituted goethite and (b) Zn-substituted hematite. (B) Fourier transform magnitudes and real components of XAFS spectra (points) and corresponding structural model fits (lines).

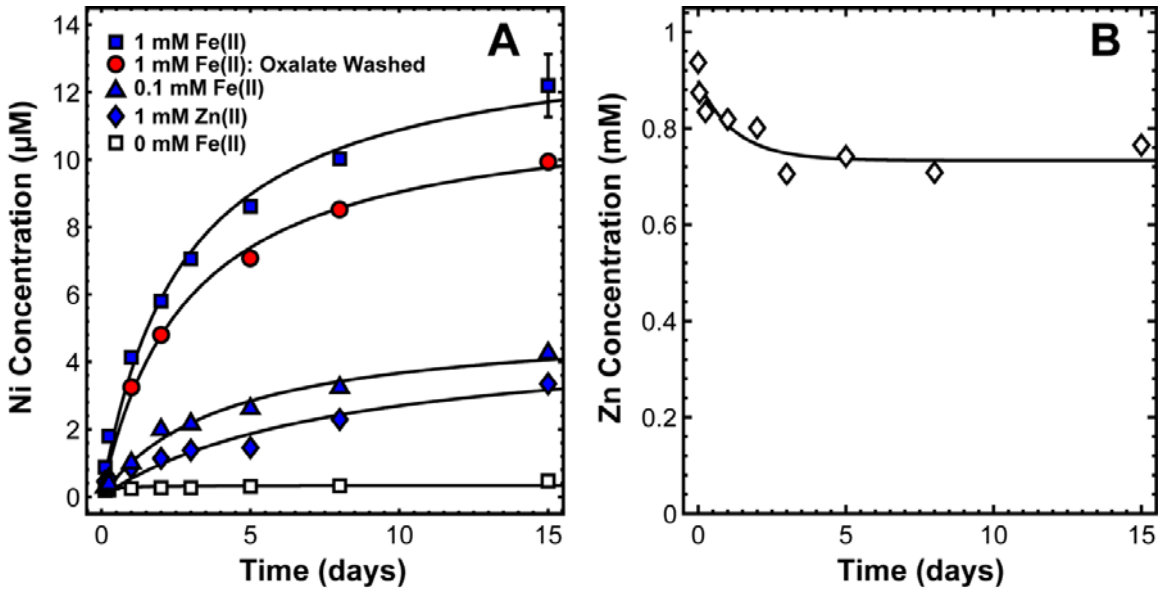

Figure A3-2. (A) Ni release from Ni-substituted goethite washed with HCl or oxalate. HCl washed material is exposed to solutions containing 1.0, 0.1, and 0 mM Fe(II) as well as 1 mM Zn(II). Oxalate washed material is exposed to 1 mM Fe(II). All reactions contain 1 g/L NiGoe, 10 mM NaCl, and 1 mM MOPS (pH 7). (B) Zn adsorption for reaction of 1 mM Zn(II) with NiGoe shown in (A).

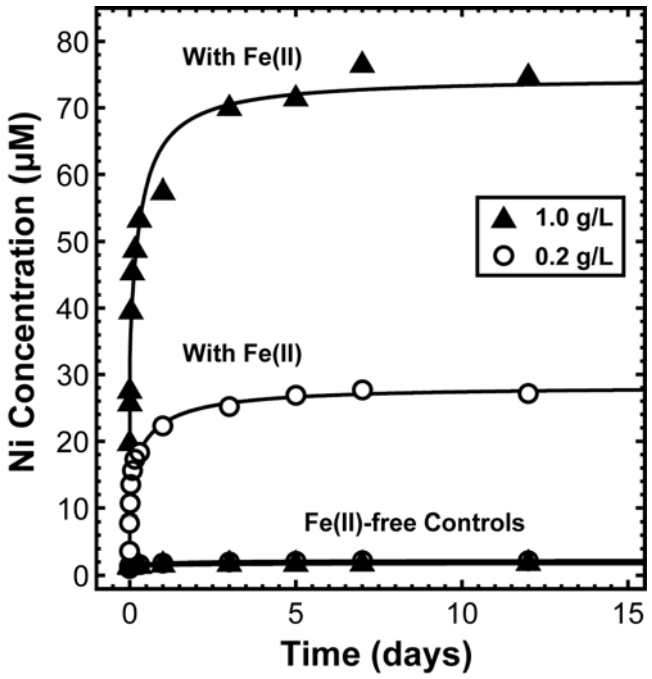

Figure A3-3. Ni release during reaction of Ni-ferrihydrite with 10^{-3} M Fe(II) at pH 7.

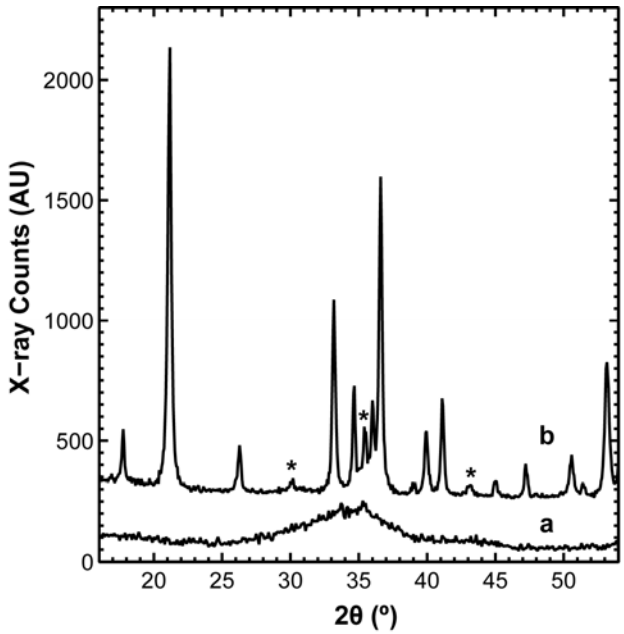

Figure A3-4. XRD patterns of Ni-ferrihydrite **(a)** before and **(b)** after 12 d reaction with 10^{-3} M Fe(II) at pH 7 with 1 g/L Ni-ferrihydrite. XRD lines marked with an asterisk on Fe(II)-reacted sample denote magnetite presence, all other lines are from goethite.

REFERENCES

Amstaetter K., Borch T., Larese-Casanova P., and Kappler A. (2010) Redox transformation of arsenic by Fe(II)-activated goethite (α-FeOOH). *Environ. Sci. Technol.* **44**, 102–108.

Ankudinov A. L., Ravel B., Rehr J. J., and Conradson S. D. (1998) Real-space multiple-scattering calculation and interpretation of x-ray-absorption near-edge structure. *Phys. Rev. B* **58**, 7565–7576.

Bargar J. R., Tebo B. M., Bergmann U., Webb S. M., Glatzel P., Chiu V. Q., and Villalobos M. (2005) Biotic and abiotic products of Mn(II) oxidation by spores of the marine Bacillus sp. strain SG-1. *Am. Mineral.* **90**, 143-154.

Beard B. L., Handler R. M., Scherer M. M., Wu L., Czaja A. D., Heimann A., and Johnson C. M. (2010) Iron isotope fractionation between aqueous ferrous iron and goethite. *Earth Planet. Sc. Lett.* **295**, 241–250.

Berner R. A. (1978) Rate control of mineral dissolution under Earth surface conditions. *Am. J. Sci.* **278**, 1235-1252.

Blake R. L., Hessevick R. E., Zoltai T., and Finger L. W. (1966) Refinement of the hematite structure. *Am. Mineral.* **51**, 123-129.

Boland D. D., Collins R. N., Payne T. E., and Waite T. D. (2011) Effect of amorphous Fe(III) oxide transformation on the Fe(II)-mediated reduction of U(VI). *Environ. Sci. Technol.* **45**, 1327-1333.

Brantley S. L. and Conrad C. F. (2008) Analysis of rates of geochemical reactions. In *Kinetics of water-rock interaction* (ed. S. L. Brantley, J. D. Kubicki, and A. F. White), pp. 1-37. Springer.

Brown G. E., Jr., Henrich V. E., Casey W. H., Clark D. L., Eggleston C., Felmy A., Goodman D. W., Gratzel M., Maciel G., McCarthy M. I., Nealson K. H., Sverjensky D. A., Toney M. J., and Zachara J. M. (1999) Metal oxide surfaces and their interaction with aqueous solutions and microbial organisms. *Chem. Rev.* **99**, 77-174.

Brown G. E., Jr. and Parks G. A. (2001) Sorption of trace elements on mineral surfaces: Modern perspectives from spectroscopic studies, and comments on sorption in the marine environment. *Int. Geol. Rev.* **43**, 963-1073.

Buerge I. J. and Hug S., J. (1999) Influence of mineral surfaces on chromium(VI) reduction by iron(II). *Environ. Sci. Technol.* **33**, 4285–4291.

Catalano J. G., Fenter P., Park C., Zhang Z., and Rosso K. M. (2010) Structure and oxidation state of hematite surfaces reacted with aqueous Fe(II) at acidic and neutral pH. *Geochim. Cosmochim. Acta* **74**, 1498–1512.

Cornell R. M., Giovanoli R., and Schneider W. (1992) The effect of nickel on the conversion of amorphous iron(III) hydroxide into more crystalline iron oxides in alkaline media. *J. Chem. Tech. Biotechnol.* **53**, 73-79.

Cornell R. M. and Schwertmann U. (2003) *The iron oxides: Structure, properties, reactions, occurrences and uses*. Wiley-VCH Verlag GmbH & Co. KGaA.

Coughlin B. R. and Stone A. T. (1995) Nonreversible adsorption of divalent metal ions (Mn(II), Co(II), Ni(II), Cu(II), and Pb(II)) onto goethite: Effects of acidification, Fe(II) addition, and picolinic acid addition. *Environ. Sci. Technol.* **29**, 2445–2455.

Elsner M., Schwarzenbach R. P., and Haderlein S. (2004) Reactivity of Fe(II)-bearing minerals toward reductive transformation of organic contaminants. *Environ. Sci. Technol.* **38**, 799–807.

Frierdich A. J., Hasenmueller E. A., and Catalano J. G. (2011) Composition and structure of nanocrystalline Fe and Mn oxide cave deposits: Implications for trace element mobility in karst systems. *Chem. Geol.* **284**, 82-96.

Giovanoli R. and Cornel R. M. (1992) Crystallization of metal substituted ferrihydrites. *Z. Pflanzenernähr. Bodenk.* **155**, 455–460.

Gualtieri A. and Venturelli P. (1999) In situ study of the goethite-hematite phase transformation by real time, synchrotron powder diffraction. *Am. Mineral.* **84**, 895–904.

Haderlein S. and Pecher K. (1998) Pollutant reduction in heterogeneous Fe(II)-Fe(III) systems. In *Mineral-water interfacial reactions: Kinetics and mechanisms*, Vol. 715: ACS Symposium Series (ed. D. L. Sparks and T. J. Grundl), pp. 342-357. American Chemical Society.

Handler R. M., Beard B. L., Johnson C. M., and Scherer M. M. (2009) Atom exchange between aqueous Fe(II) and goethite: An Fe isotope tracer study. *Environ. Sci. Technol.* **43**, 1102–1107.

Hansel C. M., Benner S. G., and Fendorf S. (2005) Competing Fe(II)-induced mineralization pathways of ferrihydrite. *Environ. Sci. Technol.* **39**, 7147–7153.

Hofstetter T. B., Schwarzenbach R. P., and Haderlein S. B. (2003) Reactivity of Fe(II) species associated with clay minerals. *Environ. Sci. Technol.* **37**, 519-528.

Jeon B.-H., Dempsey B. A., Burgos W. D., and Royer R. A. (2003) Sorption kinetics of Fe(II), Zn(II), Co(II), Ni(II), Cd(II), and Fe(II)/Me(II) onto hematite. *Water Res.* **37**, 4135–4142.

Larese-Casanova P. and Scherer M. M. (2007) Fe(II) sorption on hematite: New insights based on spectroscopic measurements. *Environ. Sci. Technol.* **41**, 471–477.

Liger E., Charlet L., and Cappellen P. V. (1999) Surface catalysis of uranium(VI) reduction by iron(II). *Geochim. Cosmochim. Acta* **63**, 2939–2955.

Michel F. M., Ehm L., Antao S. M., Lee P. L., Chupas P. J., Liu G., Strongin D. R., Schoonen M. A. A., Phillips B. L., and Parise J. B. (2007) The structure of ferrihydrite, a nanocrystalline material. *Science* **316**, 1726-1729.

Mikutta C., Wiederhold J. G., Cirpka O. A., Hofstetter T. B., Bourdon B., and Gunten U. V. (2009) Iron isotope fractionation and atom exchange during sorption of ferrous iron to mineral surfaces. *Geochim. Cosmochim. Acta* **73**, 1795–1812.

Pedersen H. D., Postma D., Jakobsen R., and Larsen O. (2005) Fast transformation of iron oxyhydroxides by the catalytic action of aqueous Fe(II). *Geochim. Cosmochim. Acta* **69**, 3967–3977.

Rosso K. M., Yanina S. V., Gorski C. A., Larese-Casanova P., and Scherer M. M. (2010) Connecting observations of hematite (α-Fe_2O_3) growth catalyzed by Fe(II). *Environ. Sci. Technol.* **44**, 61–67.

Schaefer M. V., Gorski C. A., and Scherer M. M. (2011) Spectroscopic evidence for interfacial Fe(II)-Fe(III) electron transfer in a clay mineral. *Environ. Sci. Technol.* **45**, 540-545.

Schwertmann U. (1964) Differenzierung der eisenoxide des boden durch extraktion mit ammoniumoxalat-lösung. *Z. Pflanzenernähr. Bodenk.* **105**, 194–202.

Schwertmann U. and Cornell R. M. (2000) *Iron oxides in the laboratory: Preparation and characterization*. Wiley-VCH.

Vannice M. A. (2005) *Kinetics of catalytic reactions*. Springer.

Waychunas G. A., Fuller C. C., and Davis J. A. (2002) Surface complexation and precipitate geometry for aqueous Zn(II) sorption on ferrihydrite I: X-ray absorption extended fine structure spectroscopy analysis. *Geochim. Cosmochim. Acta* **66**, 1119–1137.

Williams A. G. B. and Scherer M. M. (2004) Spectroscopic evidence for Fe(II)-Fe(III) electron transfer at the iron oxide-water interface. *Environ. Sci. Technol.* **38**, 4782–4790.

Wu L., Beard B. L., Roden E. E., Kennedy C. B., and Johnson C. M. (2010) Stable Fe isotope fractionations produced by aqueous Fe(II)-hematite surface interactions. *Geochim. Cosmochim. Acta* **74**, 4249–4265.

Yanina S. V. and Rosso K. M. (2008) Linked reactivity at mineral-water interfaces through bulk crystal conduction. *Science* **320**, 218–222.

Zhang J.-W. and Nancollas G. H. (1990) Mechanisms of growth and dissolution of sparingly soluble salts. *Rev. Mineral. Geochem.* **23**, 365-396.

Zhu M., Ginger-Vogel M., Parikh S., Feng X.-H., and Sparks D. L. (2010) Cation effects on the layer structure of biogenic Mn-oxides. *Environ. Sci. Technol.* **44**, 4465-4471.

CHAPTER 4

INHIBITION OF TRACE ELEMENT RELEASE DURING IRON(II)-ACTIVATED RECRYSTALLIZATION OF ALUMINUM-, CHROMIUM-, AND TIN-SUBSTITUTED IRON OXIDE MINERALS

To be submitted to *Environmental Science and Technology* as:

Frierdich, A.J., Scherer, M. M., Bachman, J., Engelhard, M.H., Catalano J.G. (2012) Inhibition of trace element release during iron(II) activated recrystallization of aluminum-, chromium-, and tin-substituted iron oxide minerals.

ABSTRACT

Aqueous Fe(II) reacts with Fe(III) oxides by coupled electron transfer and atom exchange (ETAE) resulting in mineral recrystallization, contaminant reduction, and trace element cycling. Previous studies of Fe(II)-Fe(III) ETAE have explored the reactivity of either pure iron oxide phases or those containing small quantities of soluble trace elements. Naturally occurring iron oxides, however, contain substantial quantities of insoluble impurities (e.g., Al) which are known to affect the chemical properties of such minerals. Here we explore the effect of Al(III), Cr(III), and Sn(IV) substitution on trace element release from Ni(II)-substituted goethite and Zn(II)-substituted hematite during reaction with aqueous Fe(II). Fe(II)-activated trace element release is substantially inhibited from both minerals when an insoluble element is co-substituted into the structure, and the total amount of release decreases exponentially with increasing co-substituent. The limited changes in surface composition that occur following reaction with Fe(II) indicate that Al, Cr, and Sn do not exsolve from the structure and that Ni and Zn released to solution originate primarily from the bulk rather than the particle exterior (upper ~3 nm). Incorporation of Al into goethite substantially decreases the amount of Fe atom exchange with aqueous Fe(II) and, consequently, the amount of Ni release from the structure. This implies that trace element release inhibition caused by substituting insoluble elements results from a decrease in the amount of mineral recrystallization. These results suggest that naturally occurring iron oxides containing insoluble elements are less susceptible to Fe(II)-activated recrystallization and exhibit a greater retention of trace elements and contaminants than pure mineral phases.

INTRODUCTION

Iron oxide minerals are ubiquitous in sedimentary environments and act as sinks for trace elements, many of which are micronutrients as well as contaminants (Brown et al., 1999; Cornell and Schwertmann, 2003). Biogeochemical iron cycling directly affects trace element fate via co-precipitation with iron oxides during Fe(II) oxidation or by release to solution from dissolving iron oxides during dissimilatory Fe(III) reduction (Roden and Emerson., 2007). The coexistence of Fe(II) and Fe(III) in a system is often the result of such iron cycling and may initiate secondary abiotic reactions involving electron transfer and atom exchange (ETAE) between aqueous Fe(II) and an Fe(III) oxide surface (Williams and Scherer, 2004; Pedersen et al., 2005; Larese-Casanova and Scherer, 2007; Yanina and Rosso, 2008; Handler et al., 2009; Rosso et al., 2010). Fe(II)-Fe(III) ETAE involves coupled Fe(II) oxidative adsorption and structural Fe(III) reductive dissolution, resulting in the recrystallization of stable iron oxides (e.g., goethite and hematite) without causing a phase transition. The regular occurrence of trace elements in iron oxides and the frequency of biogeochemical iron cycling at redox gradients suggests that Fe(II)-Fe(III) ETAE may substantially affect nutrient and contaminant fate in natural and engineered systems.

The abiotic reduction of organic contaminants, heavy metals, and radionuclides by Fe(II) on Fe(III) oxide surfaces has been studied extensively (Klausen et al., 1995; Charlet et al., 1998; Haderlein and Pecher, 1998; Buerge and Hug, 1999; Liger et al., 1999; Hofstetter et al., 2003; Strathmann and Stone, 2003; Elsner et al., 2004; Felmy et al., 2011) but the effect of Fe(II) on redox-inactive trace elements is less clear. Zn(II) incorporation into goethite has been postulated following microbial iron reduction of goethite containing adsorbed Zn (Cooper et al., 2000; Cooper et al., 2005); no

incorporation was apparent in the absence of Fe(II) production. Similar abiotic experiments examining divalent metal adsorption onto goethite also suggest that Fe(II) promotes the incorporation of trace elements (Coughlin and Stone, 1995). More recently, Frierdich et al. (2011) established that Ni(II) adsorbed to goethite and hematite progressively incorporates into the mineral structures during reaction with Fe(II) while Ni pre-incorporated into the structure is released to solution. Frierdich and Catalano (2012) demonstrated that the rate and total amount of release of structurally-incorporated Ni and Zn from goethite and hematite depends primarily on the amount of Fe(II) sorption, and showed that even low concentrations of aqueous Fe(II) can mobilize structurally-incorporated trace elements from iron oxides in the absence of net iron reduction.

Prior studies of Fe(II)-Fe(III) ETAE have utilized iron oxides that were either pure (Williams and Scherer, 2004; Pedersen et al., 2005; Larese-Casanova and Scherer, 2007; Yanina and Rosso, 2008; Handler et al., 2009; Mikutta et al., 2009; Beard et al., 2010) or contained minor (<2 mol%) amounts of structurally incorporated redox-inactive trace elements (Frierdich et al., 2011; Frierdich and Catalano, 2012). Naturally occurring iron oxides, however, often contain impurities, e.g., Al, Cr, and Sn (Singh and Gilkes, 1992; Trolard et al., 1995; Cornell and Schwertmann, 2003), which alter iron oxide reactivity. For example, Al incorporation into iron oxides inhibits microbial iron reduction (Bousserrhine et al., 1999), abiotic reductive dissolution (Torrent et al., 1987), the Fe(II)-induced transformation of ferrihydrite to more crystalline phases (Hansel et al., 2011), and contaminant reduction by magnetite (Jentzsch et al., 2007). The effect of insoluble substituting elements, such as Al, Cr, and Sn, on Fe(II)-Fe(III) ETAE or on Fe(II)-activated trace element release is unknown.

Here we explore Ni(II) and Zn(II) release from a series of Ni-substituted goethites and Zn-substituted hematites containing variable quantities of the insoluble co-substituents Al(III), Cr(III), or Sn(IV) during reaction of these minerals with aqueous Fe(II). The properties of these co-substituted iron oxides are presented along with kinetic data for Ni and Zn release during Fe(II)-activated recrystallization of iron oxides. Select samples were collected following reaction with Fe(II) and characterized by stoichiometric dissolution experiments, transmission electron microscopy (TEM), and X-ray photoelectron spectroscopy (XPS) to identify changes in surface composition and structure. Additionally, iron atom exchange between aqueous Fe(II) and several goethite samples was monitored simultaneously with trace element release for the first time to correlate these two processes in iron oxides with and without Al-substitution.

METHODS

Mineral Syntheses

The mineral syntheses carried out in this work are similar to our methods for Ni- and Zn-substituted goethite and hematite reported in Chapters 2 and 3 but modified to also incorporate Al, Cr, and Sn; all are modifications of standard techniques (Schwertmann and Cornell, 2000). The amount of Al, Cr, or Sn co-precipitated with Fe and Ni or Zn was varied to yield final products with target compositions of 1, 2, 4, or 8 mol% of co-substituent. Polypropylene labware was used instead of glass to prevent contamination from Si. A goethite material containing a target Ni and Al substitution of 2 and 1 mol%, respectively, was synthesized by slowly adding 99 mL of a solution containing 0.97 M iron(III) nitrate and 0.02 M nickel(II) chloride to 180 mL of 5 M

NaOH also containing 0.002 moles of $Al(OH)_4^-$ (added as aluminum(III) chloride). As roughly half of the Al initially co-precipitated actually incorporates into the final product (Schwertmann and Cornell, 2000), twice the number of moles of Al were added initially to yield a product with the desired composition. This procedure was repeated with increasing amounts of Al present in the 180 mL of 5 M NaOH and less Fe(III) added to yield final products with a target composition of Ni:Al (mol%:mol%) of 2:2, 2:4, and 2:8. The slurries containing the co-precipitates were diluted to 1 L and placed in an oven at 70° C for 14 days.

A hematite material containing a target Zn and Al substitution of 2 and 1 mol%, respectively, was synthesized by slowly adding 500 mL of a solution containing 0.2113 M iron(III) nitrate and 0.0044 M zinc(II) chloride to 330 mL of 1 M NaOH containing 0.0033 M $Al(OH)_4^-$ (added as aluminum(III) chloride). The pH of this slurry was then adjusted to 8 by dropwise addition of 1.0 or 0.1 M NaOH during continuous stirring. This was followed by the addition of 10 mL of 1 M EPPS (4-(2-Hydroxyethyl)-1-piperazinepropanesulfonic acid) to buffer the pH. The suspension was then diluted to 1 L, the pH was readjusted to 8, and it was then placed in an oven set to 98 °C for 5 days. This procedure was repeated with increasing amounts of Al present in the 330 mL of 1 M NaOH and less Fe(III) added to yield final products with a target composition of Zn:Al (mol%:mol%) of 2:2, 2:4, and 2:8.

These synthesis procedures were followed for Cr-substituted materials with two modifications. First, for the preparation of Ni and Cr co-substituted goethite, only 1.5 times the amount of Cr was co-precipitated relative to the desired target in the product since our previous experience with preparing Cr-substituted goethite (data not shown)

and prior work (Schwertmann and Cornell, 2000) has shown that only a fraction of co-precipitated Cr incorporates into goethite. Second, after quantification of Ni, Zn, and Al in the Al-substituted iron oxides it was found that as the amount of Al increased in the final product the amount of Ni or Zn decreased (Table 4-1). Based on this relationship, additional amounts of Ni and Zn were co-precipitated with Fe and Cr as to maintain the amount of Ni and Zn in the final co-substituted product close to the same mol% as singly-substituted NiGoe and ZnHem. This technique was repeated for the synthesis of Sn-substituted iron oxides but with Sn present in the Fe(III) solution upon co-precipitation with NaOH. The mol% of Sn co-precipitated with Fe and Ni or Zn was the same as that desired in the final product. After preparation, all materials were treated with 1 M HCl for 2 h at a solid to solution mass ratio of 1:100 to remove residual adsorbed cations and metal hydroxides and then washed free of electrolytes using de-ionized (DI) water (>18.2 MΩ·cm).

Mineral Characterization

Quantitative mineral compositions were determined using inductively-coupled plasma optical emission spectrometry (ICP-OES, Perkin-Elmer Optima 7300DV) after solid digestion in a 20% HNO_3:5% HCl mixture (trace metal grade, Fisher Scientific) at 70°C. Dissolution stoichiometry was determined separately by adding 10 mg of co-substituted iron oxide to 100 mL of 4 M HCl at 70°C; samples were collected periodically then filtered, diluted, and analyzed by ICP-OES. X-ray diffraction (XRD) was performed on a Rigaku Geigerflex D-MAX/A diffractometer using Cu-Kα radiation (0.02° $step^{-1}$). Unit cell parameters were calculated with Jade 9.0 software after 2θ

calibrations using a Si (99%, -325 mesh, Sigma-Aldrich) internal standard. Crystal morphology and particle size were examined using a JEOL JSM-7001F field emission scanning electron microscope (SEM) operated at 30 kV; samples were Au coated by plasma deposition (Cressington Sputter Coater 108) to improve image quality.

The potential for Al-, Cr-, and Sn-phase impurities occurring with/on iron oxide particles was examined with TEM using a JEOL 2100F operated at 200 kV. Surface compositions (~upper 3 nm) were determined by XPS measurements conducted at the Environmental Molecular Sciences Laboratory (EMSL) at Pacific Northwest National Laboratory using a Physical Electronics Quantera Scanning X-ray Microprobe with a focused monochromatic Al Kα X-ray (1486.7 eV) source for excitation and a spherical section analyzer equipped with a 32 element multichannel detection system. An X-ray beam focused to 100 μm diameter was rastered over a 1.3 mm x 0.1 mm rectangle on the sample. The X-ray beam was incident normal to the sample and the photoelectron detector was at 45° off-normal. High-resolution energy spectra were collected using a pass-energy of 69.0 eV with a step size of 0.125 eV. Surface-charging was minimized by flooding the sample with low energy electrons and Ar^+. The binding energy of the C 1s line was set at 285.0 eV to compensate for surface-charging effects. A hydrocarbon over-layer correction (Smith, 2005) was employed for element quantification. BET surface area was measured by N_2 adsorption using a Quantachrome Instruments Autosorb-1. Fluorescence-yield Ni and Zn K-edge extended X-ray absorption fine structure (EXAFS) spectra were collected at the Advanced Photon Source at beamline 5-BM-D to determine the metal substitution mechanism (Appendix Section A1).

Trace Element Release Experiments

Anoxic experimental conditions were maintained using an anaerobic chamber (4% H_2/96% N_2 atmosphere) and Pd catalysts to eliminate residual O_2. Trace O_2 and CO_2 contents in the chamber, as well as in DI water used for experiments, were further lowered using methods described in Chapter 2. Dissolved oxygen in DI water was measured colorimetrically (CHEMetrics test kit K-7511) prior to use and was always below the detection limit of 1 μg/L. Fe(II) stock solutions were prepared from reagent-grade $FeCl_2$•$4H_2O$, then filtered (0.2 μm, MCE) and stored in amber plastic bottles (to prevent photo-oxidation) prior to use.

Kinetic experiments were performed as described in Chapter 3. All reaction conditions were either 0 or 10^{-3} M initial Fe(II), 10^{-2} M NaCl (electrolyte), and 10^{-3} M 3-(N-Morpholino)propanesulfonic acid (MOPS, pH buffer) at pH 7; pH drift was minimal (± 0.1 pH unit) throughout the reaction. Electrolyte, Fe(II), and buffer were added from a concentrated stock solution and diluted accordingly. A kinetic experiment was initiated by spiking the reactor solution with the target mineral from a concentrated aqueous stock suspension resulting in a final reactor volume of 10 mL. All reactions were normalized by Ni or Zn added: 150 μM substituted-Ni for goethite and 240 μM substituted-Zn for hematite. This was done to compare Ni or Zn release between materials containing different amounts of Al, Cr, or Sn, since increasing the level of co-substituent affects the mineral specific surface area and the mol% of substituted Ni or Zn.

Samples were collected at defined intervals by removing the entire suspension with a syringe and immediately filtering (0.2 μm, MCE) the aliquot to remove the iron oxide particles and stop the reaction. The filtrate was then acidified (HNO_3, trace metal

grade) inside the anaerobic chamber. Metal concentrations were measured by ICP-OES; all soluble iron was assumed to be Fe(II) as Fe(III) solubility is below the ICP-OES detection limit. Each kinetic time-series was modeled by a second-order rate law for mineral dissolution (Berner, 1978; Zhang and Nancollas, 1990), in which the rate of Me release is proportional to the square of the undersaturation Me concentration (Appendix eq A4-1). Integration of eq A4-1 yields the time-dependent Me concentration:

$$[Me] = \frac{[Me]_{eq}{}^2 k_{obs} t}{1 + [Me]_{eq} k_{obs} t} \tag{4-1}$$

where t is time (days), $[Me]$ is metal concentration (μM) at time t, $[Me]_{eq}$ is the equilibrium Me concentration (μM), and k_{obs} is a pseudo second-order rate constant (μM^{-1} d^{-1}).

To examine potential changes in co-substituent speciation following reaction with Fe(II), additional reactions with samples containing the highest levels of co-substituent were reacted with 10^{-3} M Fe(II) or Fe(II)-free fluids at pH 7 and a suspension volume of 40 mL to provide enough solid for material characterization. After 15 days of reaction, the suspension was filtered under anaerobic conditions and then the solid was flushed with 10 mL of DI water to remove NaCl and buffer. The solids were air-dried and characterized by acid dissolution, TEM, and XPS to identify changes in surface composition.

Atom Exchange Experiments

Atom exchange kinetics were determined at pH 7.0 with a 1 mM 3-(N-morpholino)propanesulfonic acid (MOPS) buffer and 10 mM KCl electrolyte. A solution of ^{57}Fe(II) was made by dissolving ^{57}Fe(0) powder (>95%, ISOFLEX) in concentrated

HCl in an anaerobic glove box (96% N_2, 4%H_2) to yield a final solution of 100 mM Fe(II) and 0.1 M HCl. Parent reactors were spiked with Fe(II) to yield a final solution of 1 mM upon experiment initiation. Initial Fe(II) concentrations were taken and aliquots were made into triplicate reactors in polypropylene tubes. The kinetic experiments were initiated by adding the appropriate volume of goethite suspension to yield a final reactor volume of 10 mL and a solids loading of 1 g L^{-1}. Reactors were then wrapped in aluminum foil to avoid photo-oxidation and spun on a rotator for between 10 minutes and 10 days. Reactions were terminated by sealing reactors and centrifuging. The aqueous phase was then separated from the solids and filtered (0.22 μm nylon) and acidified with 50 μL of concentrated HCl, while the solids were dissolved in 5 mL of concentrated HCl. The final Fe(II) and total Fe concentrations of the solids and aqueous phase were determined using the 1,10-phenanthroline method (Schilt, 1969) as discussed in prior work (Williams and Scherer, 2004). Samples were then diluted in a 2% HNO_3 matrix to analyze isotopic composition. Isotope analyses were made on a Thermo-Fisher Scientific X Series 2 quadrupole ICP-Mass Spectrometer operating in collision cell mode with a glass concentric nebulizer and a HEPA filtered autosampler. The collision cell gas was Ar with a flow rate of 1 mL min^{-1}.

RESULTS

Properties of Co-substituted Iron Oxides

Compositional analyses show that most co-substituents associated with goethite and hematite are close to the target compositions of 1, 2, 4, and 8 mol% (Table 4-1). The substitution of some elements, however, is unfavorable as indicated by the low contents

associated with the final product relative to the amount originally co-precipitated with Fe and Ni or Zn. Cr substitution, especially, is limited in hematite with only about 1.2 mol% associated with the solid despite a target of 8 mol% (Table 4-1). Sn and Cr substitution in goethite is also moderately limited for the samples containing the highest levels of co-substituent. Zn, Cr, and Sn substituted in hematite exhibit congruent dissolution with Fe, indicating that they are homogeneously distributed throughout the minerals, while Al dissolution lags Fe dissolution, suggesting enrichment within the interior of the particles (Figure 4-1). Incongruent dissolution of Ni, Al, and Sn from goethite suggests enrichment near the periphery whereas Cr appears to be homogeneously substituted (Figure 4-1).

The surface composition of most elements determined by XPS (Table 4-2) differs from the bulk concentration (Table 4-1), with substantial Ni enrichment and moderate Zn depletion. Cr and Sn are also enriched at the surface of both minerals relative to the bulk whereas Al is unchanged for goethite but depleted for hematite. While these qualitative trends are likely valid (e.g., Ni surface enrichment is consistent with its non-stoichiometric dissolution behavior, Figure 4-1) given the precision of XPS, the reported absolute concentrations suffer from systematic errors associated with empirical XPS sensitivity factors and the correction for C over-layers. These values are thus only semi-quantitative and likely of low accuracy.

XRD patterns demonstrate that all materials are free of crystalline impurities (data not shown). The unit-cell parameters for goethite and hematite decrease with increasing Al and Cr content whereas a unit-cell expansion is observed for increasing Sn contents (Figures 4-2,4-3). These observations are consistent with Vegard's Law considering the size of the co-substituents; Al^{3+} and Cr^{3+} have smaller ionic radii than Fe^{3+} whereas Sn^{4+}

is larger (Shannon, 1976). The effect of Sn substitution on the goethite unit cell size is less than that for hematite.

Al substitution into goethite and hematite affects particle size and morphology, with goethite crystal size decreasing along [001] and expanding along [100] and [010] (Figure 4-4D); Al limits hematite growth along [001] resulting in particles with a platelet morphology (Figure 4-5D). Cr and Sn substitution have little influence on goethite properties whereas substitution into hematite results in smaller particles with higher specific surface areas than singly-substituted ZnHem. At high Sn substitution, particles develop a rod-like morphology (Figure 4-5). Ni and Zn K-edge EXAFS spectra for goethite and hematite containing the highest quantities of each co-substituent are consistent with Ni and Zn substituted within the crystal structure of these minerals (Appendix Table A1), similar to singly-substituted NiGoe and ZnHem (See Chapter 2 and 3). Evidence for trace element clustering with Al and Sn is apparent for both goethite and hematite. Such clustering may occur for Cr but EXAFS cannot distinguish Cr from Fe given their similar atomic numbers and electron scattering properties; the occurrence of Cr clustering around Ni and Zn is thus unclear (Appendix Section A1).

Trace Element Release Inhibition

Iron oxide minerals containing Ni or Zn and variable amounts of Al, Cr, or Sn were reacted with Fe(II) and Fe(II)-free solutions at pH 7 to examine how the co-incorporation of insoluble elements affects the release of trace elements. Suspension of co-substituted iron oxides in a 10^{-3} M Fe(II) solution results in substantially greater amounts of Ni and Zn release compared to exposure of the same materials to an Fe(II)-

free solution (Figure 4-6). Ni and Zn release from all co-substituted iron oxides, however, is less than from singly-substituted NiGoe and ZnHem, and the amount of release progressively decreases as the amount of co-substituent increases. This trend holds for all twenty-four co-substituted materials examined in this study. Trace element release from all materials is modeled well using a second-order kinetic rate law consistent with surface reaction limited mineral dissolution (Berner, 1978; Zhang and Nancollas, 1990). This is in agreement with our prior work on Ni and Zn release (Chapters 2 and 3) and suggests that the presence of co-substituents does not change the trace element release mechanism (i.e., release occurs during reductive dissolution caused by Fe(II)-Fe(III) ETAE). Aqueous Al, Cr, and Sn were not detected (the solubility of all co-substituents at pH 7 is lower than ICP-OES detection limits) and dissolved Fe was not observed in Fe(II)-free controls.

Although no apparent change in the overall mechanism for Ni and Zn release occurs with increasing the amount of co-substituent, the amount of release is substantially affected. The equilibrium Ni and Zn concentrations, determined from second-order fits (eq 4-1) of Ni or Zn release from each material, exponentially decrease with increasing co-substituent (Figure 4-7). This illustrates that small amounts of added co-substituent substantially reduce total trace element release. Additionally, many of the exponential curves predict that trace element release does not approach zero with increasing co-substituent, indicating that naturally occurring iron oxides with large quantities (up to 30 mol%) of Al (Fitzpatrick and Schwertmann, 1982) may still release trace elements if exposed to Fe(II). The exponential form may represent a thermodynamic relationship between mineral recrystallization and trace element repartitioning. The rate of Ni release

from goethite, based on the master rate constant (k, $k = [Me]_{eq} \times k_{obs}$) (Chapter 3), changes little with Al and Sn concentration (Table 4-1). Cr substitution into goethite, however, decreases the rate of Ni release similarly for all Cr concentrations. The rate of Zn release from hematite is unaffected, within error, upon co-substitution with Al, Cr, and Sn (Table 4-1).

Post-reaction Surface Composition and Structure

Ni-substituted goethite and Zn-substituted hematite containing the highest levels of Al, Cr, and Sn were collected following reaction with Fe(II) and characterized to investigate the trace element release inhibition mechanism. High resolution TEM imaging of several particles of each material suggests that no substantial co-substituent enrichment occurs at the particle edges nor does a separate phase exsolve from the bulk following reaction with Fe(II). All particles imaged reveal continuous lattice fringes extending from the particle interior to the edge suggesting that after reaction with Fe(II) the structure of the bulk particle differs little from that of the periphery (Figures 4-8,4-9).

A full spectrum compositional analysis by XPS indicates that reaction with Fe(II) does cause subtle changes in the surface composition for most materials, with evidence for both surface enrichment and depletion of co-substituents and depletion of trace elements. The surface composition of goethite is slightly depleted in Al, Cr, and Sn following reaction with Fe(II) whereas a slight enrichment in Al and Sn is observed for hematite (Table 4-2). Materials reacted with Fe(II) relative to those exposed to an Fe(II)-free control solution all show a depletion in Ni and Zn (Table 4-2). These trends are apparent in most of the iron normalized XPS spectra of Al, Cr, Sn, Ni, and Zn (Figure 4-

10) although subtle changes may not be evident in individual narrow-scan spectra depending on the relative compositions of other elements. The O 1s binding energy is similar for iron oxide materials of the same phase containing Al and Cr while materials containing Sn display a substantial O 1s binding energy shift to higher energy (Figure 4-10), suggesting the presence of near-surface hydroxyl groups (Liu et al., 1998). Two singly-substituted Al-substituted iron oxides (AlGoe and AlHem) containing less Al (ca. 2 mol%) than the co-substituted materials were also examined to determine if the concentration of co-substituent affects the repartitioning behavior. After reaction with Fe(II), an increase in the surface concentration of Al occurs on hematite whereas little change is apparent for goethite (Table 4-2, Figure 4-11); both results are consistent with those of the co-substituted iron oxides containing higher Al contents.

Dissolution stoichiometry of iron oxides following reaction with Fe(II) is consistent with the compositional data obtained by XPS. For example, co-substituents are not substantially redistributed from the bulk to the surface, the only observed near-surface enrichment of co-substituents occurs for Al and Sn on hematite, and Ni and Zn surface concentrations are depleted (Figure 4-12). Taken in whole, the TEM, XPS, and dissolution stoichiometry data are consistent but reveal no major accumulation of insoluble co-substituents on the surface indicating that mineral recrystallization is inhibited or occurs via a mechanism that prevents the repartitioning of these elements.

Iron Atom Exchange of Ni- and Al-substituted Goethite

Atom exchange between aqueous Fe(II) and a series of goethite samples was monitored to determine how the substitutions of Ni, Al, and Ni co-substituted with Al

affect recrystallization and its correlation with Ni release. Complete (>96% ± 3%) Fe isotope equilibrium between pure goethite and aqueous Fe(II) occurs within 10 days (Figure 4-13); this is consistent with prior studies (Handler et al., 2009; Beard et al., 2010). Extensive atom exchange also occurs readily for NiGoe (91% ± 4%) within the 10 day period while Ni is simultaneously released to solution (Figure 4-13) at levels comparable to earlier work (Chapter 2, Figure 4-6). A substantial decrease in the amount of atom exchange occurs upon Al-substitution into goethite (60% ± 10% exchange) (Figure 4-13). A slight depletion in surface Al occurs for AlGoe following reaction with Fe(II) (Table 4-2), yet more than half of the structural Fe(III) exchanges with aqueous Fe(II), demonstrating that changes in surface composition are poor indicators of the amount of Fe(II)-activated recrystallization. When Ni and Al are co-substituted into goethite, the amount of iron isotope exchange is inhibited (47% ± 5% exchange) and similar to AlGoe (Figure 4-13). Furthermore, the amount of Ni release is substantially less than that observed for NiGoe (Figure 4-13B). The slight variation in iron atom exchange between the goethite samples containing Al may be due to the small differences in Al content (Table 4-1). About half of the amount of recrystallization and Ni release occur for NiAlGoe-2 compared to NiGoe (Figure 4-13B), thus providing evidence that the amount of Ni release is directly related to the amount of recrystallization of these materials.

DISCUSSION

Connecting Atom Exchange and Trace Element Release

The relationship between iron atom exchange and Ni release from goethite is an essential first step towards reconciliation of these two phenomena. The atom exchange data for NiGoe demonstrates that the absolute amount of trace element release from an iron oxide may be substantially less than the recrystallization that has occurred. For example, more than 90% iron atom exchange occurs for NiGoe in 10 days while about 6% of the total incorporated Ni is released to solution. This observation demonstrates that the amount of trace element release to solution can substantially differ from the percentage of particle volume that undergoes recrystallization. Furthermore, it suggests that the vast majority of Ni is reincorporated during Fe(II)-activated recrystallization rather than released to solution. Stoichiometric dissolution experiments (Figure 4-12) and XPS analyses (Table 4-2) show that Ni does not accumulate at the surface for co-substituted goethite samples. Differences in Ni and Zn release from goethite and hematite were previously (Chapter 3) observed and attributed to differences in either mineral recrystallization or in the element repartitioning behavior. The iron atom exchange data suggests that trace element release is proportional to but not indicative of the amount of recrystallization. These previously observed differences in Ni and Zn release may thus reflect the favorability of reincorporation, which is likely controlled by the ionic radii of Ni^{2+} and Zn^{2+} relative to that of Fe^{3+}.

Inhibition Mechanism

Trace element release from iron oxides during reaction with aqueous Fe(II) is substantially inhibited when insoluble co-substituents are present in the crystal structure. Substitution of Al into goethite hinders iron atom exchange and lessens the amount of Ni release to solution, suggesting that Ni and Zn release inhibition is related to the amount of Fe(II)-activated recrystallization of iron oxide minerals. While decreased iron atom exchange reduces the amount of trace element release, the mechanism by which Al, Cr, and Sn hinder such atom exchange is unclear.

Al, Cr, and Sn substitution enhance the conductivity of iron oxides (Morin, 1951; Balko and Clarkson, 2001; Kerisit and Rosso, 2007; Kleiman-Shwarsctein et al., 2008; Huda et al., 2010; Kleiman-Shwarsctein et al., 2010; Ling et al., 2011). This is expected to increase the rate of Fe(II)-Fe(III) ETAE and thus recrystallization. Trace element release and, in the Al case, atom exchange are inhibited, so conductivity changes cannot be responsible. Alternatively, these insoluble elements may build up on the mineral surface thus resulting in passivation. A common property of Al, Cr, and Sn is insolubility at circumneutral pH. Since Fe(II)-Fe(III) ETAE involves both Fe(II) oxidative adsorption and Fe(III) reductive dissolution, the surface concentration of these substituted elements should increase where Fe(III) reductive dissolution occurs. Dissolution should thus slow, at lease locally, upon build-up of an insoluble redox-inactive element because of physical blocking of Fe sites or redirection of electron flow.

Substantial changes in mineral surface concentration are not readily apparent. For example, there is no TEM evidence for co-substituent exsolution (Figures 4-8,4-9). Modest surface compositional changes are observed by XPS (Figure 4-10), but there

appears to be no major accumulation or depletion of Al, Cr, or Sn (Table 4-2). The lack of net accumulation of insoluble co-substituents based on bulk surface composition measurements is not inconsistent with the hypothesis that these elements buildup at surfaces and inhibit Fe(II)-Fe(III) ETAE. For instance, net accumulation on a surface experiencing Fe(III) reductive dissolution may be balanced by the buildup of Fe via Fe(II) oxidative adsorption on a different surface of the same particle. Such compositional changes would be unapparent from measurements by XPS which determines the average surface composition.

Environmental Implications

Naturally occurring iron oxide minerals commonly contain impurities and, consequently, their reactivity should be different from pure phases typically used in laboratory studies. Since Al, Cr, and Sn substitution enhances the conductivity of iron oxides (Morin, 1951; Balko and Clarkson, 2001; Kerisit and Rosso, 2007; Kleiman-Shwarsctein et al., 2008; Huda et al., 2010; Kleiman-Shwarsctein et al., 2010; Ling et al., 2011), the reduction of contaminants mediated by Fe(II) may be enhanced in natural settings. This investigation, however, shows that Al, Cr, and Sn substitution inhibits the release of associated trace elements during reaction with aqueous Fe(II), thus rendering them less effective as sources for micronutrients in soils and sediments. Entrapment of contaminants in iron oxides, however, is a more stable sequestration method if the mineral phase also contains insoluble co-dopants.

ACKNOWLEDGEMENTS

This work was supported by the National Science Foundation (NSF) through Grant No. EAR-0818354. ICP-OES analyses were performed at the Nano Research Facility at Washington University in St. Louis, which is supported by the NSF under award ECS-0335765. XPS measurements were performed at EMSL, a national scientific user facility sponsored by the Department of Energy's Office of Biological and Environmental Research and located at Pacific Northwest National Laboratory. EXAFS measurements were performed at the DuPont-Northwestern-Dow Collaborative Access Team (DND-CAT) located at Sector 5 of the Advanced Photon Source (APS). DND-CAT is supported by E.I. DuPont de Nemours & Co., The Dow Chemical Company and Northwestern University. Use of the APS, an Office of Science User Facility operated for the U.S. Department of Energy (DOE) Office of Science by Argonne National Laboratory, was supported by the U.S. DOE under Contract No. DE-AC02-06CH11357.

Table 4-1. Physical properties of iron oxides and kinetic parameters from eq 1 for Ni and Zn release from these materials upon reaction with 10^{-3} M Fe(II) at pH 7.

Sample ID	Substituent composition (mol%)		Surface Area ($m^2\ g^{-1}$)	$[Me]_{eq}$ (μM)	k_{obs} ($\mu M^{-1}\ d^{-1}$)	k^a (d^{-1})
	Me	Co-substituent				
NiGoe	1.37 Ni	-[b]	39.0	13.8(8)	0.027(6)	0.39(3)
NiAlGoe-1	1.05 Ni	1.03 Al	19.5	10.6(8)	0.027(7)	0.29(8)
NiAlGoe-2	1.05 Ni	2.05 Al	-	9(1)	0.04(2)	0.4(2)
NiAlGoe-4	0.94 Ni	3.47 Al	-	7.4(7)	0.04(1)	0.30(8)
NiAlGoe-8	0.67 Ni	7.31 Al	10.8	6.1(5)	0.06(2)	0.4(1)
AlGoe	-	1.83 Al	-	-	-	-
NiCrGoe-1	1.98 Ni	0.90 Cr	43.9	11(2)	0.013(8)	0.14(9)
NiCrGoe-2	2.09 Ni	2.45 Cr	-	10(2)	0.012(7)	0.12(7)
NiCrGoe-4	2.00 Ni	3.97 Cr	-	6(1)	0.02(1)	0.12(6)
NiCrGoe-8	1.81 Ni	5.87 Cr	49.2	4.6(8)	0.03(2)	0.14(9)
NiSnGoe-1	1.69 Ni	0.77 Sn	39.2	11.5(9)	0.017(4)	0.20(5)
NiSnGoe-2	1.86 Ni	1.42 Sn	-	9.8(8)	0.021(6)	0.21(6)
NiSnGoe-4	2.01 Ni	2.37 Sn	-	9(1)	0.04(2)	0.4(2)
NiSnGoe-8	2.69 Ni	4.48 Sn	37.2	7.5(5)	0.05(1)	0.38(8)
ZnHem	1.70 Zn	-	13.1	12(1)	0.05(2)	0.77(7)
ZnAlHem-1	1.38 Zn	1.15 Al	15.5	9(1)	0.07(4)	0.6(4)
ZnAlHem-2	1.39 Zn	2.18 Al	-	6.5(8)	0.10(6)	0.7(4)
ZnAlHem-4	1.48 Zn	4.33 Al	-	3.9(5)	0.3(2)	1.2(8)
ZnAlHem-8	1.30 Zn	8.53 Al	16.8	3.0(4)	0.4(3)	1.2(9)
AlHem	-	2.15 Al	-	-	-	
ZnCrHem-1	1.33 Zn	0.35 Cr	19.6	4.0(4)	0.3(2)	1.2(8)
ZnCrHem-2	1.13 Zn	0.49 Cr	-	3.0(3)	0.4(3)	1.2(9)
ZnCrHem-4	0.88 Zn	0.82 Cr	-	1.9(3)	0.7(6)	1(1)
ZnCrHem-8	0.77 Zn	1.18 Cr	24.6	1.0(1)	10(10)[c]	10(10)
ZnSnHem-1	1.67 Zn	1.01 Sn	40.6	8.4(9)	0.14(8)	1.2(7)
ZnSnHem-2	1.84 Zn	1.94 Sn	-	4.9(5)	0.3(2)	1.5(9)
ZnSnHem-4	2.01 Zn	4.20 Sn	-	2.1(3)	0.2(1)	0.4(2)
ZnSnHem-8	1.75 Zn	7.90 Sn	46.2	1.2(1)	1.1(5)	1.3(6)

[a] Master rate constant (i.e., $k = [Me]_{eq} \times k_{obs}$). See Chapter 3.
[b] Dash (-) indicates no measurement or not applicable.
[c] The large k_{obs} results from the absence of data points at early times.

Table 4-2. XPS quantification of surface composition of goethite and hematite containing the greatest quantities of each co-substituent after reaction in a pH 7 fluid with or without 10^{-3} M Fe(II). Singly-substituted Al-substituted goethite and hematite are also shown.

Sample ID	[Fe(II)] (M)	Surface composition (atom%)[a]				Me (mol%)	Co-substituent (mol%)
		O	Fe[b]	Me	Co-substituent		
NiAlGoe-8	0	63.7	32.3	1.3 Ni	2.7 Al	3.52	7.49
NiAlGoe-8	10^{-3}	64.2	32.2	1.2 Ni	2.4 Al	3.47	6.69
NiCrGoe-8	0	63.0	31.3	1.3 Ni	4.3 Cr	3.62	11.73
NiCrGoe-8	10^{-3}	63.0	31.5	1.3 Ni	4.3 Cr	3.44	11.56
NiSnGoe-8	0	64.9	29.8	2.3 Ni	3.0 Sn	6.51	8.58
NiSnGoe-8	10^{-3}	64.0	31.2	1.8 Ni	3.0 Sn	4.91	8.33
ZnAlHem-8	0	55.9	42.4	0.3 Zn	1.4 Al	0.75	3.10
ZnAlHem-8	10^{-3}	56.6	41.5	0.2 Zn	1.7 Al	0.42	3.83
ZnCrHem-8	0	56.2	41.6	0.1 Zn	2.1 Cr	0.21	4.85
ZnCrHem-8	10^{-3}	55.7	42.1	0.1 Zn	2.1 Cr	0.20	4.77
ZnSnHem-8	0	56.6	38.1	0.4 Zn	4.9 Sn	0.95	11.31
ZnSnHem-8	10^{-3}	57.6	37.3	0.3 Zn	4.9 Sn	0.67	11.49
AlGoe	0	61.8	37.5	-[c]	0.8 Al	-	1.96
AlGoe	10^{-3}	61.1	38.2	-	0.6 Al	-	1.65
AlHem	0	55.8	44.0	-	0.2 Al	-	0.55
AlHem	10^{-3}	54.8	44.7	-	0.5 Al	-	1.01

[a] All values reported after carbon over-layer correction.
[b] Fe values for samples containing Sn account for Sn 3p contribution in Fe 2p spectrum.
[c] Dash (-) indicates value is not applicable.

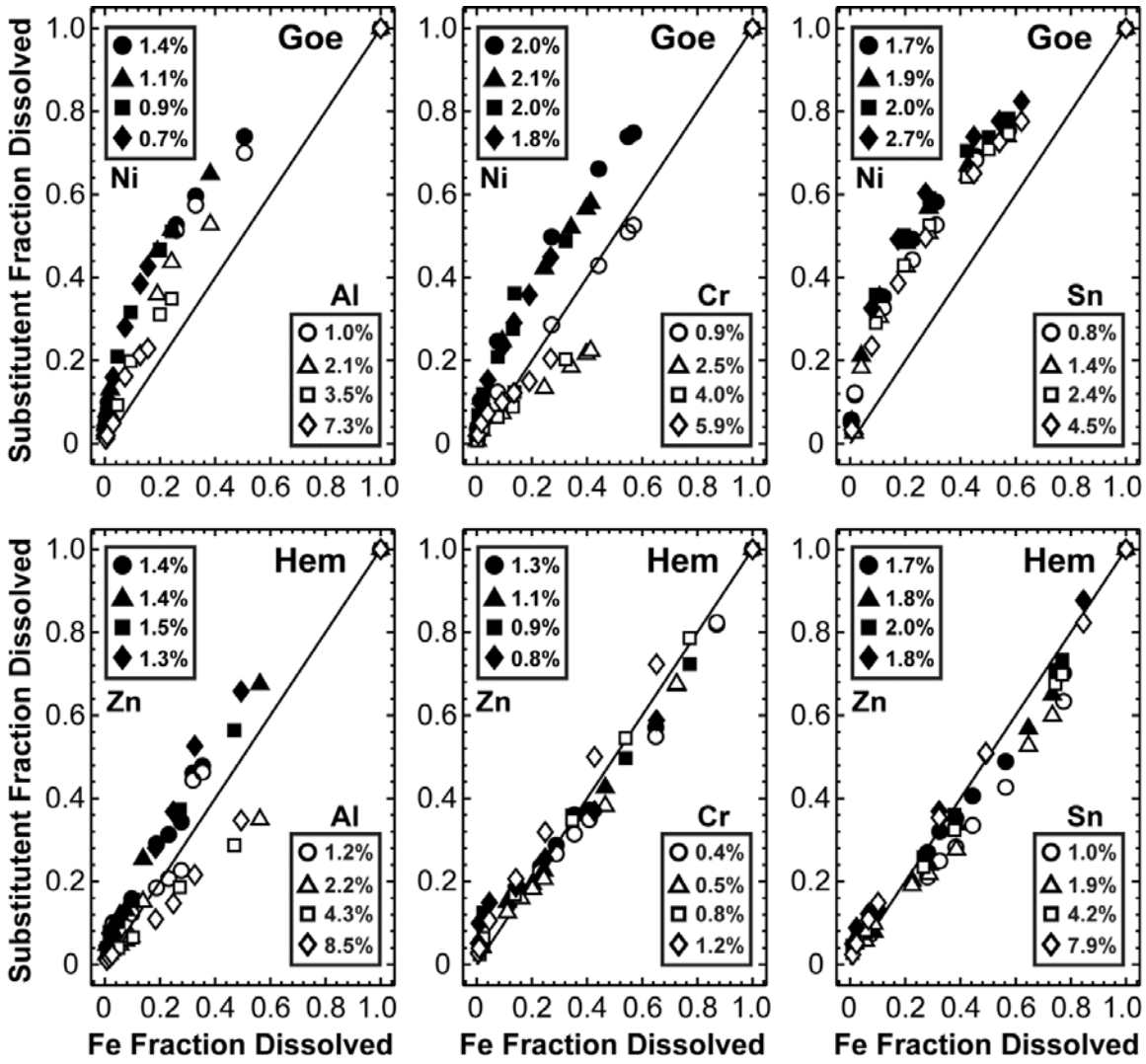

Figure 4-1. Fraction of Ni and Al, Cr, or Sn dissolved during complete acid dissolution of co-substituted goethite (top) and fraction of Zn and Al, Cr, or Sn dissolved during complete acid dissolution of co-substituted hematite (bottom). Solid line represents 1:1 dissolution.

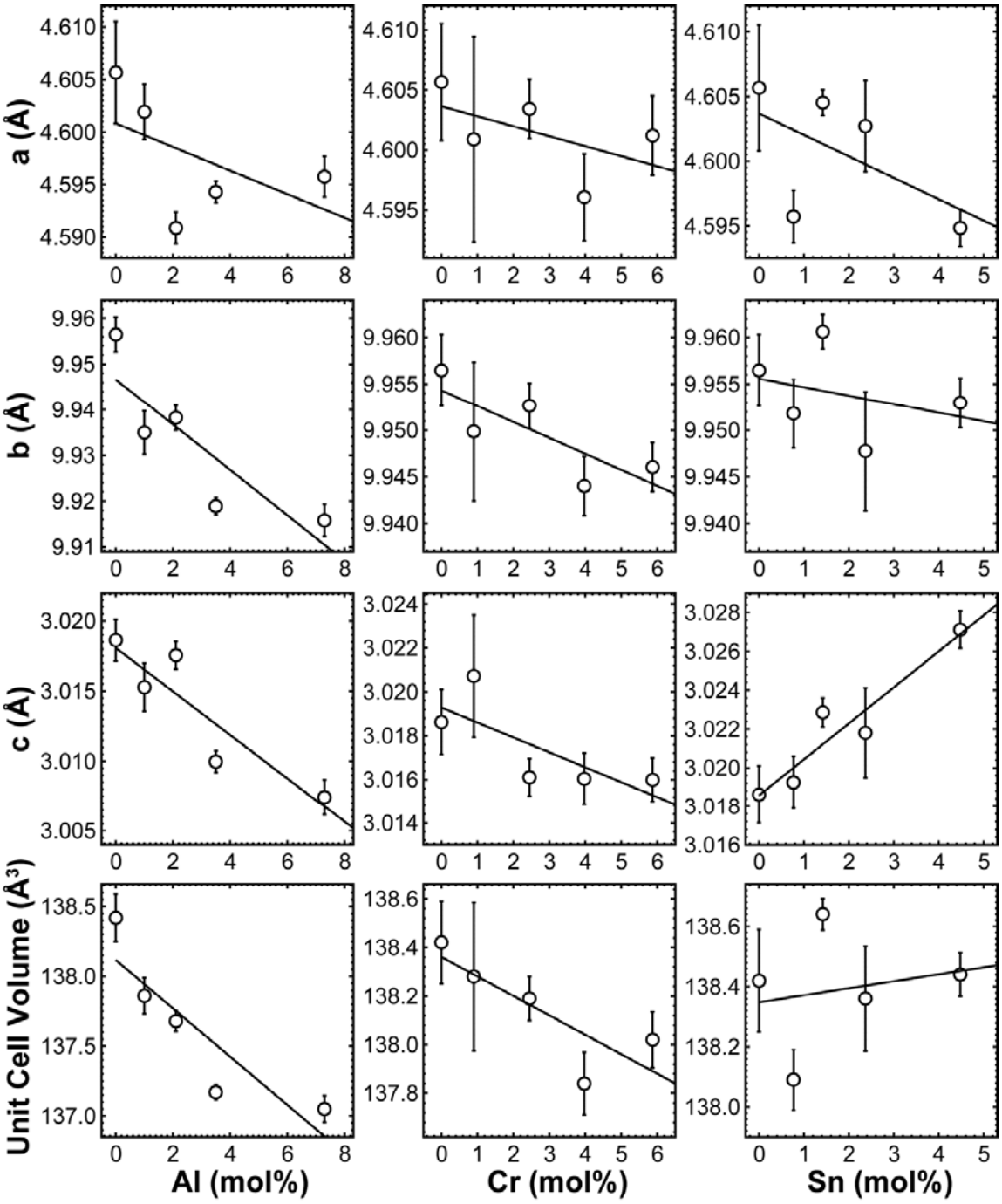

Figure 4-2. Unit cell parameters and calculated unit cell volume for co-substituted goethite. Solid line represents linear fit. Statistical uncertainties for each value are presented as error bars and reported at the 95% confidence level.

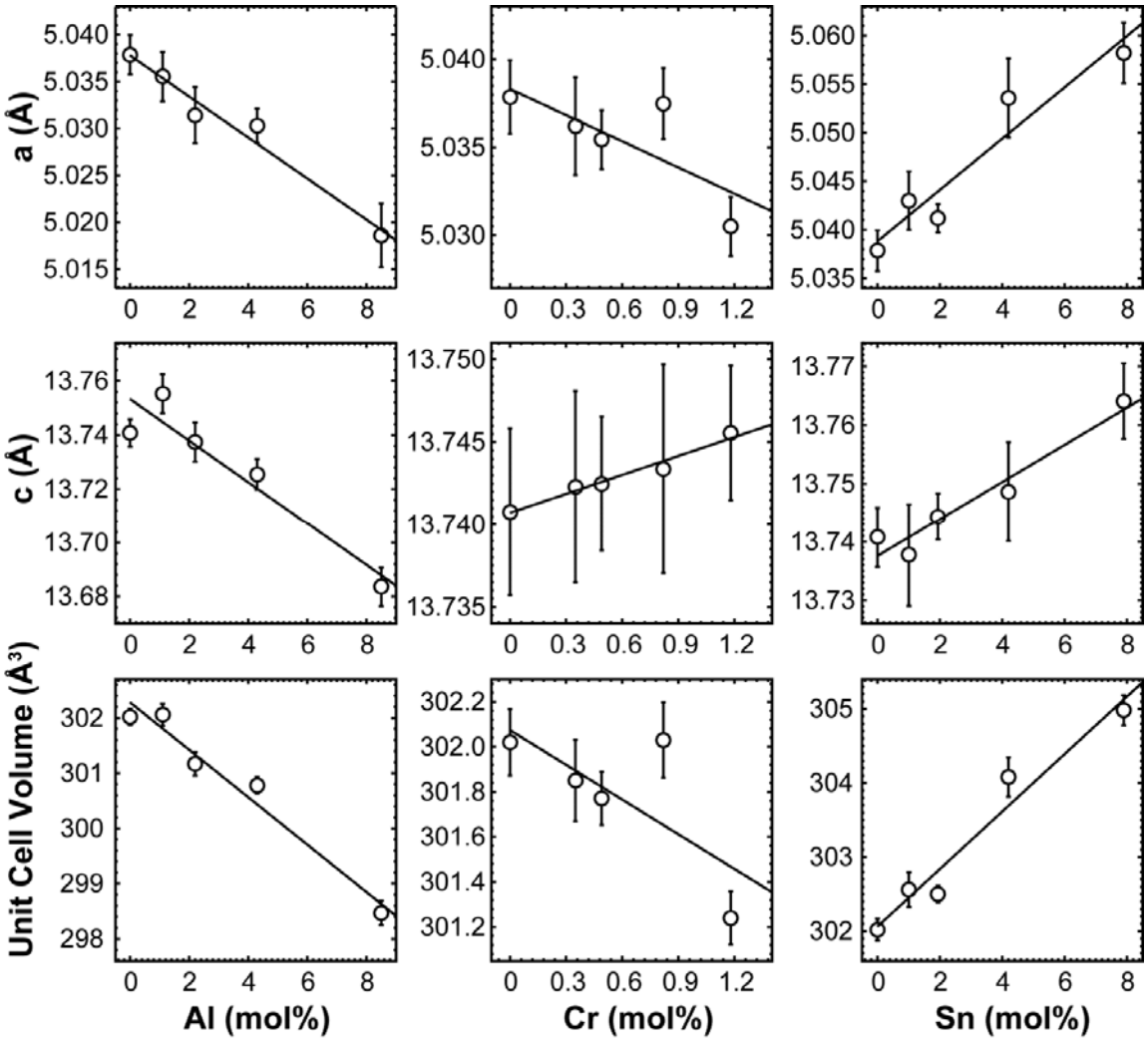

Figure 4-3. Unit cell parameters and calculated unit cell volume for co-substituted hematite. Solid line represents linear fit. Statistical uncertainties for each value are presented as error bars and reported at the 95% confidence level.

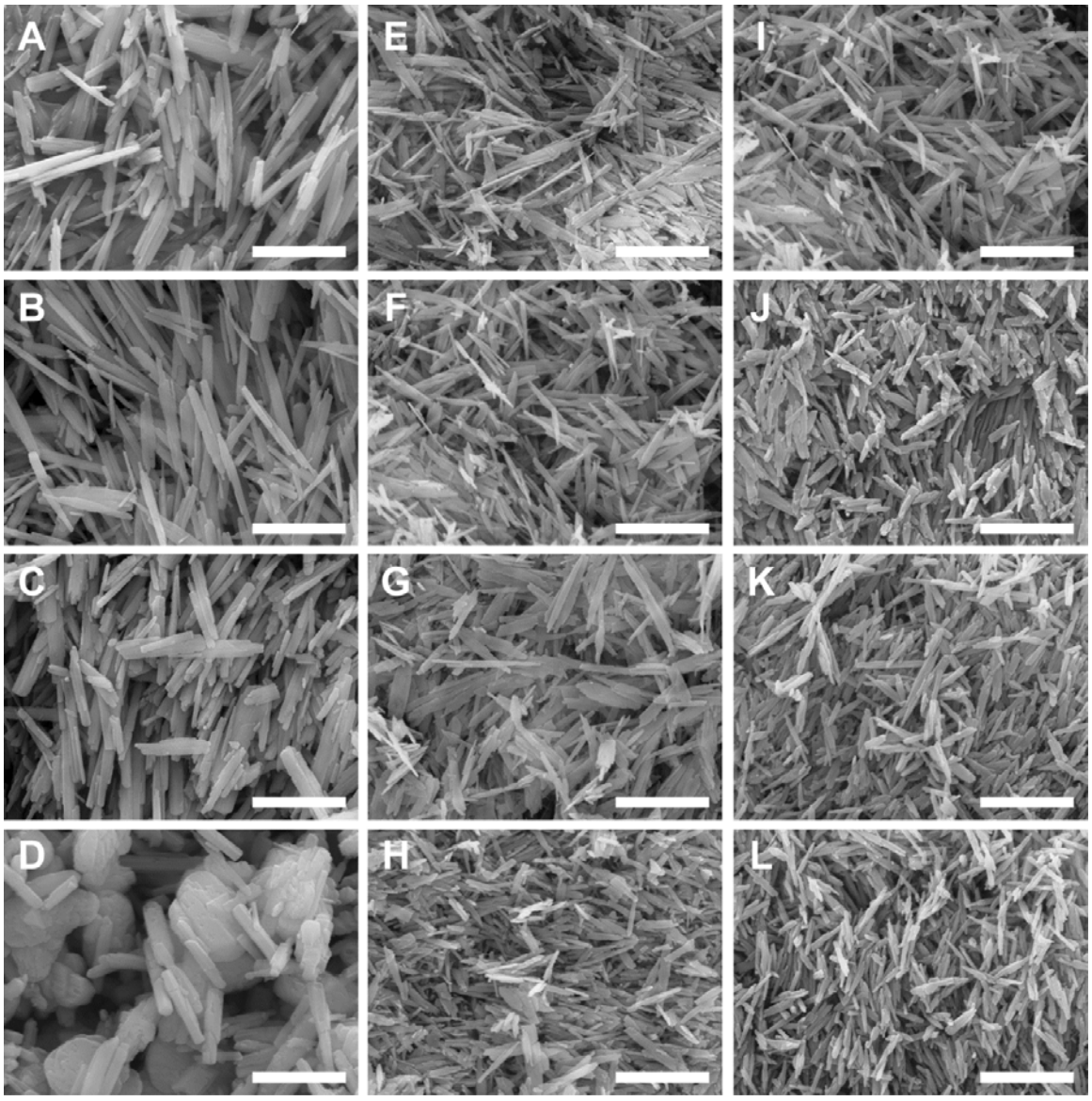

Figure 4-4. SEM images of Ni-substituted goethite with increasing levels of co-substituted Al (A-D), Cr (E-H), or Sn (I-L).

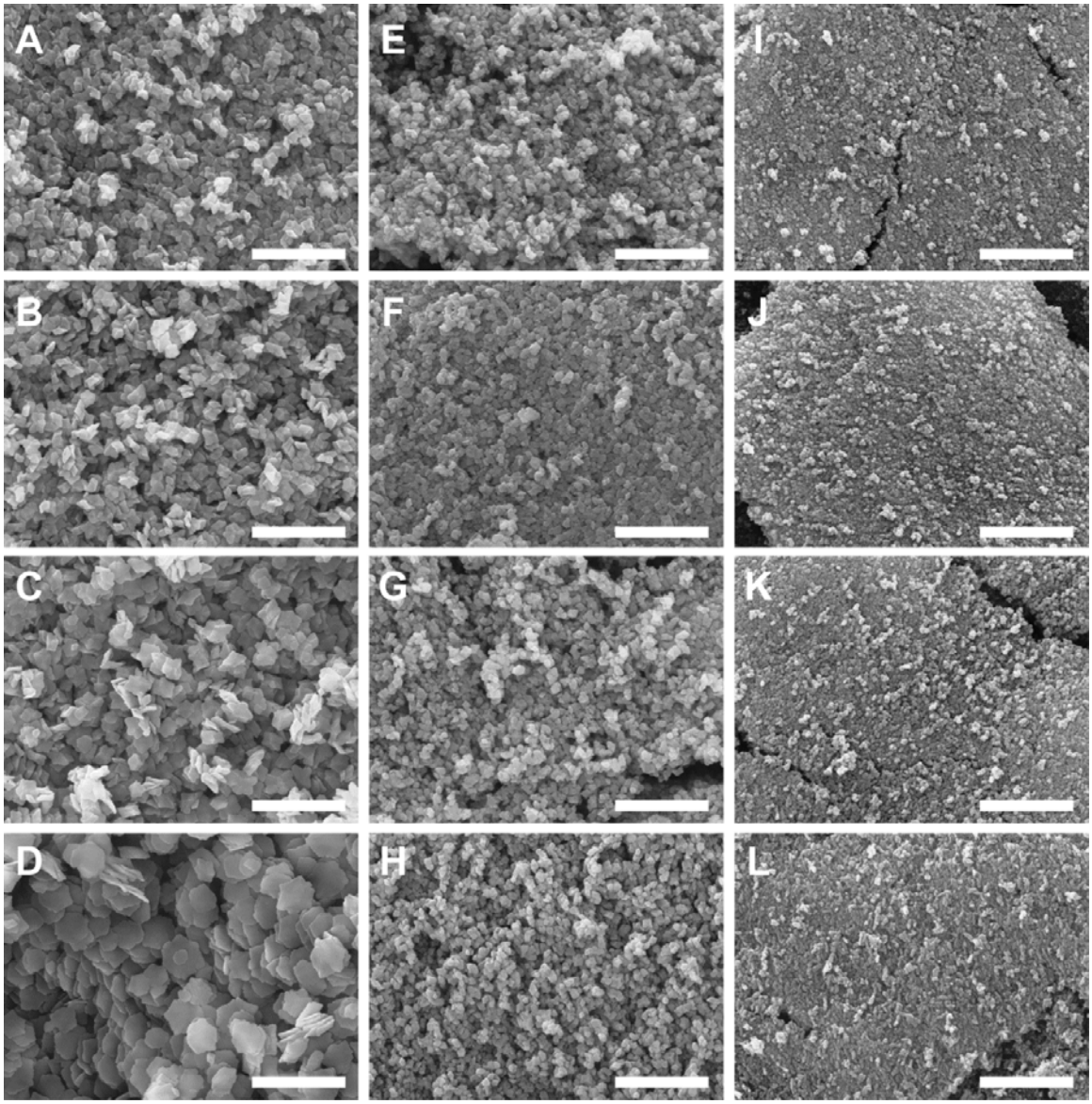

Figure 4-5. SEM images of Zn-substituted hematite with increasing levels of co-substituted Al (A-D), Cr (E-H), or Sn (I-L).

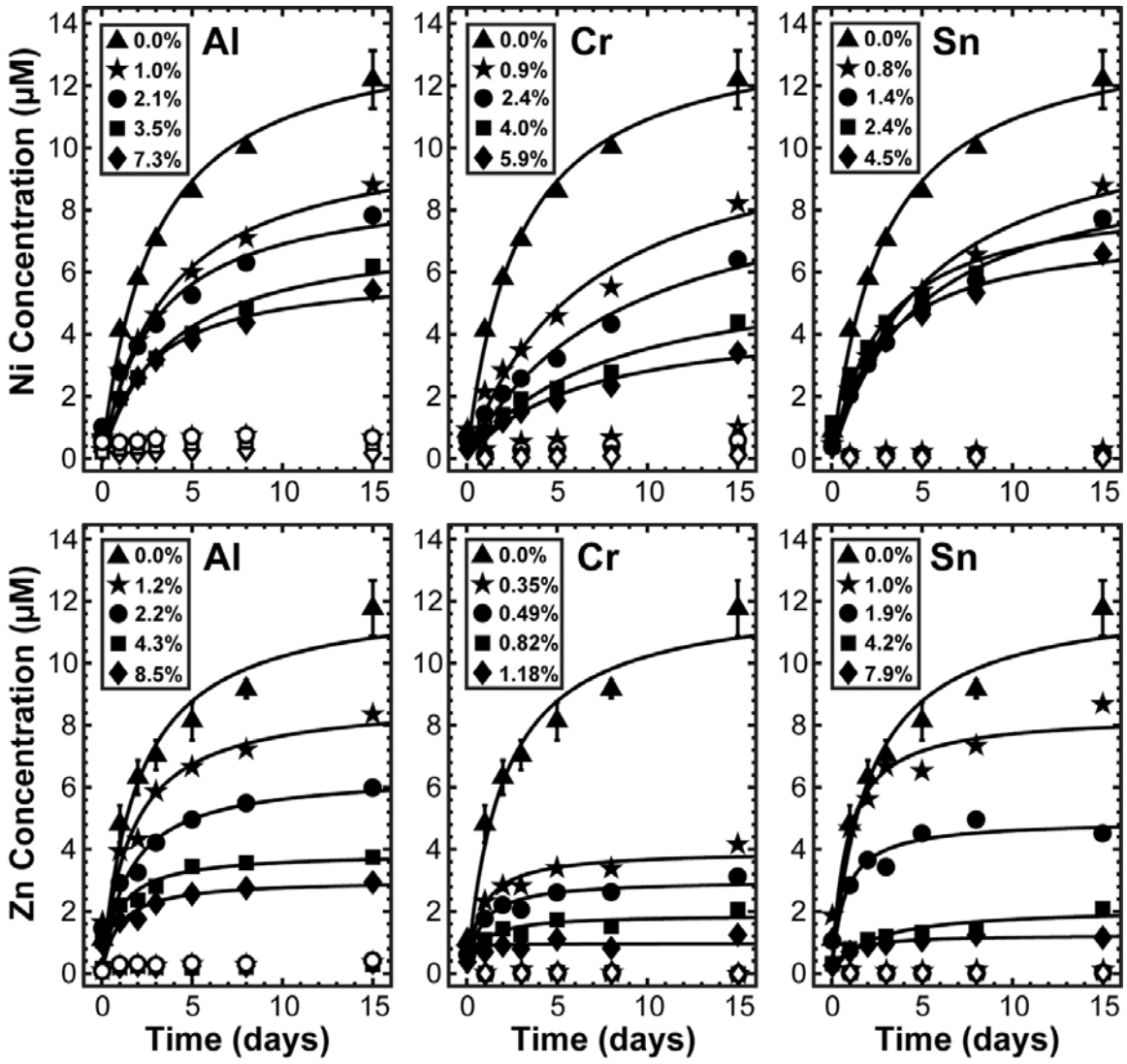

Figure 4-6. Aqueous Ni and Zn concentrations during reaction of 10^{-3} M Fe(II) at pH 7 with Ni-substituted goethite (top row) and Zn-substituted hematite (bottom row) co-substituted with Al, Cr, or Sn. Open symbols represent Fe(II)-free controls. Solid lines are second-order kinetic fits using eq 1. Data for NiGoe and ZnHem, obtained previously (Chapter 3), are shown for comparison.

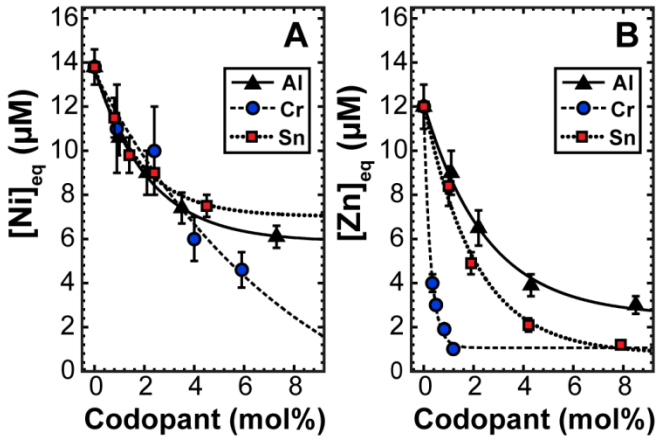

Figure 4-7. Equilibrium Ni and Zn concentrations following reaction of Al, Cr, and Sn co-substituted (A) Ni-substituted goethite and (B) Zn-substituted hematite with 10^{-3} M Fe(II) at pH 7. Values were obtained by fitting each time-series in Figure 1 using a second-order kinetic model (eq 1). Statistical uncertainties for each value are presented as error bars and reported at the 95% confidence level. Solid lines represent fits using an exponential equation.

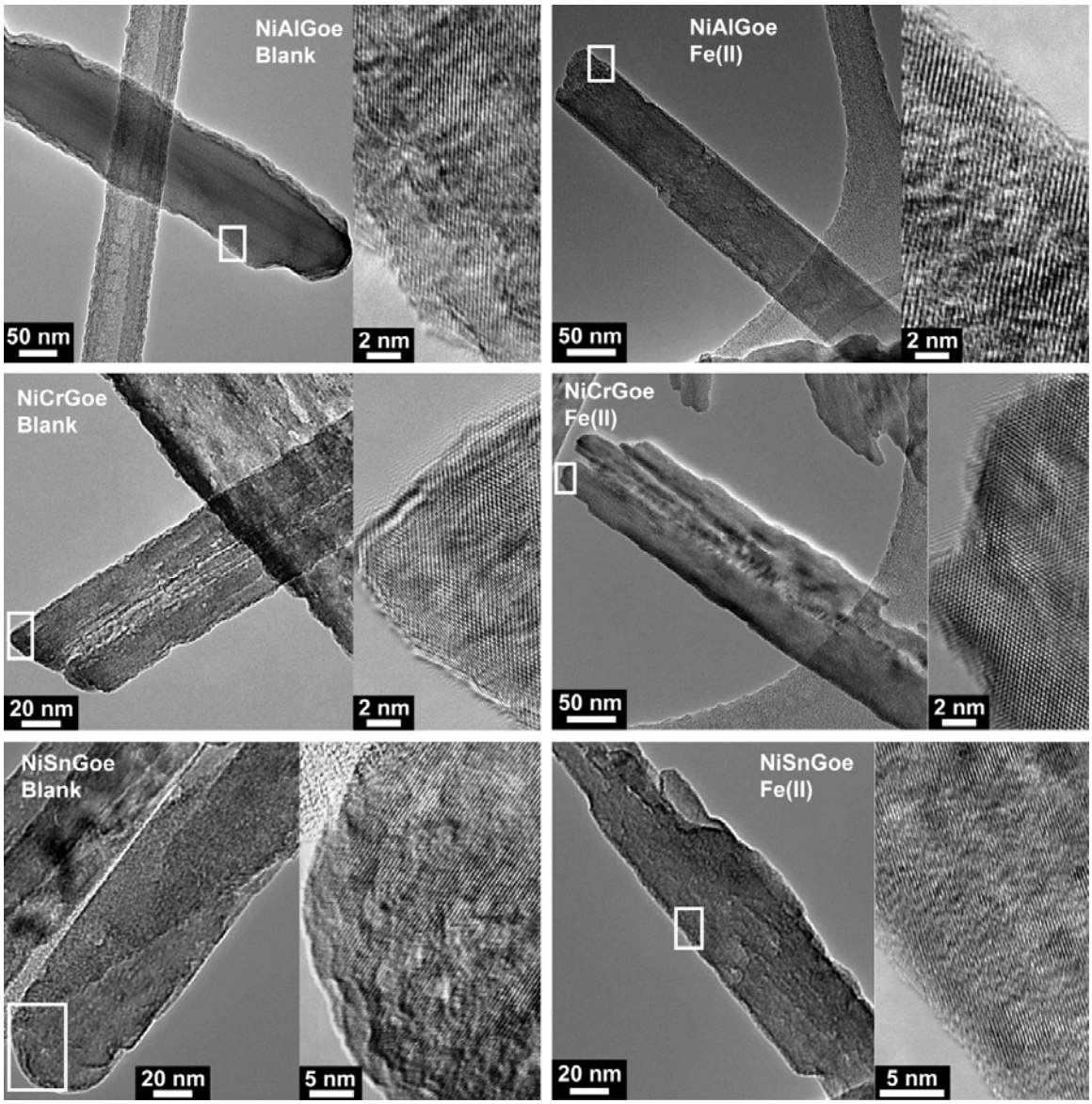

Figure 4-8. TEM images of Ni-substituted goethite co-substituted with the highest levels of Al, Cr, or Sn after reaction in a pH 7 fluid with (right) or without (left) 10^{-3} M Fe(II). White box indicates the imaging area for high resolution TEM.

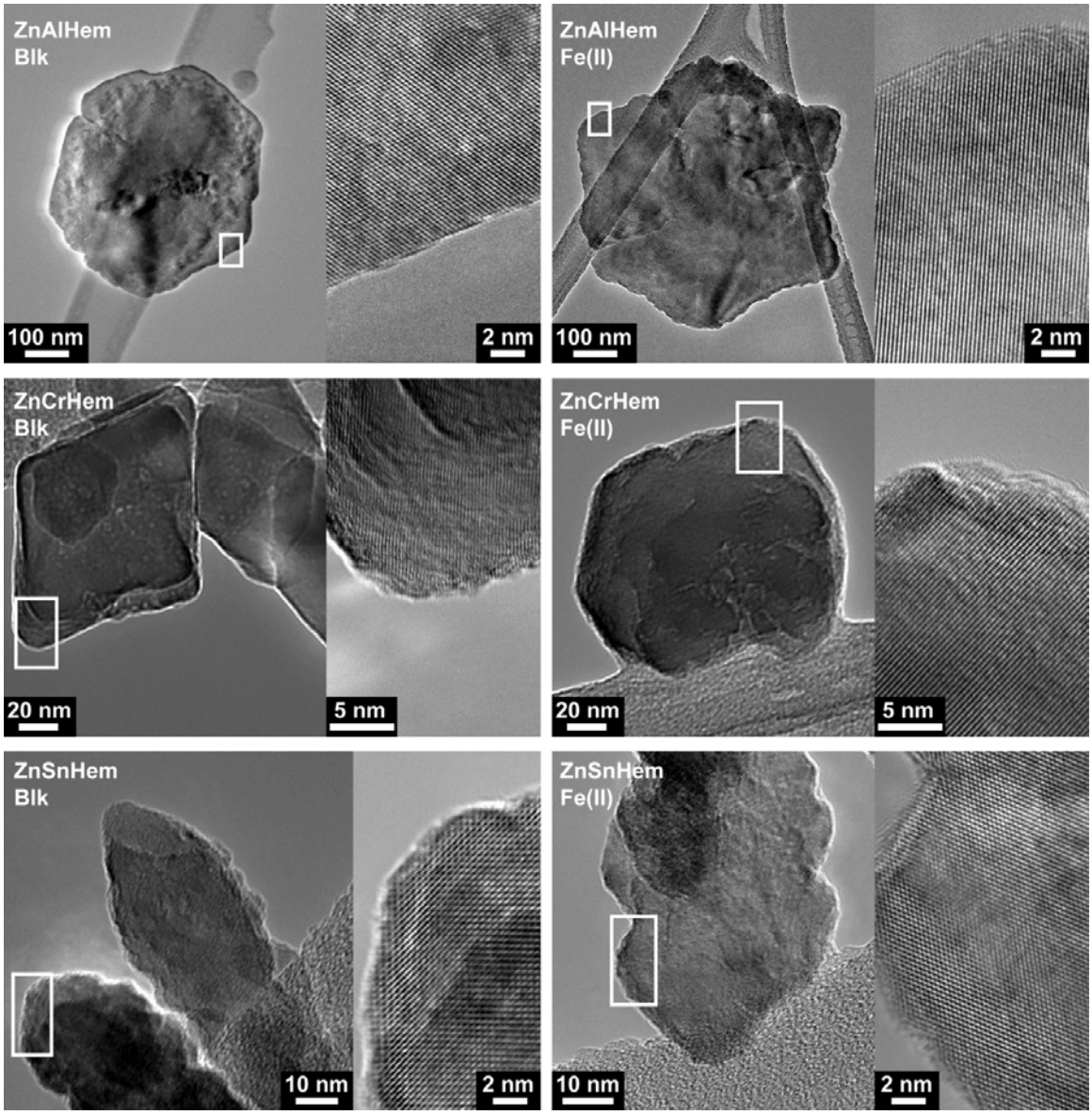

Figure 4-9. TEM images of Zn-substituted hematite co-substituted with the highest levels of Al, Cr, or Sn after reaction in a pH 7 fluid with (right) or without (left) 10^{-3} M Fe(II). White box indicates the imaging area for high resolution TEM.

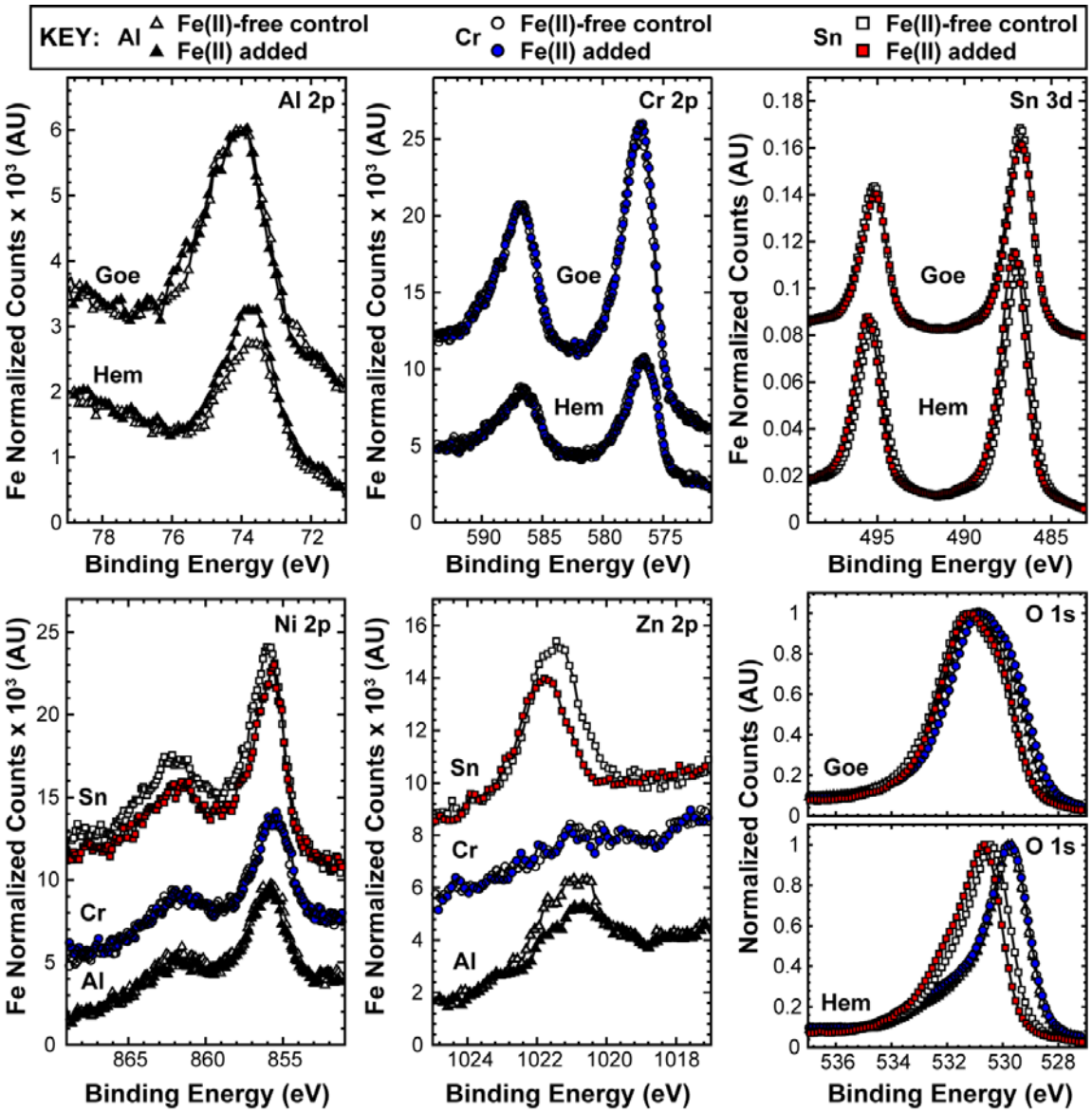

Figure 4-10. XPS spectra of Ni-substituted goethite and Zn-substituted hematite co-substituted with the highest levels of Al, Cr, or Sn after reaction in a pH 7 fluid with or without 10^{-3} M Fe(II). Each spectrum, except O 1s, is normalized by the peak area of the Fe 2p region for that sample and accounts for the Sn 3d contribution if applicable. All spectra are energy corrected by setting the C 1s peak equal to 285.0 eV.

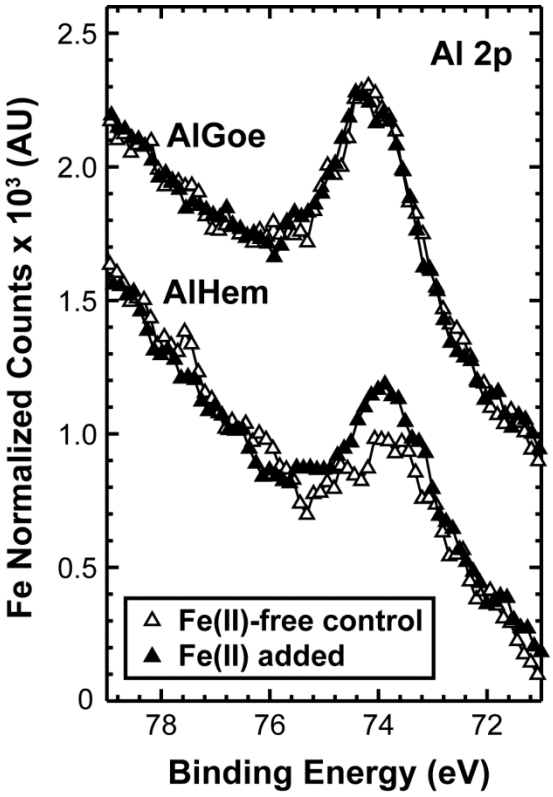

Figure 4-11. XPS spectra of Al-substituted goethite and Al-substituted hematite after reaction in a pH 7 fluid with or without 10^{-3} M Fe(II). Each spectrum is normalized by the peak area of the Fe 2p region for that sample. All spectra are energy corrected by setting the C 1s peak equal to 285.0 eV.

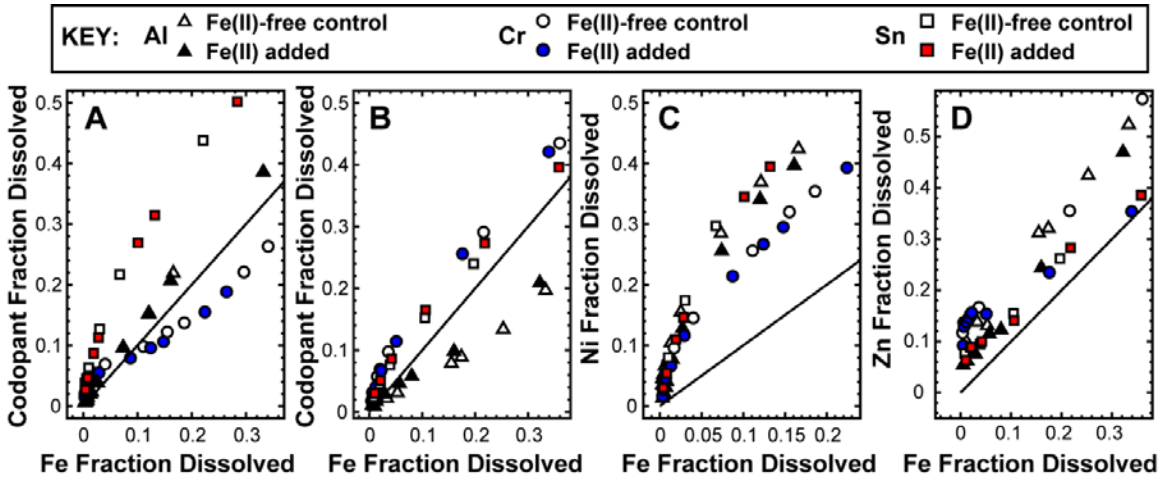

Figure 4-12. Fraction of Al, Cr, or Sn dissolved during complete acid dissolution of co-substituted goethite (A) and (B) hematite. Fraction of (C) Ni and (D) Zn dissolved during complete acid dissolution of co-substituted goethite and hematite, respectively. Solid line represents 1:1 dissolution.

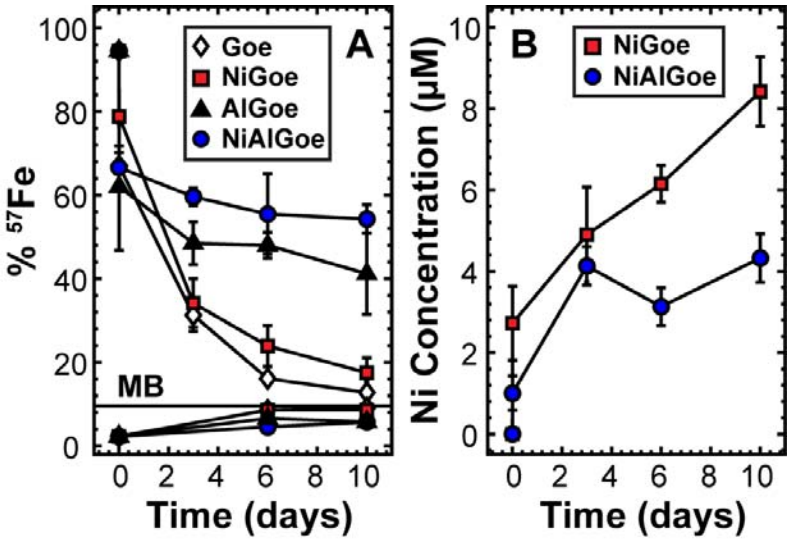

Figure 4-13. (A) Iron isotope exchange between aqueous Fe(II) and goethite, Ni-substituted goethite, Al-substituted goethite, and Ni,Al-co-substituted goethite. Horizontal solid line represents the calculated mass balance (MB) upon complete isotopic equilibration of ^{57}Fe(II) with 1 g L^{-1} of natural isotopically abundant goethite. Points below MB line are for solid Fe whereas points above MB line are for aqueous Fe(II). Points represent the mean value of triplicate samples and error bars correspond to the standard deviation. Solid curves are second-order kinetic fits. Reaction conditions: 1 g L^{-1} solid, 10^{-3} M initial Fe(II), and 10^{-3} M MOPS at pH 7.

CHAPTER 4 APPENDIX

SECTION A1. EXAFS DATA COLLECTION AND ANALYSIS

EXAFS measurements were performed on beamline 5-BM-D at the Advanced Photon Source at Argonne National Laboratory in fluorescent yield mode. The incident beam energy was selected using a Si(111) double-crystal monochromator. The harmonic content of the X-ray beam was reduced by detuning the second crystal of the monochromator by 40% and by insertion of a pair of Rh-coated harmonic mirrors. Samples were mounted as dry powders and sealed in polycarbonate holders with Kapton^{TM} tape. The X-ray energy was calibrated by setting the maximum in the first derivative of the X-ray absorption near-edge structure spectrum of a Zn or Ni metal foil to 9659 eV or 8333 eV for the Zn and Ni K-edges, respectively. The normalized and background subtracted k^3-weighted EXAFS spectra of Ni and Zn were quantitatively analyzed in SixPACK using phase and amplitude functions. These functions were generated from a Ni or Zn atom substituted in an Fe(III)-octahedral site in the structures of goethite [α-FeOOH] (Gualtieri and Venturelli, 1999) and hematite [α-Fe_2O_3] (Blake et al., 1966), respectively, using FEFF 7.02 (Ankudinov et al., 1998). Fitting of the spectra of samples that also contained Al or Sn employed phase and amplitude functions generated from structure that included both substituting atoms (e.g., Ni and Al). Coordination number (N), interatomic distance (R), and σ^2 (a Debye–Waller-type factor based on a Gaussian distribution of interatomic distances), were refined using a nonlinear least-squares fitting routine. The amplitude reduction factor, S_0^2, was fixed to 0.9 for spectral fitting.

Ni and Zn K-edge EXAFS spectra for Ni-substituted goethite and Zn-substituted hematite, respectively, containing the highest quantities of co-substituted Al, Cr, or Sn are consistent with Ni and Zn substituted within the crystal structure of these minerals, similar to singly-substituted NiGoe and ZnHem (Chapters 2 and 3). The amplitude of the second shell(s) for materials containing Al and Sn, however, is substantially reduced relative to singly-substituted or Cr-substituted iron oxides. This suggests that Al and Sn may be clustered near Ni and Zn in neighboring Fe sites. Destructive interferences between the scattering from Al or Sn and Fe neighbors in the same second shell position would reduce the size of the features in the Fourier transform between 2 and 3 $Å^{-1}$. Such interference would only have a significant effect on the spectra if Al and Sn concentrated in sites neighboring Ni and Zn far in excess of their bulk concentration. This was tested by fitting the spectra with an Al or Sn located in the nearest Fe site with its distance set equal to that of the Fe atoms. The sum of the Al or Sn plus Fe coordination number was set to 4 for hematite, the expected coordination for the first cation shell in this mineral. A similar process was repeated for goethite except a Sn or Al was added to both of the two nearest cation shells. All spectra are modeled well using this approach (Figure A4-1) and fitting parameters indicate that Al or Sn occupy 1 in 4 sites in the first cation shell for ZnAlHem, ZnSnHem, and NiSnGoe (Table S1). Greater Al clustering around Ni is observed in goethite with Al occupying nearly half of the cation sites surrounding Ni (Table A4-1). The substitution of Cr has little effect on the Ni and Zn EXAFS spectral features (Figure A4-1). While clustering of Cr around Ni and Zn may also occur, as seen with Al and Sn, EXAFS cannot identify such clustering because it is unable to distinguish Cr from Fe given their similar atomic numbers and electron scattering properties.

The Fourier transform (FT) of the Zn EXAFS for ZnSnHem exhibits a Zn-O shell with a larger amplitude and shift to larger distance relative to ZnHem, ZnAlHem-8, and ZnCrHem-8, suggesting a change in coordination (Figure A4-1). Fitting parameters for the O shell (Table A4-1) reveal a coordination number (6±1) and interatomic distance (2.06±0.02) consistent with octahedral Zn (Waychunas et al., 2002). This differs from the tetrahedral coordination of Zn in ZnHem (Chapter 3), ZnAlHem-8, and ZnCrHem-8 (Table A4-1). Octahedral Zn has a larger ionic radius than tetrahedral Zn and thus its substitution may only be favored upon a local expansion caused by the substitution of Sn(IV), which is larger than Fe(III) (Shannon, 1976).

Table A4-1. EXAFS spectra structural fitting results for Ni- and Zn-substituted iron oxides co-substituted with Al, Cr, or Sn.

		EXAFS					Structure[a]	
Sample	**Shell**	***N*[b]**	***R* (Å)**	**σ^2 (Å^2)**	**ΔE_0 (eV)**	**χ_ν^2**	***N***	***R* (Å)**
ZnAlHem	O	4(1)[c]	1.98(2)	0.008(3)	-5(3)	17.8	3, 3	1.946, 2.116
	Fe[d]	3.2(4)	2.92(2)	0.009[e]	-5(3)		4	2.953
	Al	0.8(4)	2.92(2)	0.009	-5(3)			2.953
	Fe	1.8(8)	3.32(3)	0.009	-5(3)		3	3.364
ZnCrHem	O	3(1)	1.99(2)	0.007(3)	-4(4)	11.8	3, 3	1.946, 2.116
	Fe[d]	4(2)	2.94(3)	0.008(4)	-4(4)		4	2.953
	Fe	3(1)	3.33(3)	0.008(4)	-4(4)		3	3.364
	Fe[f]	2(2)	3.70(4)	0.008(4)	-4(4)		6	3.705
ZnSnHem	O	6(1)	2.06(2)	0.013(3)	-1(2)	11.2	3, 3	1.946, 2.116
	Fe[d]	2.8(3)	3.00(1)	0.009[e]	-1(2)		4	2.953
	Sn	1.2(3)	3.00(1)	0.009	-1(2)			2.953
	Fe	1.4(5)	3.34(3)	0.009	-1(2)		3	3.364
NiAlGoe	O	6[g]	2.049(7)	0.0056(4)	-6(1)	0.88	3, 3	1.937, 2.088
	Fe	0.9(2)	3.04(5)	0.005[e]	-6(1)		2	3.013
	Al	1.1(2)	3.04(5)	0.005	-6(1)			3.013
	Fe	0.9(2)	3.18(5)	0.0044	-6(1)		2	3.292
	Al	1.1(2)	3.18(5)	0.0044	-6(1)			3.292
NiCrGoe	O	6[g]	2.06(1)	0.0053(7)	-3(2)	5.3	3, 3	1.937, 2.088
	Fe	2	2.97(2)	0.007(2)	-3(2)		2	3.013
	Fe	2	3.15(2)	0.005(2)	-3(2)		2	3.292
NiSnGoe	O	6[g]	2.049(7)	0.0056(4)	-4(1)	4.6	3, 3	1.937, 2.088
	Fe	1.4(2)	2.95(2)	0.005[e]	-4(1)		2	3.013
	Sn	0.6(2)	2.95(2)	0.005	-4(1)			3.013
	Fe	1.4(2)	3.12(2)	0.0044	-4(1)		2	3.292
	Sn	0.6(2)	3.12(2)	0.0044	-4(1)			3.292

[a] Coordination numbers and interatomic distances from iron site derived from the crystal structures of the minerals.

[b] Fixed to crystallographic values for NiCrGoe.

[c] Statistical uncertainties in the last digit are reported in parentheses at the 95% confidence level. Parameters with no listed uncertainties were not varied during the analysis.

[d] Represents multiple unresolvable neighbors.

[e] σ^2 fixed for all Fe shells based on values obtained from singly-substituted ZnHem or NiGoe (Chapters 2 and 3). These values were fixed to constrain the number of parameters during fitting.

[f] Inclusion of this Fe shells produced as better fit, as was the case ZnHem (Chapter 3).

[g] Two oxygen shells could not be resolved and a better fit was obtained with a single shell.

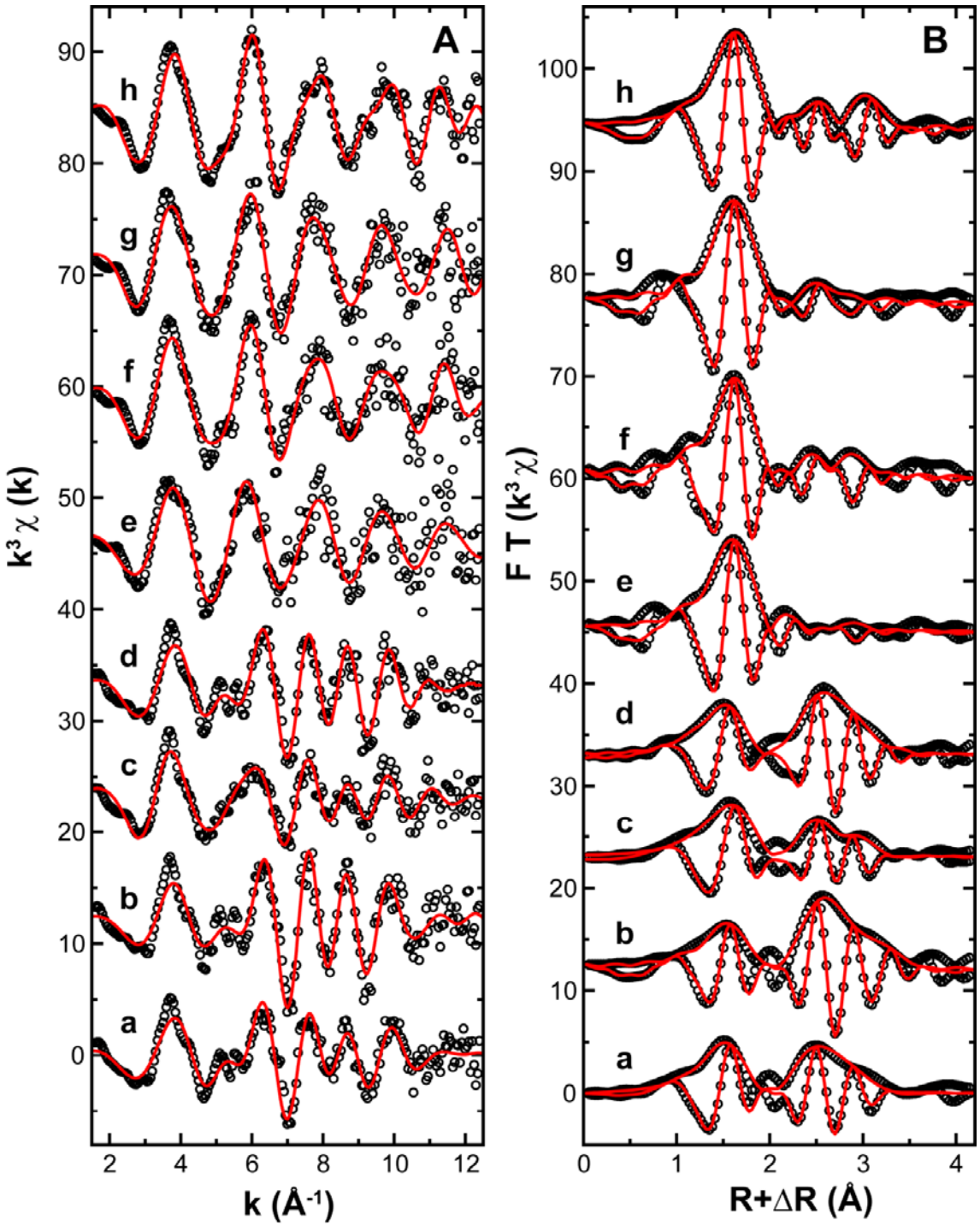

Figure A4-1. (A) Ni and Zn K-edge EXAFS spectra (points) and structural model fits (lines) as well as (B) fourier transform (FT) magnitudes and real components of EXAFS spectra for (a) ZnAlHem-8, (b) ZnCrHem-8, (c) ZnSnHem-8, (d) ZnHem, (e) NiAlGoe-8, (f) NiCrGoe-8, (g) NiSnGoe-8, and (h) NiGoe.

$$Rate = \frac{d[Me]}{dt} = k_{obs}([Me]_{eq} - [Me])^2$$

Equation A4-1. t is time (days), [Me] is metal concentration (μM) at time t, $[Me]_{eq}$ is the equilibrium Me concentration (μM), and k_{obs} is a pseudo second-order rate constant ($\mu M^{-1}\ d^{-1}$).

REFERENCES

Ankudinov A. L., Ravel B., Rehr J. J., and Conradson S. D. (1998) Real-space multiple-scattering calculation and interpretation of x-ray-absorption near-edge structure. *Phys. Rev. B* **58**, 7565–7576.

Balko B. A. and Clarkson K. M. (2001) The effect of doping with Ti(IV) and Sn(IV) on oxygen reduction at hematite electrodes. *J. Electrochem. Soc.* **148**, E85-E91.

Beard B. L., Handler R. M., Scherer M. M., Wu L., Czaja A. D., Heimann A., and Johnson C. M. (2010) Iron isotope fractionation between aqueous ferrous iron and goethite. *Earth Planet. Sc. Lett.* **295**, 241–250.

Berner R. A. (1978) Rate control of mineral dissolution under Earth surface conditions. *Am. J. Sci.* **278**, 1235-1252.

Blake R. L., Hessevick R. E., Zoltai T., and Finger L. W. (1966) Refinement of the hematite structure. *Am. Mineral.* **51**, 123-129.

Bousserrhine N., Gasser U. G., Jeanroy E., and Berthelin J. (1999) Bacterial and chemical reductive dissolution of Mn-, Co-, Cr-, and Al-substituted goethites. *Geomicrobiol. J.* **16**, 245-258.

Brown G. E., Jr., Henrich V. E., Casey W. H., Clark D. L., Eggleston C., Felmy A., Goodman D. W., Gratzel M., Maciel G., McCarthy M. I., Nealson K. H., Sverjensky D. A., Toney M. J., and Zachara J. M. (1999) Metal oxide surfaces and their interaction with aqueous solutions and microbial organisms. *Chem. Rev.* **99**, 77-174.

Buerge I. J. and Hug S., J. (1999) Influence of mineral surfaces on chromium(VI) reduction by iron(II). *Environ. Sci. Technol.* **33**, 4285–4291.

Charlet L., Silvester E., and Liger E. (1998) N-compound and actinide immobilisation in surficial fluids by Fe(II): The surface $Fe^{III}OFe^{II}OH^{o}$ species, as major reductant. *Chem. Geol.* **151**, 85–93.

Cooper C. D., Picardal F., Rivera J., and Talbot C. (2000) Zinc immobilization and magnetite formation via ferric oxide reduction by *Shewanella* putrefaciens 200. *Environ. Sci. Technol.* **34**, 100-106.

Cooper C. D., Neal A. L., Kukkadapu R. K., Brewe D., Coby A., and Picardal F. W. (2005) Effects of sediment iron mineral composition on microbially mediated changes in divalent metal speciation: Importance of ferrihydrite. *Geochim. Cosmochim. Acta* **69**, 1739–1754.

Cornell R. M. and Schwertmann U. (2003) *The iron oxides: Structure, properties, reactions, occurrences and uses*. Wiley-VCH Verlag GmbH & Co. KGaA.

Coughlin B. R. and Stone A. T. (1995) Nonreversible adsorption of divalent metal ions (Mn(II), Co(II), Ni(II), Cu(II), and Pb(II)) onto goethite: Effects of acidification, Fe(II) addition, and picolinic acid addition. *Environ. Sci. Technol.* **29**, 2445–2455.

Elsner M., Schwarzenbach R. P., and Haderlein S. (2004) Reactivity of Fe(II)-bearing minerals toward reductive transformation of organic contaminants. *Environ. Sci. Technol.* **38**, 799–807.

Felmy A. R., Moore D. A., Rosso K. M., Qafoku O., Rai D., Buck E. C., and Ilton E. S. (2011) Heterogeneous Reduction of PuO_2 with Fe(II): Importance of the Fe(III) Reaction Product. *Environ. Sci. Technol.* **45**, 3952–3958.

Fitzpatrick R. W. and Schwertmann U. (1982) Al-substituted goethite-An indicator of pedogenic and other weathering environments in South Africa. *Geoderma* **27**, 335-347.

Frierdich A. J., Luo Y., and Catalano J. G. (2011) Trace element cycling through iron oxide minerals during redox-driven dynamic recrystallization. *Geology* **39**, 1083–1086.

Frierdich A. J. and Catalano J. G. (2012) Controls on Fe(II)-activated trace element release from goethite and hematite. *Environ. Sci. Technol.* **46**, 1519−1526.

Gualtieri A. and Venturelli P. (1999) In situ study of the goethite-hematite phase transformation by real time, synchrotron powder diffraction. *Am. Mineral.* **84**, 895–904.

Haderlein S. and Pecher K. (1998) Pollutant reduction in heterogeneous Fe(II)-Fe(III) systems. In *Mineral-water interfacial reactions: Kinetics and mechanisms*, Vol. 715: ACS Symposium Series (ed. D. L. Sparks and T. J. Grundl), pp. 342-357. American Chemical Society.

Handler R. M., Beard B. L., Johnson C. M., and Scherer M. M. (2009) Atom exchange between aqueous Fe(II) and goethite: An Fe isotope tracer study. *Environ. Sci. Technol.* **43**, 1102–1107.

Hansel C. M., Learman D. R., Lentini C. J., and Ekstrom E. B. (2011) Effect of adsorbed and substituted Al on Fe(II)-induced mineralization pathways of ferrihydrite. *Geochim. Cosmochim. Acta* **75**, 4653–4666.

Hofstetter T. B., Schwarzenbach R. P., and Haderlein S. B. (2003) Reactivity of Fe(II) species associated with clay minerals. *Environ. Sci. Technol.* **37**, 519-528.

Huda M. N., Walsh A., Yan Y., Wei S.-H., and Al-Jassim M. M. (2010) Electronic, structural, and magnetic effects of 3d transition metals in hematite. *J. Appl. Phys.* **107**, 123712.

Jentzsch T. L., Chun C. L., Gabor R. S., and Penn R. L. (2007) Influence of aluminum substitution on the reactivity of magnetite nanoparticles. *J. Phys. Chem. C* **111**, 10247-10253.

Kerisit S. and Rosso K. M. (2007) Kinetic Monte Carlo model of charge transport in hematite. *J. Chem. Phys.* **127**, 124706.

Klausen J., Trober S. P., Haderlein S. B., and Schwarzenbach R. P. (1995) Reduction of substituted nitrobenzenes by Fe(II) in aqueous mineral suspensions. *Environ. Sci. Technol.* **29**, 2396-2404.

Kleiman-Shwarsctein A., Hu Y.-S., Forman A. J., Stucky G. D., and McFarland E. W. (2008) Electrodeposition of α-Fe_2O_3 doped with Mo or Cr as photoanodes for photocatalytic water splitting. *J. Phys. Chem. C* **112**, 15900-15907.

Kleiman-Shwarsctein A., Huda M. N., Walsh A., Yan Y., Stucky G. D., Hu Y.-S., Al-Jassim M. M., and McFarland E. W. (2010) Electrodeposited aluminum-doped α-Fe_2O_3 photoelectrodes: experiment and theory. *Chem. Mater.* **22**, 510–517.

Larese-Casanova P. and Scherer M. M. (2007) Fe(II) sorption on hematite: New insights based on spectroscopic measurements. *Environ. Sci. Technol.* **41**, 471–477.

Liger E., Charlet L., and Cappellen P. V. (1999) Surface catalysis of uranium(VI) reduction by iron(II). *Geochim. Cosmochim. Acta* **63**, 2939–2955.

Ling Y., Wang G., Wheeler D. A., Zhang J. Z., and Li Y. (2011) Sn-doped hematite nanostructures for photoelectrochemical water splitting. *Nano Lett.* **11**, 2119–2125.

Liu P., Kendelewicz T., Brown G. E., Jr., Nelson E. J., and Chambers S. A. (1998) Reaction of water vapor with α-Al_2O_3(0001) and α-Fe_2O_3(0001) surfaces: Synchrotron X-ray photoemission studies and thermodynamic calculations. *Surf. Sci.* **417**, 53–65.

Mikutta C., Wiederhold J. G., Cirpka O. A., Hofstetter T. B., Bourdon B., and Gunten U. V. (2009) Iron isotope fractionation and atom exchange during sorption of ferrous iron to mineral surfaces. *Geochim. Cosmochim. Acta* **73**, 1795–1812.

Morin F. J. (1951) Electrical properties of α-Fe_2O_3 and α-Fe_2O_3 containing titanium. *Phys. Rev.* **83**, 1005-1010.

Pedersen H. D., Postma D., Jakobsen R., and Larsen O. (2005) Fast transformation of iron oxyhydroxides by the catalytic action of aqueous Fe(II). *Geochim. Cosmochim. Acta* **69**, 3967–3977.

Roden E. E. and Emerson. D. (2007) Microbial metal cycling in aquatic environments. In *Manual of Environmental Microbiology* (ed. C. J. Hurst, D. Lipson, R. Crawford, J. Garland, A. Mills, and L. D. Stezenbach), pp. 540-562. American Society for Microbiology.

Rosso K. M., Yanina S. V., Gorski C. A., Larese-Casanova P., and Scherer M. M. (2010) Connecting observations of hematite (α-Fe_2O_3) growth catalyzed by Fe(II). *Environ. Sci. Technol.* **44**, 61–67.

Schilt A. A. (1969) *Analytical applications of 1,10-phenanthroline and related compounds*. Pergamon Press.

Schwertmann U. and Cornell R. M. (2000) *Iron oxides in the laboratory: Preparation and characterization*. Wiley-VCH.

Shannon R. D. (1976) Revised effective ionic radii and systematic studies of interatomic distances in halides and chalcogenides. *Acta. Cryst.* **A32**, 751-767.

Singh B. and Gilkes R. J. (1992) Properties and distribution of iron oxides and their association with minor elements in the soils of south-western Australia. *J. Soil Sci.* **43**, 77-98.

Smith G. C. (2005) Evaluation of a simple correction for the hydrocarbon contamination layer in quantitative surface analysis by XPS. *J. Electron Spectrosc. Relat. Phenom.* **148**, 21–28.

Strathmann T. J. and Stone A. T. (2003) Mineral surface catalysis of reactions between Fe^{II} and oxime carbamate pesticides. *Geochim. Cosmochim. Acta* **67**, 2775–2791.

Torrent J., Schwertmann U., and Barron V. (1987) The reductive dissolution of synthetic goethite and hematite by dithionite. *Clay. Miner.* **22**, 329–337.

Trolard F., Bourrie G., Jeanroy E., Herbillon A. J., and Martin H. (1995) Trace metals in natural iron oxides from laterites: A study using selective kinetic extraction. *Geochim. Cosmochim. Acta* **59**, 1285-1297.

Waychunas G. A., Fuller C. C., and Davis J. A. (2002) Surface complexation and precipitate geometry for aqueous Zn(II) sorption on ferrihydrite I: X-ray absorption extended fine structure spectroscopy analysis. *Geochim. Cosmochim. Acta* **66**, 1119–1137.

Williams A. G. B. and Scherer M. M. (2004) Spectroscopic evidence for Fe(II)-Fe(III) electron transfer at the iron oxide-water interface. *Environ. Sci. Technol.* **38**, 4782–4790.

Yanina S. V. and Rosso K. M. (2008) Linked reactivity at mineral-water interfaces through bulk crystal conduction. *Science* **320**, 218–222.

Zhang J.-W. and Nancollas G. H. (1990) Mechanisms of growth and dissolution of sparingly soluble salts. *Rev. Mineral. Geochem.* **23**, 365-396.

CHAPTER 5

IRON(II)-MEDIATED REDUCTION AND REPARTITIONING OF STRUCTURALLY INCORPORATED COPPER, COBALT, AND MANGANESE IN IRON OXIDES

To be submitted to *Environmental Science and Technology* as:

Frierdich, A.J., Catalano J.G. (2012) Iron(II)-mediated reduction and repartitioning of structurally incorporated copper, cobalt, and manganese in iron oxides.

ABSTRACT

The reduction of trace elements and contaminants by Fe(II) at Fe(III) oxide surfaces is well documented. The effect of aqueous Fe(II) on the fate of redox-active trace elements structurally incorporated into iron oxides, however, is unknown. Here we investigate the fate of redox-active elements during Fe(II)-activated recrystallization of Cu(II)-, Co(III)-, and Mn(III,IV)-substituted goethite and hematite. Enhanced release of Cu, Co, and Mn to solution occurs upon exposure of all materials to aqueous Fe(II) relative to reactions in Fe(II)-free fluids. The quantity of trace element release increases with pH when Fe(II) is present but decreases with increasing pH in the absence of Fe(II). Co and Mn release from goethite is predicted well using a second-order kinetic model, consistent with the release of redox-inactive elements such as Ni and Zn. Cu release and Co and Mn release from hematite, however, require the sum of two rates to adequately model the kinetic data. Greater uptake of Fe(II) by Cu-, Co-, and Mn-substituted iron oxides relative to analogs containing only redox-inactive elements suggests that net Fe(II) oxidation occurs. Reduction of Cu, Co, and Mn in all materials following reaction with Fe(II) is confirmed by X-ray absorption near-edge structure spectroscopy. This work shows that aqueous Fe(II) repartitions structurally incorporated redox-active trace elements from iron oxides into fluids without net mineral dissolution, and suggests that redox-active trace element release during partial microbial iron reduction may be driven primarily by coupled abiotic Fe(II)-activated recrystallization and reduction.

INTRODUCTION

Biogeochemical iron cycling is ubiquitous in sedimentary and aquatic environments and generates systems with coexisting aqueous Fe(II) and Fe(III) oxide minerals. Secondary abiotic reactions between aqueous Fe(II) and Fe(III) oxides occur readily and may induce mineral transformations, e.g., Fe(II)-catalyzed ferrihydrite conversion to goethite (Hansel et al., 2005), iron isotope fractionation (Crosby et al., 2005), and contaminant reduction, e.g., Cr(VI), U(VI), Pu(IV), and organic contaminants (Buerge and Hug, 1999; Liger et al., 1999; Strathmann and Stone, 2003; Elsner et al., 2004; Boland et al., 2011; Felmy et al., 2011). These processes are driven by coupled electron transfer and atom exchange (ETAE) between aqueous Fe(II) and the Fe(III) oxide surface (Williams and Scherer, 2004; Pedersen et al., 2005; Larese-Casanova and Scherer, 2007; Handler et al., 2009; Beard et al., 2010; Catalano et al., 2010; Rosso et al., 2010), and such reactions can result in complete recrystallization of stable, crystalline iron oxide minerals (Handler et al., 2009; Beard et al., 2010).

The discovery of Fe(II)-Fe(III) ETAE has only been firmly established recently, yet the implications of these reactions on trace element and contaminant fate are already emerging. Current data demonstrate that redox-inactive trace elements are cycled through iron oxide structures (e.g., adsorbed Ni(II) incorporates into mineral and pre-incorporated Ni(II) is released to solution) during Fe(II)-activated recrystallization of goethite and hematite (Chapter 2). These results explain observations from past studies in which enhanced retention of divalent metals by goethite was observed when these elements were adsorbed in the presence of Fe(II) compared to adsorption in Fe(II)-free solutions (Coughlin and Stone, 1995; Cooper et al., 2000). Net trace element release of structurally

incorporated redox-inactive trace elements [i.e., Ni(II) and Zn(II)] from goethite and hematite during reaction with Fe(II), and the chemical controls that affect such release, have been described recently and indicate that such processes likely influence the transport and availability of micronutrients and contaminants (Chapter 3). Many trace elements incorporated into iron oxides, however, are redox-active [e.g., Cu(II), Co(III), and Mn(III)]. Such elements are technologically and economically important metals, essential micronutrients for many microorganisms, plants, and animals, and priority water contaminants. While the reduction of sorbed contaminants by Fe(II) on iron oxide surfaces has been studied extensively, the effect of Fe(II)-Fe(III) ETAE on structurally incorporated redox-active trace elements commonly associated with iron oxides has not been examined.

Here we characterize the effect of aqueous Fe(II) on the speciation of Cu, Co, and Mn incorporated into crystalline iron oxides. The temporal evolution of the fluid composition is monitored during reaction of Cu-, Co-, Mn-, and Co,Mn-di-substituted goethite and hematite with Fe(II) solutions at various pH values. X-ray absorption near-edge structure (XANES) spectroscopy was used to examine the speciation of Cu, Co, and Mn in goethite and hematite before and after reaction.

MATERIALS AND METHODS

Mineral Syntheses

Preparation of Cu-substituted goethite and hematite (here on, termed CuGoe and CuHem) was performed as previously reported for Ni(II)-substituted goethite and hematite (Chapter 2) except that Cu(II) was co-precipitated with Fe(III) instead of Ni(II).

Co-, Mn-, and Co,Mn-di-substituted goethite and hematite (here on, termed CoGoe, MnGoe, CoMnGoe, CoHem, MnHem, and CoMnHem) were prepared by modifying standard methods (Schwertmann and Cornell, 2000). Preparation of CoGoe and MnGoe was performed by adding 125 mL of a solution containing 0.98 M iron(III) nitrate and 0.02 M cobalt(II) chloride or 0.02 M manganese(II) chloride to 225 mL of 5 M NaOH. Synthesis of CoHem and MnHem was performed by adding a 500 mL of a solution containing 0.2156 M iron(III) nitrate and 0.0044 M cobalt(II) chloride or 0.0044 M manganese(II) chloride to 330 mL of 1 M NaOH. Preparation of the di-substituted materials was done in the same manner except the ratio of Fe, Co, and Mn was adjusted such that Co and Mn were each 2 mol%. The preparation of di-substituted iron oxides was done to examine the preferential release of these elements from the same solid. The resulting co-precipitates were heated at 70°C for 14 days under alkaline conditions or at 98°C for 5 days at pH 8 [buffered with 10^{-3} M 4-(2-Hydroxyethyl)-1-piperazinepropanesulfonic acid (EPPS)] to yield goethite or hematite, respectively (Chapter 4). All materials were treated with 1 M HCl at a solid to solution mass ratio of 1:100 to remove residual adsorbed cations and metal hydroxides. All materials were then washed free of electrolytes using de-ionized (DI) water (>18.2 MΩ·cm) and stored as a suspension in DI water until further use.

Mineral Characterization

Trace element composition and dissolution stoichiometry was determined using inductively-coupled plasma optical emission spectrometry (ICP-OES, Perkin-Elmer Optima 7300DV) as described previously (Chapter 4). Iron oxide phase purity was

determined by X-ray diffraction (XRD) on a Rigaku Geigerflex D-MAX/A diffractometer using Cu Kα radiation. Crystal morphology and particle size were examined using a JEOL JSM-7001F field emission scanning electron microscope (SEM) operated at 30 keV. Samples were coated with gold by plasma deposition (Cressington Sputter Coater 108) to improve image quality. BET surface area was measured by N_2 adsorption using a Quantachrome Instruments Autosorb-1. Cu, Co, and Mn K-edge X-ray absorption fine-structure (XAFS) spectra were collected at the Advanced Photon Source in fluorescence yield to determine the metal substitution mechanism and speciation changes resulting from reaction with Fe(II). Detailed XAFS and XANES data collection and analysis procedures are described elsewhere (Appendix Section A1).

Kinetic Experiments

Anoxic experimental conditions were maintained in an anaerobic chamber (4% H_2/96% N_2 atmosphere) using Pd catalysts to eliminate residual O_2. Trace O_2 and CO_2 contents in the chamber, as well as in DI water used for experiments, were further lowered using methods previously described (Chapter 2). Dissolved oxygen in DI water was measured colorimetrically (CHEMetrics test kit K-7511) prior to use and was always below the detection limit of 1 μg/L. Fe(II) stock solutions were prepared from reagent-grade $FeCl_2 \cdot 4H_2O$, then filtered (0.2 μm, MCE) and stored in amber plastic bottles (to prevent photo-oxidation) prior to use.

Kinetic experiments were performed as described in our prior work (Chapter 3). All reactors contained 10^{-2} M NaCl and 1 g/L mineral. Fluid pH was controlled with HCl (pH 4), 10^{-3} M 2-(N-Morpholino)ethanesulfonic acid (MES, pH 5.5), and 10^{-3} M 3-(N-

Morpholino)propanesulfonic acid (MOPS, pH 7 and 7.5). pH drift was minimal (± 0.1 pH unit) throughout the reaction. Fe(II), electrolyte, and buffer were added from a concentrated stock solution and diluted accordingly. A kinetic experiment was initiated by spiking the reactor solution with the target mineral from a concentrated aqueous stock suspension yielding a final reaction volume of 10 mL. Samples were collected at defined intervals by removing the entire suspension with a syringe and immediately filtering (0.2 μm, MCE) the aliquot to remove the iron oxide particles and stop the reaction. The filtrate was then acidified (HNO_3, trace metal grade) inside the anaerobic chamber. Metal concentrations were measured by ICP-OES; all dissolved iron, cobalt, and manganese was assumed to be Fe(II), Co(II), and Mn(II), because Fe(III), Co(III), and Mn(III,IV) solubility is below the ICP-OES detection limit at the pH conditions studied.

RESULTS

Mineral Properties

Goethite materials have greater but more variable specific surface areas than hematite (Table 5-1). These attributes are reflected in SEM images (Figure 5-1) which illustrate particle size variability among different goethite samples and relatively uniform hematite materials regardless of the substituting metal. No apparent impurities are observed in SEM images, as particle morphologies are consistent with goethite and hematite, and no crystalline impurities are detected by XRD except a minor (~1%) goethite component in MnHem (Figure 5-2). Cu, Co, and Mn contents in most materials are near the target stoichiometry of 2 mol% (Table 5-1). Cu and Co dissolve stoichiometrically with Fe for all samples (Figure 5-3) indicating a uniform distribution

within the solid. MnGoe shows stoichiometric dissolution but dissolution is slightly non-stoichiometric when Mn is substituted in hematite, suggesting that Mn is concentrated within the hematite particle interiors or exists as a component resistant to dissolution, e.g., Mn(IV) (Figure 5-3). Co and Mn K-edge XANES spectra indicate that Co and Mn are predominantly trivalent species in most samples (Table 5-1), although some Co(II) and Mn(IV) are also present. In the di-substituted materials Co has a lower average oxidation state (AOS) and Mn has a higher AOS than in the singly-substituted phases, suggesting coupled Co(II)-Mn(IV) substitution for Fe(III) as a charge balancing mechanism. Cu K-edge extended X-ray absorption fine structure (EXAFS) spectra are consistent with Jahn-Teller distorted Cu(II) located within an Fe(III)-octahedral site in both goethite and hematite (Appendix Section A2); the locations of Co and Mn in the mineral structures were not determined.

Fe(II)-activated Trace Element Release

Cu, Co, and Mn-substituted iron oxides were reacted in aqueous fluids buffered at various pH values in the presence and absence of 10^{-3} M Fe(II) to examine the kinetics of trace element release. The fate of Cu during reaction of CuGoe and CuHem with Fe(II) is strongly affected by pH. In the absence of Fe(II) no Cu release is observed at pH 7 but minor release occurs at pH 5.5 from CuHem and at pH 4 for both CuGoe and CuHem (Figure 5-4). Cu release is substantially enhanced from both minerals in the presence of 10^{-3} M Fe(II) at all pH values examined (Figure 5-4). The kinetics of Cu release substantially differ from that observed for redox-inactive metals [e.g., Ni(II) and Zn(II)] examined previously (Chapter 3). At pH 4 and 5.5 rapid Cu release occurs at early times

but slows as the reaction progresses. The data are poorly modeled using a single kinetic equation. An excellent fit to the data is obtained, however, by using the sum of two second-order rate equations with rates, based on observed second-order rate constants (i.e., k_{fast} and k_{slow}), differing by several orders of magnitude (Table 5-2). Cu release from goethite and hematite during reaction with Fe(II) at pH 7 is rapid and reaches maximum concentrations within 5 minutes, which then quickly decrease at a similar rate until they are below detection limit (0.02 μM) (Figure 5-4C). No Cu is detected in solution for the remainder of the reaction (i.e., up to 15 days).

The release of Co and Mn from goethite and hematite is enhanced in the presence of 10^{-3} M Fe(II) relative to Fe(II)-free controls at all pH values examined (Figure 5-5). Release strongly varies with pH but, unlike Cu, the greatest concentrations released to solution occur at circumneutral pH, and such concentrations are maintained or continue to increase during the entire experiment (Figure 5-5). Both Co and Mn release from hematite occurs with a kinetic profile similar to that of Cu; initial rapid release is followed by a slower kinetic process. Consequently, modeling the release from hematite at all pH conditions requires the sum of two second-order equations. Co and Mn release from goethite, however, is modeled well using a single second-order kinetic equation (Table 5-2, Figure 5-5). The rate of Co and Mn release from goethite and hematite at pH 4 and 5.5 is comparable to Cu (Table 5-2) but at circumneutral pH, the observed second-order rate constants for slow release (k_{slow}) decrease by 1-2 orders of magnitude (Table 5-2). Such release is substantially slower than that for redox-inactive elements that were previously investigated (Chapter 3).

The amount of Co and Mn release varies with mineral phase and element type. Greater quantities of both elements are released from hematite compared to goethite but higher Mn concentrations evolve from every mineral type examined (i.e., goethite, hematite, and di-substituted goethite and hematite) relative to Co (Figure 5-5). Co release from both di-substituted iron oxides is elevated relative to Co release from the singly-substituted phases. Mn release from Co,Mn-di-substituted goethite is elevated but not from Co,Mn-di-substituted hematite compared to its singly-substituted phases. At low pH, Co release during reaction with Fe(II) is slightly more than release in the absence of Fe(II). Mn release at these low pH values, however, is substantially greater in the presence of Fe(II) compared to an Fe(II)-free control.

Fe(II) Sorption

The temporal loss of Fe(II) from solution was monitored in conjunction with trace element release to determine how these two processes relate and whether Fe(II) uptake by Cu-, Co-, and Mn-substituted iron oxides differs from Fe(II) sorption by iron oxides substituted with redox-inactive trace elements. The kinetics of Fe(II) sorption during exposure of Cu-, Co, and Mn-substituted materials to 10^{-3} M Fe(II) are similar to our prior work (Chapters 2,3), i.e., rapid uptake with little net change in concentration for the remainder of the experiment (Figure 5-6). Such kinetic behavior differs from that of trace element release. There are, however, substantial differences in the amount of Fe(II) sorption by Cu-, Co-, and Mn-substituted iron oxides compared to iron oxides containing redox-inactive trace elements [i.e., Ni(II) and Zn(II)].

The amount of Fe(II) sorbed increases with pH for all materials (Figure 5-7A,B). No measureable Fe(II) sorption by Ni-substituted goethite (NiGoe) and Zn-substituted hematite (ZnHem) occurs at pH 4, and only a minor amount of uptake occurs at pH 5.5 for NiGoe (Figure 5-7A,B). As the pH is increased further, however, a substantial amount of Fe(II) sorption occurs for NiGoe and ZnHem; this trend is typical for cation sorption on oxide surfaces and the results are consistent with Fe(II) sorption on pure goethite and hematite (Strathmann and Stone, 2003). Similarly, Fe(II) sorption is negligible for Cu-substituted iron oxides at pH 4, although at pH 5.5 and pH 7 Fe(II) removal from solution occurs in excess of that seen for materials containing no reducible trace elements. All materials containing Co and Mn, however, exhibit substantially more Fe(II) uptake at all pH values, with sorption at pH 4 surpassing that at pH 8 for NiGoe and ZnHem (Figure 5-7A,B). The loss of aqueous Fe(II) at low pH suggests that Fe(II) oxidation has occurred as Fe(II) uptake is limited below its sorption edge, which is near pH 7 for goethite, hematite, and iron-free oxide minerals (Strathmann and Stone, 2003; Nano and Strathmann, 2006).

Trace Element Release with Stoichiometrically Limited Fe(II)

The potential for Fe(II) oxidation by Cu(II), Co(III), and Mn(III/IV), and its effect on trace element release, was further explored by reacting all materials with 10^{-4} M Fe(II); only incomplete reduction of the trace elements is possible with this Fe(II) concentration because Fe(II) will be stoichiometrically limiting (Table 5-1). The release behavior of all trace elements differ when Cu-, Co-, and Mn-substituted iron oxides are reacted with 10^{-4} M Fe(II) compared to 10^{-3} M Fe(II) at pH 7. Cu release from CuGoe

and CuHem (Figure 5-8A) occurs with a rate and final concentration that is similar to reaction with 10^{-3} M Fe(II) (Figure 5-4C) although Cu remains in solution longer with concentrations decreasing at a slower rate. When Fe(II) is stoichiometrically limiting, Co and Mn release is reduced, and concentrations reach a maximum, steady state more quickly (Figure 5-8B,C) than observed with 10^{-3} M Fe(II) (Figure 5-5). There is no detectable Co release from CoGoe or CoMnGoe, and the amounts of Co liberated from CoHem and CoMnHem is less than that observed at high Fe(II) concentrations (Figure 5-8B). Mn release (Figure 5-8C) is less affected by lower Fe(II) concentrations than Co but is still less than that observed from reaction with 10^{-3} M Fe(II). Three major trends that were observed for Co and Mn release during reaction with 10^{-3} M Fe(II) still hold for reactions with 10^{-4} M Fe(II): there is more Mn release than Co, both elements are preferentially liberated from hematite compared to goethite, and modeling the release from hematite requires the sum of two rate equations (Figure 5-8B,C).

The uptake kinetics of 10^{-4} M Fe(II) at pH 7 by Cu-, Co-, and Mn-substituted iron oxides differs from that observed at 10^{-3} M Fe(II). Materials containing Co result in the greatest quantities of Fe(II) uptake with complete loss of Fe(II) from solution occurring within 1 hr and 30 d for goethite and hematite, respectively (Figure 5-7C,D). Furthermore, greater quantities of Fe(II) are removed from solution by Cu-, Co-, and Mn-substituted iron oxides compared to NiGoe and ZnHem (Figure 5-7C,D), and Fe(II) concentrations continually decrease rather than stabilizing after several days as observed for NiGoe and ZnHem. These differences are not correlated with mineral surface area (Table 5-1).

Trace Element Oxidation States

The correlation between trace element release and excess Fe(II) uptake by Cu-, Co-, and Mn-substituted iron oxides suggests that these redox-active elements are being reduced. Trace element oxidation states in the solid phase were thus examined by XANES spectroscopy before and after reaction with Fe(II) to identify speciation changes. XANES spectra of CuGoe and CuHem following reaction with Fe(II) contain a prominent pre-edge feature indicative of Cu(I) (Figure 5-9A,B). Linear combination fitting of the XANES spectra shows that 13.6 ± 0.2% and 8.5 ± 0.4% of Cu in CuGoe and CuHem, respectively, is present as Cu_2O. The XANES spectra for all Co- and Mn-substituted iron oxides exhibit a shift to lower energy following reaction with Fe(II), demonstrating reduction of these elements (Figure 5-9C-F). The quantity of Co and Mn reduced exceeds that released to solution, which demonstrates that structural Co and Mn is reduced in situ or that substantial reincorporation of these elements occurs following reduction. AOS quantification (Appendix Section A1) of solid phase Co and Mn indicate that Co(II) is the dominant oxidation state following reaction with Fe(II) whereas Mn exists primarily as Mn(III) (Table 3).

The observed reduction of Co and Mn associated with the solid phase is expected given the release of these elements to solution. For example, Co(III) and Mn(III,IV) initially associated with the solid are insoluble at the pH values considered without a complexant; this points to Co(II) and Mn(II) in solution. Cu reduction at pH 7 is also consistent with the observed release behavior as solubility calculations, using The Geochemist's Workbench® (Bethke, 2009), reveal that about 3 μM Cu(II) should be soluble at pH 7 whereas Cu(I) solubility is below the ICP-OES detection limit. The

speciation of Cu in solution at low pH is less clear as Cu(I) becomes more soluble. However, the limited Fe(II) uptake by Cu-substituted iron oxides at pH 4 (Figure 5.7) suggests that limited Cu reduction occurs at low pH.

DISCUSSION

Release Kinetics and Mechanism

This study demonstrates that the speciation of Cu, Co, and Mn structurally incorporated in iron oxide minerals is affected during Fe(II)-activated recrystallization, resulting in the reduction and repartitioning of these elements. Our prior work (Chapter 3) has shown that Fe(II)-activated Ni(II) and Zn(II) release from goethite and hematite follows a second-order kinetic equation for surface reaction limited mineral dissolution (Berner, 1978; Zhang and Nancollas, 1990). This is mechanistically consistent with release occurring at the sites of reductive dissolution during recrystallization caused by Fe(II)-Fe(III) ETAE. While the release kinetics of Cu, Co, and Mn have some similarities with Ni and Zn release, there are numerous element- and mineral-specific differences that suggest the release of redox-active elements involves different reaction mechanisms.

Co and Mn release from goethite is predicted well using a second-order kinetic model, consistent with the release of redox-inactive elements. Co and Mn release from hematite and Cu release from both iron oxides studied requires the sum of two rates to adequately model their kinetic behavior. This indicates either that there are two processes affecting the release of soluble trace elements or that there is a mid-reaction change in the rate limiting step. The former is expected as we have already shown that trace elements may incorporate into goethite and hematite during Fe(II)-activated recrystallization

(Chapter 2). Furthermore, Fe atom exchange data between aqueous Fe(II) and NiGoe and Ni,Al-di-substituted goethite (Chapter 4) indicate that most of the Ni exposed to solution during Fe(II)-Fe(III) ETAE is immediately reincorporated.

Rapid release of redox-active elements observed at early times may result from oxidation state changes of the substituent, which affect its repartitioning behavior and release to solution. For example, the size of each element, and thus its substitution stability, varies with oxidation state. Trivalent Co and Mn are similar in size to Fe(III) but their divalent forms are larger than Fe(III) by 0.1 and 0.2 Å, respectively (Shannon, 1976). Consequently, the rapid release of these elements at early times may reflect the unfavorable reincorporation of Mn(II) and Co(II) and thus enhanced release. As their concentrations buildup in solution, re-adsorption and incorporation may result in the slow rate observed at longer times. The absence of such a phenomenon for goethite may be explained by its structure, which can accommodate larger ions, e.g., octahedral Zn (Chapter 3) and Sn(IV) with little unit-cell expansion (Chapter 4), whereas the relaxation of the oxygen lattice in hematite is more constrained, reducing the favorability of incorporation of larger substituents. As a result, the reincorporation of Co(II) and Mn(II) may be highly favorable in goethite but such reincorporation into hematite can only occur when the concentrations of these elements in solution are elevated. A size-stability relationship comparison for Cu(II) is difficult to evaluate because of its Jahn-Teller distortion.

Alternatively, a mid-reaction change in the rate limiting step caused by net Fe(II) oxidation may result in the requirement to model Co and Mn release from hematite and Cu release from both iron oxides with the sum of two rates. The concentration of Fe(II)

has been demonstrated to affect both the rate and amount of trace element release (Chapter 3). Consequently, oxidation of Fe(II) by Cu(II), Co(III) and Mn(III,IV) results in less aqueous Fe(II) to compete with Cu(I,II), Co(II) and Mn(II) for surface sites thus leading to greater uptake of trace elements by the minerals. Lower Fe(II) concentrations would also result in less or slower recrystallization and therefore limited amounts of trace element release to solution. Additionally, net Fe(II) oxidation may form a passivating surface layer, thus inhibiting further trace element release from deeper layers within the mineral. The slower Fe(II) oxidation by Co- and Mn-substituted hematite, and Cu-substituted iron oxides, compared to goethite analogs (Figure 5-7C,D) may explain why slow release only dominates at later reaction times. Net Fe(II) oxidation is also consistent with the generally slow release of Co and Mn compared to other elements as Co- and Mn-substituted iron oxides take up the greatest amounts of Fe(II) (Figure 5-7A,B).

Differences in Co and Mn Partitioning

Greater quantities of Mn are released from goethite, hematite, and di-substituted goethite and hematite relative to Co. Differences in release have been observed for Ni- and Zn-substituted iron oxides, with greater Ni release from goethite and greater Zn release from hematite (Chapter 3). These differences could not be attributed to differences in surface area, metal content, or metal distribution within the structure, leading to the conclusion that relative release is either related to differences in recrystallization or in the repartitioning behavior of the elements (Chapter 3). Similarly, differences in Co and Mn release cannot be attributed to differences in mineral surface area as enhanced Mn release is observed even for the di-substituted materials.

Additionally, bulk compositions for Co and Mn in the same phase are comparable (<8% difference for CoMnGoe and <6% for CoMnHem) whereas the differences in release vary by factors of 2-3 (Table 5-2). Furthermore, the reduction potentials of Co(III) and Mn(III) are similar (Mcardell et al., 1998) indicating that preferential reduction is not a factor. Based on the substantial amounts of Mn released to solution and the absence of Mn(II) in the solids following reaction with Fe(II), Mn(II) appears to be unstable within goethite and hematite. However, abundant Co(II) is associated with the solid, particularly after Fe(II) exposure, suggesting that Co(II) has greater stability than Mn(II) within the mineral structures. These results are consistent with the expected substitution stability of these elements based on their ionic radii, i.e., octahedral Mn(II) is 0.1 Å larger than octahedral Co(II) (Shannon, 1976). Furthermore, the persistence of structural Mn(III), which is similar in size to Fe(III), following reaction with Fe(II) (Table 5-3) indicates that trivalent Mn is the most stable form in both goethite and hematite.

Environmental Implications

Homogeneous (Biddle, 1901; Matocha et al., 2005) and heterogeneous (O'loughlin et al., 2003a) reduction of Cu(II) by Fe(II) is known and has been implicated as an important control on the fate of Cu in the environment and in the formation of native Cu deposits (Biddle, 1901; Cornwall, 1956). Reduction of Cu(II) to Cu(0) by structural Fe(II) in green rust has been reported (O'loughlin et al., 2003a; O'loughlin et al., 2003b) whereas only reduction to Cu(I) was observed for the homogeneous reaction with aqueous Fe(II) and the reaction of Fe(II) and Cu(II) on goethite surfaces (Maithreepalaand and Doong, 2004; Matocha et al., 2005). The substantial amount of

Cu(II) associated with the solid following reaction with Fe(II) in our study points to Cu(II)-substituted in iron oxides as being more resistant to reduction.

The reduction of Mn(III,IV) oxides by Fe(II) occurs readily and the reaction can elevate Mn(II) concentrations in groundwater and separate Mn from Fe in sediments (Postma, 1985; Postma and Appelo, 2000). Our work shows that aqueous Fe(II) can remove structurally incorporated Mn(III,IV) from iron oxides, thus revealing a new mechanism for the redistribution of these two elements. The effect of Fe(II) on Co(III) is less certain. Congruent dissolution of Mn and Co from substituted goethite has been observed during microbial iron reduction (Bousserrhine et al., 1999) although these materials were almost completely dissolved (>90%) within 6 days. Thus, the effect of Fe(II) is uncertain, as Fe(II)-activated recrystallization occurs on a longer timescale. Partial microbial reduction (≤45%) of Co-substituted goethite over 32 days has also been reported to result in enhanced release of Co(II) relative to Fe(II) (Zachara et al., 2001). Microbially-mediated co-reduction of Co(III) and Fe(III) was assumed in this study but our work provides clear evidence that Fe(II) can abiotically reduce Co(III), releasing Co(II) to solution. The partitioning of trace elements during microbial iron cycling is well known (Roden and Emerson, 2007) and often assumed to result directly from microbial processes. Our work, however, illustrates the importance of Fe(II)-Fe(III) ETAE on the mobilization and speciation of redox-active trace elements during microbial iron cycling and suggests that such secondary abiotic reactions exert a major control on trace element and contaminant fate in aquatic systems.

ACKNOWLEDGEMENTS

This work was supported by the National Science Foundation (NSF) through Grant No. EAR-0818354. ICP-OES analyses were performed at the Nano Research Facility at Washington University in St. Louis, which is supported by the NSF under award ECS-0335765. Portions of this work were performed at the Advanced Photon Source (APS) at beamlines 20-BM (PNC/XSD) and 5-BM-D (DND-CAT). PNC/XSD facilities, and research at these facilities, are supported by the US Department of Energy - Basic Energy Sciences, a Major Resources Support grant from NSERC, the University of Washington, Simon Fraser University and the APS. DND-CAT is supported by DuPont, Dow Chemical Company, and Northwestern University. Use of the APS, an Office of Science User Facility operated for the U.S. Department of Energy (DOE) Office of Science by Argonne National Laboratory, was supported by the U.S. DOE under Contract No. DE-AC02-06CH11357.

Table 5-1. Iron oxide properties and reactor conditions.

Sample ID	Surface Area (m^2 g^{-1})	Substituent Composition (mol%)	Substituent AOS[a]	Initial [Me] (μM)[b]
CuGoe	41.1	1.86 Cu	2.00 Cu[c]	209 Cu
MnGoe	27.6	2.25 Mn	3.21 Mn	253 Mn
CoGoe	19.8	2.16 Co	2.91 Co	243 Co
CoMnGoe	47.1	1.97 Co 2.14 Mn	2.58 Co 3.39 Mn	222 Mn 241 Co
CuHem	12.7	1.56 Cu	2.00 Cu	195 Cu
MnHem	17.3	2.21 Mn	2.96 Mn	277 Mn
CoHem	15.4	2.07 Co	2.56 Co	259 Co
CoMnHem	13.8	2.09 Co 2.22 Mn	2.18 Co 3.52 Mn	262 Co 278 Mn

[a] Average oxidation state.
[b] Amount of incorporated Cu, Co, or Mn in each reactor for 1 g/L solid suspension.
[c] Cu assumed to be divalent as the syntheses were conducted under oxidizing conditions.

Table 5-2. Kinetic fitting parameters for Cu, Co, and Mn release.

Sample ID	k_{fast} / k_{slow} (μM^{-1} d^{-1})	$[Me]_{fast}$ / $[Me]_{slow}$ (μM)
CuGoe		
pH 4	1000[a] / 0.28(7)	0.71(7) / 1.72(9)
pH 5.5	70(40) / 0.4(2)	2.8(3) / 2.8(3)
pH 7	–[b] / –	– / –
MnGoe		
pH 4	– / 0.4(2)	– / 2.3(2)
pH 5.5	– / 0.19(9)	– / 3.6(3)
pH 7	– / 0.019(4)	– / 9.6(5)
pH 7.5	– / 0.015(3)	– / 12.0(6)
CoGoe		
pH 4	– / 0.6(3)	– / 0.67(6)
pH 5.5	– / 0.6(4)	– / 0.65(7)
pH 7	– / 0.0076(5)	– / 6.5(1)
pH 7.5	– / 0.020(4)	– / 5.9(2)
CoMnGoe		
pH 4	– / 0.4(2) Co – / 0.20(9) Mn	– / 1.15(8) Co – / 4.8(3) Mn
pH 5.5	– / 0.3(2) Co – / 0.2(1) Mn	– / 0.9(1) Co – / 5.6(5) Mn
pH 7	– / 0.0020(5) Co – / 0.004(2) Mn	– / 12.4(9) Co – / 18(3) Mn
pH 7.5	– / 0.006(1) Co – / 0.007(2) Mn	– / 10.7(5) Co – / 21(1) Mn
CuHem		
pH 4	40(70) / 0.11(9)	2.5(3) / 2.4(1)
pH 5.5	100(30) / 0.25(9)	4.2(2) / 2.7(2)
pH 7	– / –	– / –
MnHem		
pH 4	1000[a] / 0.2(2)	6.0(3) / 1.7(3)
pH 5.5	500(200) / 0.019(6)	7.0(5) / 8.5(6)
pH 7	0.6(3) / 0.002(2)	24(3) / 24(5)
pH 7.5	80(80) / 0.03(1)	11(3) / 31(3)
CoHem		
pH 4	100(200) / 0.3(3)	2.0(5) / 1.0(4)
pH 5.5	1700(800) / 0.4(1)	1.8(2) / 1.5(2)
pH 7	5(3) / 0.005(2)	3.6(5) / 11.0(8)
pH 7.5	2(1) / 0.003(2)	5.4(7) / 11(2)
CoMnHem		
pH 4	60(20) / 0.03(2) Co 12(2) / 0.03(2) Mn	2.44(7) / 1.2(2) Co 5.0(1) / 1.5(3) Mn
pH 5.5	2000(2000) / 0.3(1) Co 400(100) / 0.8(5) Mn	2.1(2) / 1.6(2) Co 5.1(3) / 1.8(3) Mn
pH 7	4(4) / 0.003(1) Co 200(200) / 0.003(1) Mn	5(1) / 18(2) Co 7(1) / 26(2) Mn
pH 7.5	2(2) / 0.002(1) Co 2(2) / 0.002(1) Mn	6(1) / 19(3) Co 12(2) / 29(4) Mn

[a] k_{fast} was fixed to this value because it could not be constrained by the data.

[b] Dash (–) indicates data was not fit or fit with a single kinetic model.

Table 5-3. Average oxidation state of Cu, Co, and Mn determined from XANES spectra before and after reaction with 10^{-3} M Fe(II). CuGoe and CuHem were reacted at pH 7 for 26 days. Co- and Mn-substituted iron oxides were reacted at pH 7.5 for 60 days.

Sample ID	Me AOS[a] Initial	Me AOS[a] Final	Amount Reduced (μM)[b]	Percent Reduced[c]
CuGoe	2.00 Cu	1.86 Cu	28 Cu	13.6 Cu
MnGoe	3.21 Mn	2.90 Mn	89 Mn	29 Mn
CoGoe	2.91 Co	2.51 Co	100 Co	45 Co
CoMnGoe	2.58 Co 3.39 Mn	2.32 Co 3.23 Mn	61 Co 64 Mn	47Co 19 Mn
CuHem	2.00 Cu	1.92 Cu	17 Cu	8.5 Cu
MnHem	2.96 Mn	2.89 Mn	57 Mn	21 Mn
CoHem	2.56 Co	2.12 Co	116 Co	80 Co
CoMnHem	2.18 Co 3.52 Mn	2.00 Co 3.02 Mn	47 Co 181 Mn	100 Co 43 Mn

[a] Me average oxidation state (AOS) for solid only.
[b] Trace element reduction for entire system. Refers to electrons transferred to Me.
[c] Percent reduction for entire system. Refers to electron equivalents for Mn as both Mn(III) and Mn(IV) are present.

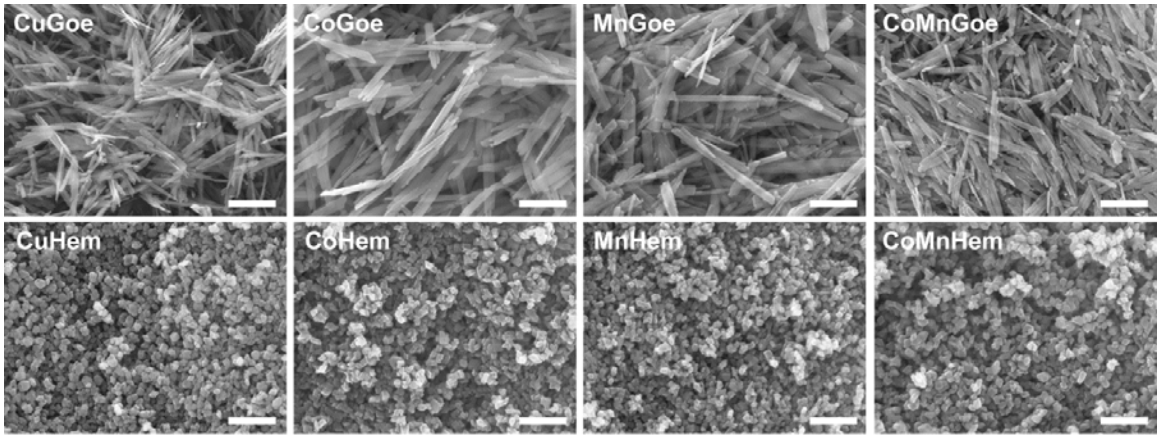

Figure 5-1. SEM images of Cu-, Co-, Mn-, and Co,Mn-di-substituted (top) goethite and (bottom) hematite particles. Scale bar is 1 micron.

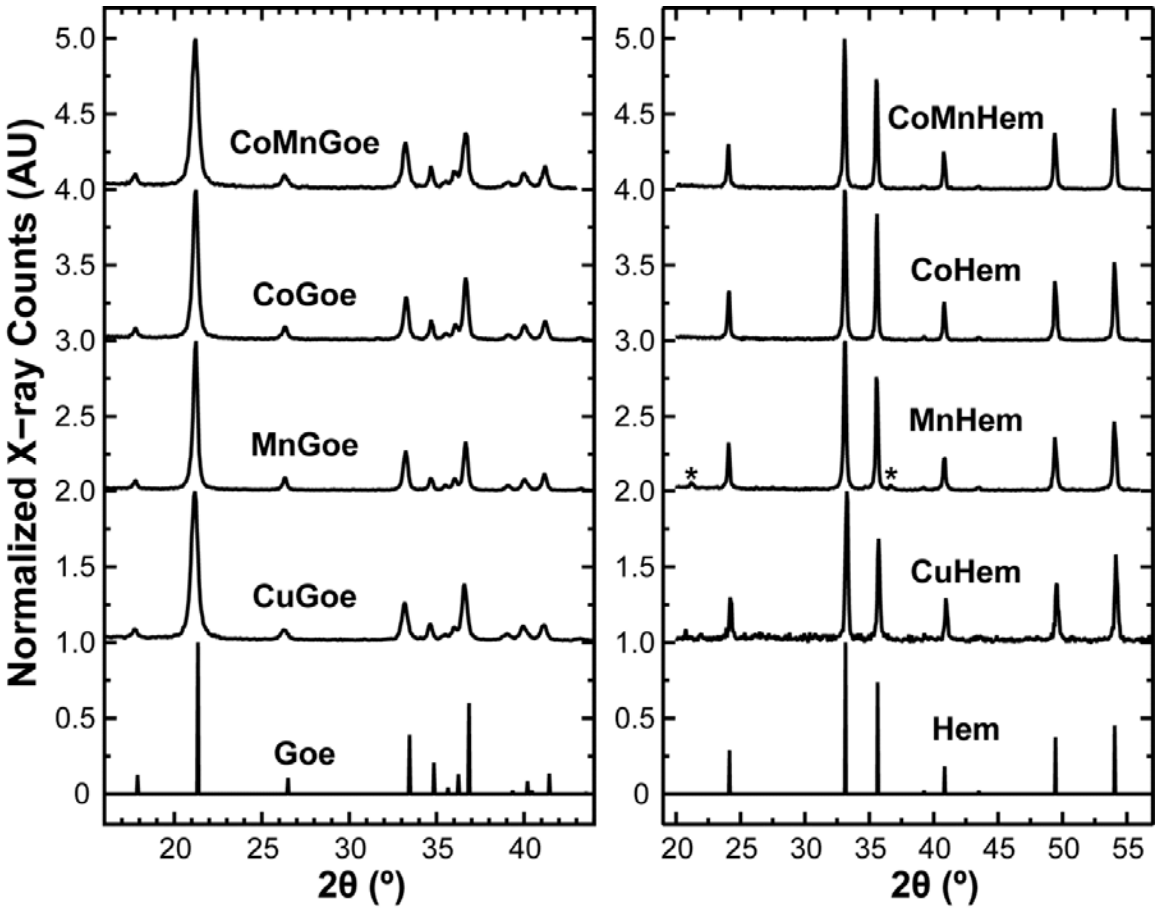

Figure 5-2. (A) XRD patterns of Cu-, Co-, Mn-, and Co,Mn-di-substituted goethite and hematite. Calculated XRD line positions and relative intensities for goethite and hematite are also shown for comparison. Asterisk denotes the presence of goethite impurity.

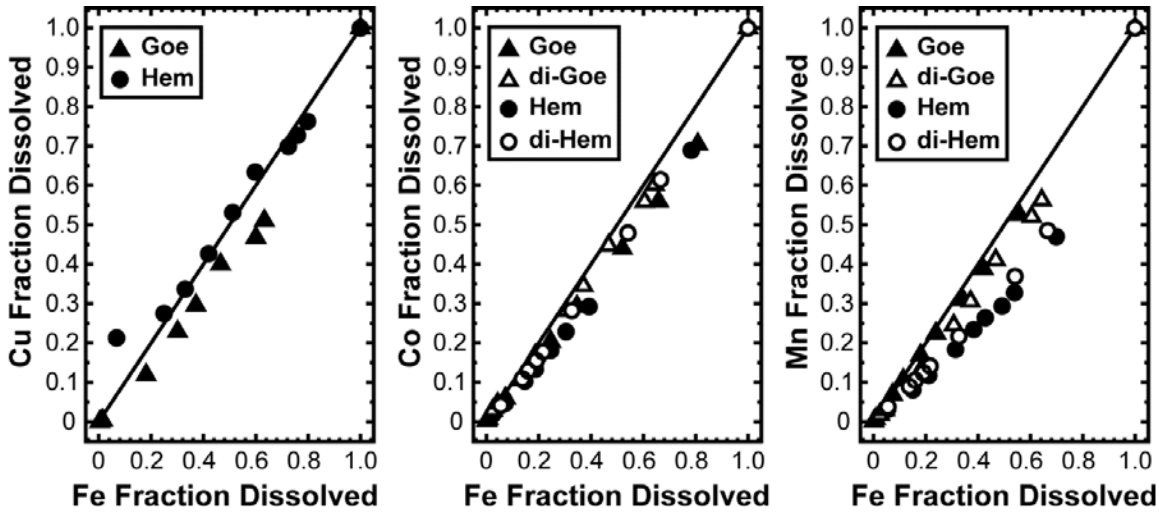

Figure 5-3. Fraction of Cu, Co, or Mn dissolved during complete acid dissolution of Cu-, Co-, Mn-, or Co,Mn-di-substituted goethite and hematite. Solid line represents 1:1 dissolution.

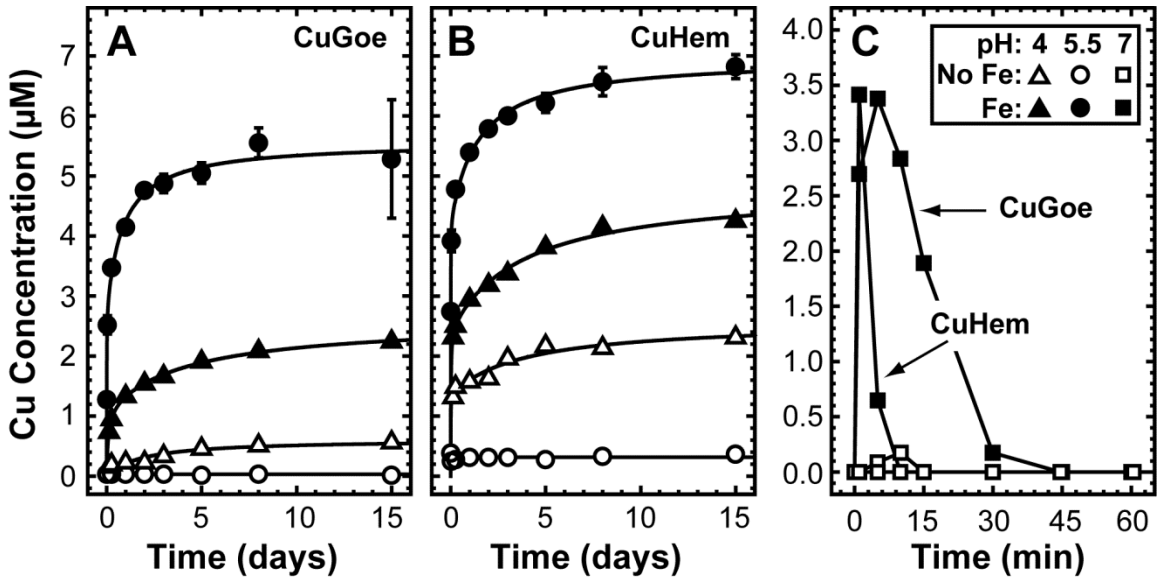

Figure 5-4. Evolution of aqueous copper concentrations during reaction of (A) CuGoe and (B) CuHem with 10^{-3}M Fe(II) at pH 4 and 5.5. Solid curves represent second-order kinetic model fits using the sum of two rates. (C) Cu concentration during reaction of CuGoe and CuHem with 10^{-3}M Fe(II) at pH 7. Solid lines connecting points in panel C are guides, not kinetic fits. All reactions contain 1 g/L of solid.

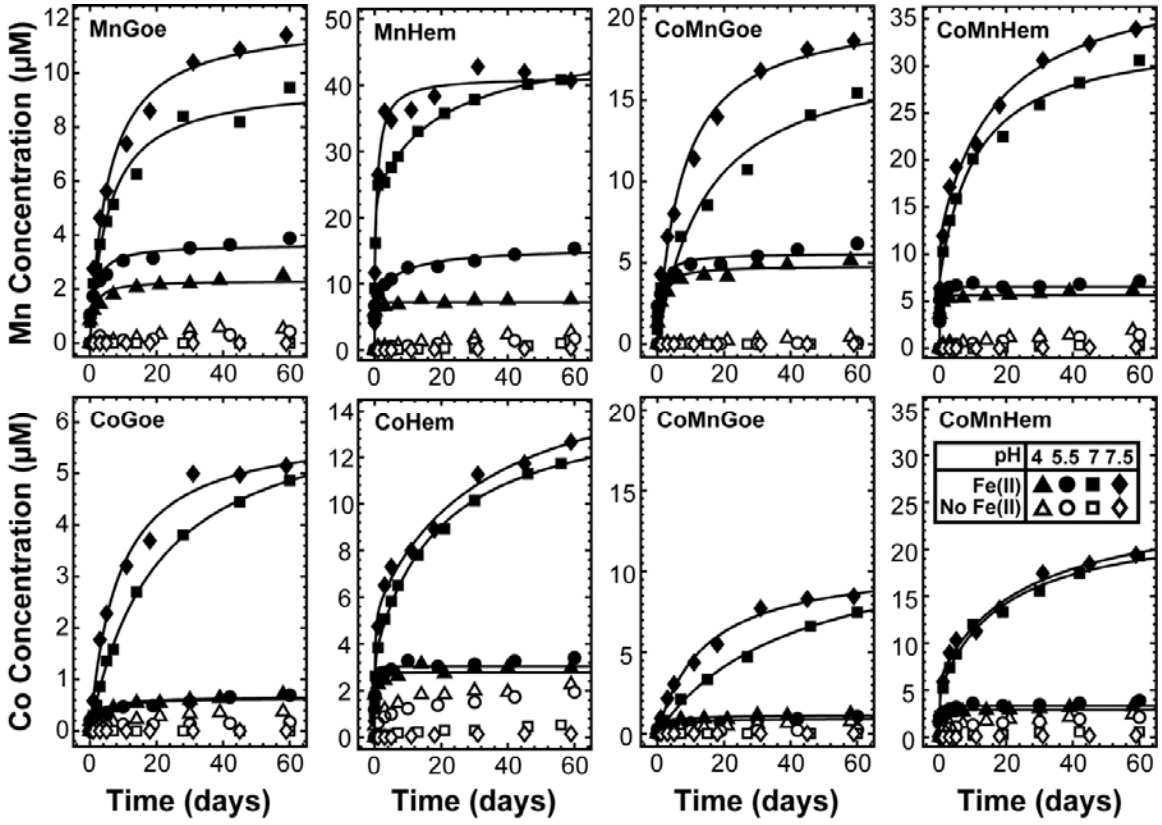

Figure 5-5. Evolution of aqueous Co and Mn concentrations during reaction of Co-, Mn-, and Co,Mn-di-substituted goethite and hematite with 10^{-3}M Fe(II) and Fe(II)-free solutions at various pH. Solid lines represent single and the sum of two second-order kinetic model fits for goethite and hematite, respectively. Solid concentration is 1 g/L for each reaction.

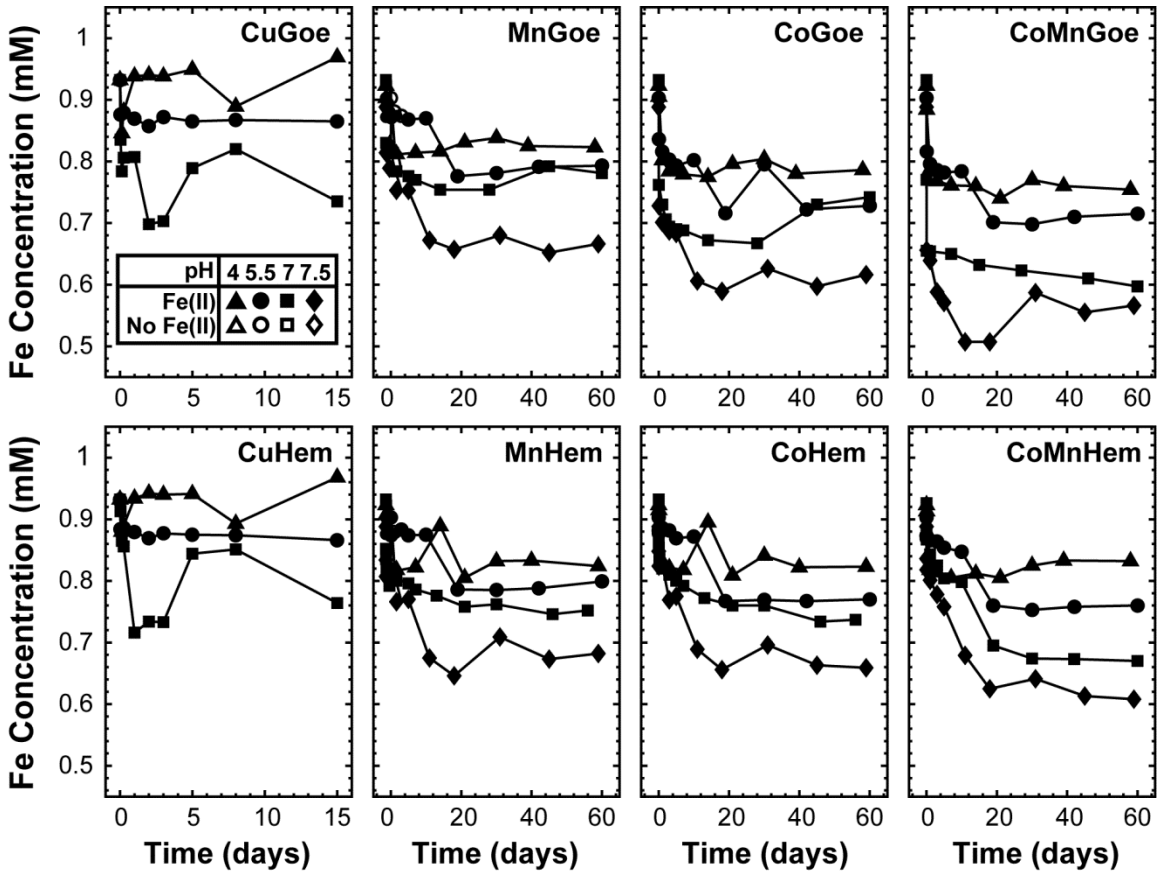

Figure 5-6. Fe(II) sorption by Cu-, Co-, Mn-, and Co,Mn-di-substituted goethite and hematite during reaction with 10^{-3} M Fe(II) at various pH.

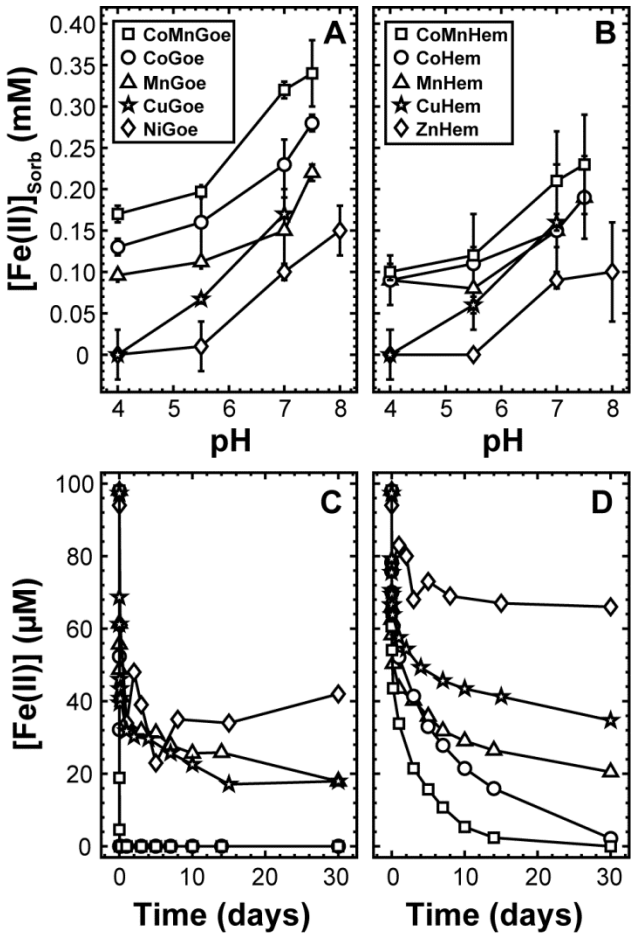

Figure 5-7. (A,B) Fe(II) sorbed to trace element substituted iron oxides at various pH values following 15 days of reaction for NiGoe, ZnHem, CuGoe, and CuHem. Fe(II) uptake by Co- and Mn-substituted iron oxides was determined after 60 days of reaction.$[Fe(II)]_{sorb}$ determined by subtracting the average of the last four time points (Figure 5-7) from the measured initial Fe(II) concentration (i.e., no solid present) Target initial Fe(II) concentration is 10^{-3} M. (C,D) Temporal uptake of Fe(II) by trace element substituted iron oxides at pH 7. All experiments contain 1 g/L of solid. Goethite and hematite containing redox-inactive metals discussed in prior work (Chapter 3) shown for comparison.

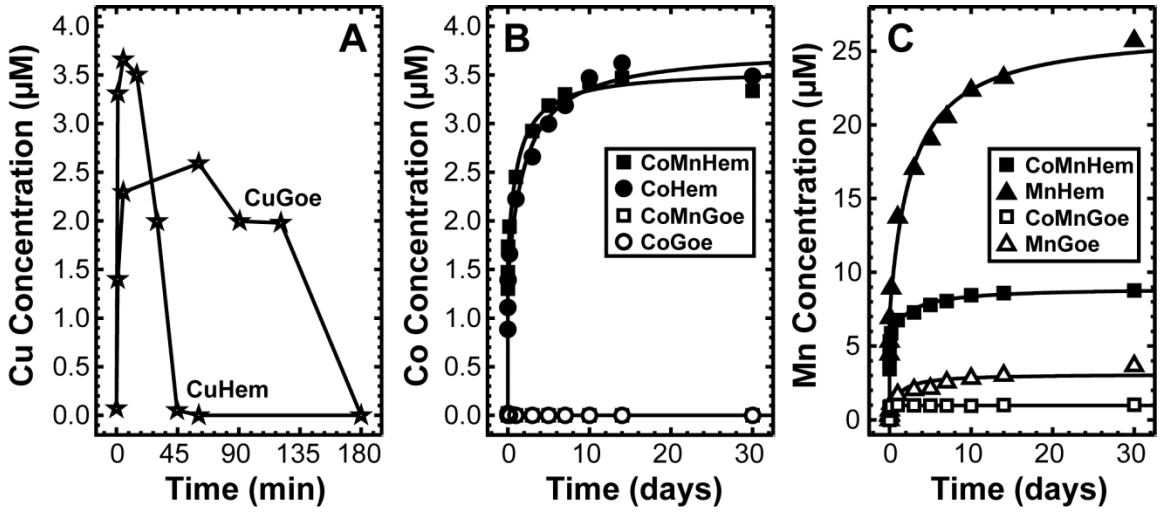

Figure 5-8. (A) Cu, (B) Co, and (C) Mn release from trace element-substituted goethite and hematite during reaction with 10^{-4} M Fe(II) at pH 7.

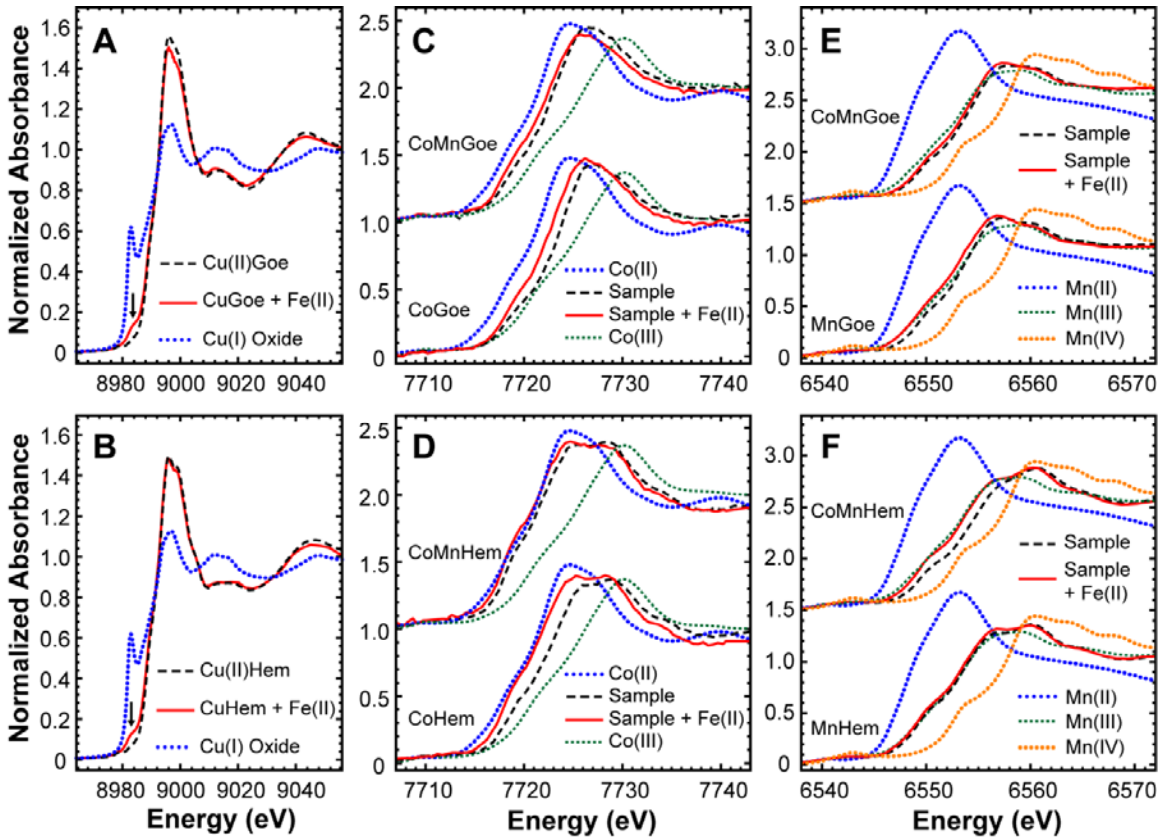

Figure 5-9. (A,B) Cu K-edge XANES spectra for Cu-substituted iron oxides before and after reaction with 10^{-3} M Fe(II) for 26 days at pH 7 compared to a Cu(I) oxide reference. (C,D) Co and (E,F) Mn K-edge XANES spectra for Co-, Mn-, and Co,Mn-di-substituted iron oxides before and after reaction with 10^{-3} M Fe(II) at pH 7.5 for 60 days.

CHAPTER 5 APPENDIX

SECTION A1. EXAFS AND XANES DATA COLLECTION AND ANALYSIS

EXAFS and XANES measurements on Cu-substituted iron oxide samples were done on beamline 20-BM (PNC/XSD) at the Advanced Photon Source at Argonne National Laboratory in fluorescent yield mode. Beam energy was controlled using a Si(111) double-crystal monochromator, and harmonic content of the X-ray beam was reduced by detuning the second crystal of the monochromator by 10% and by insertion of a Rh-coated harmonic rejection mirror (cutoff energy of ~16 keV) 1 m before the sample. The beam was focused both vertically and horizontally to a size of 700 μm; focusing was primarily done to increase the usable X-ray flux of the beamline. Samples were mounted as dry powders and sealed in polycarbonate holders with Kapton^{TM} tape. Samples reacted with Fe(II) were mounted as a wet paste and heat sealed in polyethylene bags to maintain anoxic conditions.

XANES measurements on Co- and Mn-substituted iron oxides were performed on beamline 5-BM-D at the Advanced Photon Source at Argonne National Laboratory in fluorescent yield mode. The incident beam energy was selected using a Si(111) double-crystal monochromator. The harmonic content of the X-ray beam was reduced by detuning the second crystal of the monochromator by 40% and by insertion of a pair of Rh-coated harmonic mirrors. Pre-reaction samples were mounted as dry powders and sealed in polycarbonate holders with Kapton^{TM} tape. Samples reacted with Fe(II) were collected on a removable syringe filter inside an anaerobic chamber, dried, and then sealed on the filter with Kapton^{TM} tape.

The X-ray energy was calibrated by setting the maximum in the first derivative of the X-ray absorption near-edge structure spectrum of Cu, Co, and Mn metal foils to 8979 eV, 7709 eV, and 6539 eV for the Cu, Co, and Mn K-edges, respectively. The normalized and background subtracted k^3-weighted EXAFS spectra of Cu were quantitatively analyzed in SixPACK using phase and amplitude functions in FEFF 7.02 (Ankudinov et al., 1998) using structures of goethite [α-FeOOH] (Gualtieri and Venturelli, 1999) and hematite [α-Fe_2O_3] (Blake et al., 1966) containing a Cu atom substituted into an Fe(III)-octahedral site. Coordination number (N), interatomic distance (R), and σ^2 (a Debye–Waller-type factor based on a Gaussian distribution of interatomic distances), were refined using a nonlinear least-squares fitting routine. The amplitude reduction factor, S_0^2, was fixed to 0.9 for spectral fitting.

Average oxidation states of Co and Mn were determined by using the half-height energies of the absorption edge (i.e., energy at which the absorption is half of the step height for a background subtracted and normalized spectrum). Co(II) and Co(III) spectral standards were obtained from prior work (Catalano et al., 2005). A Mn(II) standard was obtained by collecting a XANES spectrum on a 0.5 M Mn(II) chloride solution in transmission mode. Mn(III) and Mn(IV) spectral standards were also obtained in transmission mode by analysis of Mn(III) and Mn(IV) oxide samples (Sigma-Aldrich) dispersed on scotch tape. The half-height energy calibration line for Mn oxidation state standards was linear (R^2>0.999).

SECTION A2. COPPER SUBSTITUTION IN GOETHITE AND HEMATITE

Cu K-edge EXAFS spectra are consistent with Jahn-Teller distorted Cu(II) locating within an Fe(III)-octahedral site in both goethite and hematite (Table A5-1, Figure A5-1). The Cu coordination environment in both minerals was modeled well using a split oxygen shell with the coordination numbers fixed to 4 and 2 for the equatorial and axial oxygen atoms, respectively. Furthermore, each of the Fe shell coordination numbers was fixed to its crystallographic value. Little distortion of the hematite structure is observed as a result of Cu substitution as each of the three nearest Fe shells yield distances close to that for the known crystal structure (Table A5-1), indicating that Cu is located in an Fe(III)-octahedral site. Cu substitution in goethite, however, resulted in more structural distortion than observed for hematite. The first nearest Fe shell was fit well while the second resulted in a distance shorter than expected (Table A5-1). There was difficulty in fitting the third Fe shell for goethite. In the ideal goethite structure this shell consists of two pairs of Fe atoms, with each pair located in a different neighboring double octahedral chain. While all four of these Fe atoms are equidistant from the octahedral cation site in the normal goethite structure, the spectrum for CuGoe could not be reproduced using such a configuration of neighboring atoms. Instead, the third Fe shell was split into two shells (coordination number fixed to 2 for each) with each having a unique distance from Cu. This approach yielded a satisfactory fit (Table A5-1, Figure A5-1) and is consistent with a Jahn-Teller distortion of the Cu octahedron which would asymmetrically split the Fe neighbor distances.

Table A5-1. EXAFS spectra structural fitting results for Cu-substituted iron oxides.

Sample	EXAFS						Structure[a]	
	Shell	N^b	R (Å)	σ^2 (Å^2)	ΔE_0 (eV)	χ_ν^2	N	R (Å)
CuHem	O	4	1.986(8)[c]	0.0056(6)	-4(1)	3.2	3	1.946
	O	2	2.17(2)	0.008(2)	-4(1)		3	2.116
	Fe[d]	4	2.928(8)	0.0095(5)	-4(1)		4	2.953
	Fe	3	3.39(1)	0.0080(9)	-4(1)		3	3.364
	Fe	6	3.69(1)	0.012(1)	-4(1)		6	3.705
CuGoe	O	4	1.98(2)	0.006(2)	-4(3)	17.3	3	1.937
	O	2	2.14(5)	0.010(7)	-4(3)		3	2.088
	Fe	2	2.97(2)	0.007(2)	-4(3)		2	3.013
	Fe	2	3.15(4)	0.007(2)	-4(3)		2	3.292
	Fe	2[e]	3.37(7)	0.013(4)	-4(3)		4[e]	3.431
	Fe	2[e]	3.86(5)	0.013(4)	-4(3)			

[a] Coordination numbers and interatomic distances from iron site derived from the crystal structures of the minerals.
[b] Fixed to crystallographic values for Fe shells except where noted.
[c] Statistical uncertainties in the last digit are reported in parentheses at the 95% confidence level.
[d] Represents multiple unresolvable neighbors.
[e] Spectrum could not be fit using a single Fe shell due to Jahn-Teller distortion.

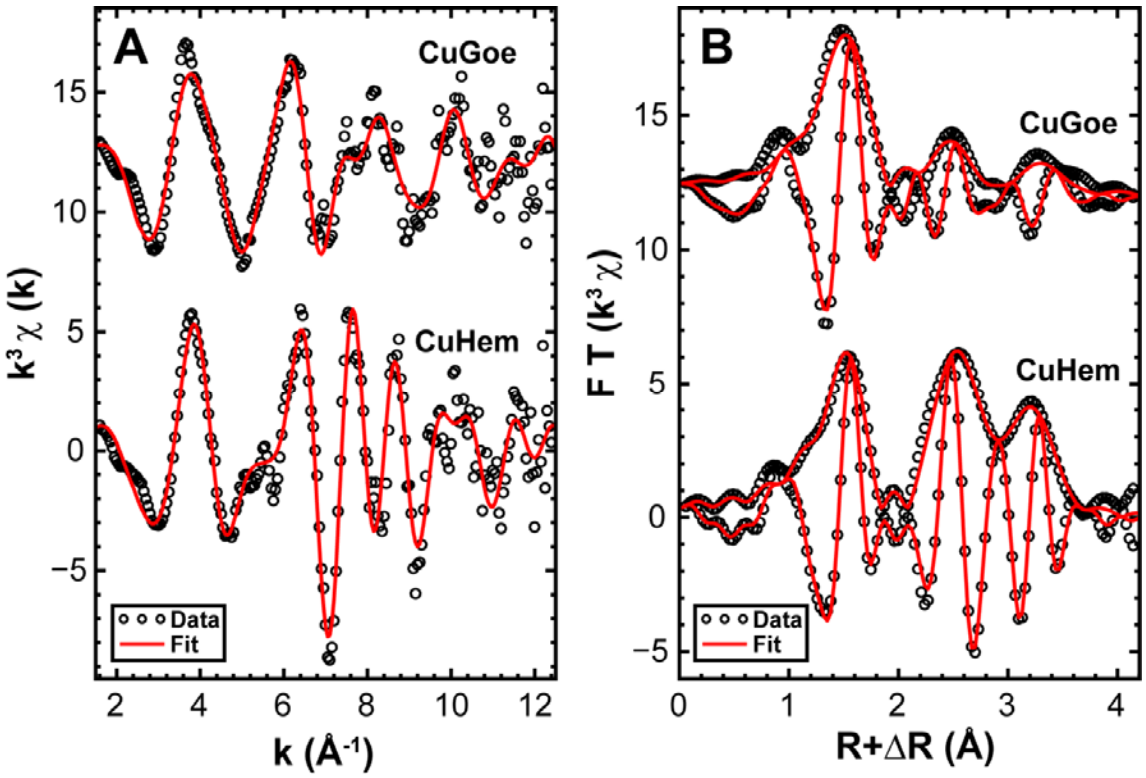

Figure A5-1. (A) Cu K-edge EXAFS spectra (points) and structural model fits (lines) for Cu-substituted goethite and Cu-substituted hematite. (B) Fourier transform magnitudes and real components of EXAFS spectra (points) and corresponding structural model fits (lines).

REFERENCES

Ankudinov A. L., Ravel B., Rehr J. J., and Conradson S. D. (1998) Real-space multiple-scattering calculation and interpretation of x-ray-absorption near-edge structure. *Phys. Rev. B* **58**, 7565–7576.

Beard B. L., Handler R. M., Scherer M. M., Wu L., Czaja A. D., Heimann A., and Johnson C. M. (2010) Iron isotope fractionation between aqueous ferrous iron and goethite. *Earth Planet. Sc. Lett.* **295**, 241–250.

Berner R. A. (1978) Rate control of mineral dissolution under Earth surface conditions. *Am. J. Sci.* **278**, 1235-1252.

Bethke C. M. (2009) The Geochemist's Workbench Release 8.0. Hydrogeology Program, University of Illinois, Urbana, IL.

Biddle H. C. (1901) The deposition of copper by solutions of ferrous salts. *J. Geol.* **9**, 430-436.

Blake R. L., Hessevick R. E., Zoltai T., and Finger L. W. (1966) Refinement of the hematite structure. *Am. Mineral.* **51**, 123-129.

Boland D. D., Collins R. N., Payne T. E., and Waite T. D. (2011) Effect of amorphous Fe(III) oxide transformation on the Fe(II)-mediated reduction of U(VI). *Environ. Sci. Technol.* **45**, 1327-1333.

Bousserrhine N., Gasser U. G., Jeanroy E., and Berthelin J. (1999) Bacterial and chemical reductive dissolution of Mn-, Co-, Cr-, and Al-substituted goethites. *Geomicrobiol. J.* **16**, 245-258.

Buerge I. J. and Hug S., J. (1999) Influence of mineral surfaces on chromium(VI) reduction by iron(II). *Environ. Sci. Technol.* **33**, 4285–4291.

Catalano J. G., Warner J. A., and Brown G. E., Jr. (2005) Sorption and precipitation of Co(II) in Hanford sediments and alkaline aluminate solutions. *Appl. Geochem.* **20**, 193–205.

Catalano J. G., Fenter P., Park C., Zhang Z., and Rosso K. M. (2010) Structure and oxidation state of hematite surfaces reacted with aqueous Fe(II) at acidic and neutral pH. *Geochim. Cosmochim. Acta* **74**, 1498–1512.

Cooper C. D., Picardal F., Rivera J., and Talbot C. (2000) Zinc immobilization and magnetite formation via ferric oxide reduction by *Shewanella* putrefaciens 200. *Environ. Sci. Technol.* **34**, 100-106.

Cornwall H. R. (1956) A summary of ideas on the origin of native copper deposits. *Econ. Geol.* **51**, 615-631.

Coughlin B. R. and Stone A. T. (1995) Nonreversible adsorption of divalent metal ions (Mn(II), Co(II), Ni(II), Cu(II), and Pb(II)) onto goethite: Effects of acidification, Fe(II) addition, and picolinic acid addition. *Environ. Sci. Technol.* **29**, 2445–2455.

Crosby H. A., Johnson C. M., Roden E. E., and Beard B. L. (2005) Coupled Fe(II)-Fe(III) electron and atom exchange as a mechanism for Fe isotope fractionation during dissimilatory iron oxide reduction. *Environ. Sci. Technol.* **39**, 6698–6704.

Elsner M., Schwarzenbach R. P., and Haderlein S. (2004) Reactivity of Fe(II)-bearing minerals toward reductive transformation of organic contaminants. *Environ. Sci. Technol.* **38**, 799–807.

Felmy A. R., Moore D. A., Rosso K. M., Qafoku O., Rai D., Buck E. C., and Ilton E. S. (2011) Heterogeneous Reduction of PuO_2 with Fe(II): Importance of the Fe(III) Reaction Product. *Environ. Sci. Technol.* **45**, 3952–3958.

Gualtieri A. and Venturelli P. (1999) In situ study of the goethite-hematite phase transformation by real time, synchrotron powder diffraction. *Am. Mineral.* **84**, 895–904.

Handler R. M., Beard B. L., Johnson C. M., and Scherer M. M. (2009) Atom exchange between aqueous Fe(II) and goethite: An Fe isotope tracer study. *Environ. Sci. Technol.* **43**, 1102–1107.

Hansel C. M., Benner S. G., and Fendorf S. (2005) Competing Fe(II)-induced mineralization pathways of ferrihydrite. *Environ. Sci. Technol.* **39**, 7147–7153.

Larese-Casanova P. and Scherer M. M. (2007) Fe(II) sorption on hematite: New insights based on spectroscopic measurements. *Environ. Sci. Technol.* **41**, 471–477.

Liger E., Charlet L., and Cappellen P. V. (1999) Surface catalysis of uranium(VI) reduction by iron(II). *Geochim. Cosmochim. Acta* **63**, 2939–2955.

Maithreepalaand R. A. and Doong R. (2004) Synergistic effect of copper ion on the reductive dechlorination of carbon tetrachloride by surface-bound Fe(II) associated with goethite. *Environ. Sci. Technol.* **38**, 260-268.

Matocha C. J., Karathanasis A. D., Rakshit S., and Wagner K. M. (2005) Reduction of copper(II) by iron(II). *J. Environ. Qual.* **34**, 1539-1546.

McArdell C., Stone A. T., and Tian J. (1998) Reaction of EDTA and related aminocarboxylate chelating agents with $Co^{III}OOH$ (heterogenite) and $Mn^{III}OOH$ (manganite). *Environ. Sci. Technol.* **32**, 2923-2930.

Nano G. V. and Strathmann T. J. (2006) Ferrous iron sorption by hydrous metal oxides. *J. Colloid Interf. Sci.* **297**, 443–454.

O'Loughlin E. J., Kelly S. D., Kemner K. M., Csencsits R., and Cook R. E. (2003a) Reduction of Ag^{I}, Au^{III}, Cu^{II}, and Hg^{II} by Fe^{II}/Fe^{III} hydroxysulfate green rust. *Chemosphere* **53**, 437–446.

O'Loughlin E. J., Kemner K. M., and Burris D. R. (2003b) Effects of Ag^{I}, Au^{III}, and Cu^{II} on the reductive dechlorination of carbon tetrachloride by green rust. *Environ. Sci. Technol.* **37**, 2905-2912.

Pedersen H. D., Postma D., Jakobsen R., and Larsen O. (2005) Fast transformation of iron oxyhydroxides by the catalytic action of aqueous Fe(II). *Geochim. Cosmochim. Acta* **69**, 3967–3977.

Postma D. (1985) Concentration of Mn and separation from Fe in sediments-I. Kinetics and stoichiometry of the reaction between biiessite and dissolved Fe(II) at 10°C. *Geochim. Cosmochim. Acta* **49**, 1023-1033.

Postma D. and Appelo C. A. J. (2000) Reduction of Mn-oxides by ferrous iron in a flow system: Column experiment and reactive transport modeling. *Geochim. Cosmochim. Acta* **64**, 1237–1247.

Roden E. E. and Emerson D. (2007) Microbial metal cycling in aquatic environments. In *Manual of Environmental Microbiology* (ed. C. J. Hurst, D. Lipson, R. Crawford, J. Garland, A. Mills, and L. D. Stezenbach), pp. 540-562. American Society for Microbiology.

Rosso K. M., Yanina S. V., Gorski C. A., Larese-Casanova P., and Scherer M. M. (2010) Connecting observations of hematite (α-Fe_2O_3) growth catalyzed by Fe(II). *Environ. Sci. Technol.* **44**, 61–67.

Schwertmann U. and Cornell R. M. (2000) *Iron oxides in the laboratory: Preparation and characterization*. Wiley-VCH.

Shannon R. D. (1976) Revised effective ionic radii and systematic studies of interatomic distances in halides and chalcogenides. *Acta. Cryst.* **A32**, 751-767.

Strathmann T. J. and Stone A. T. (2003) Mineral surface catalysis of reactions between Fe^{II} and oxime carbamate pesticides. *Geochim. Cosmochim. Acta* **67**, 2775–2791.

Williams A. G. B. and Scherer M. M. (2004) Spectroscopic evidence for Fe(II)-Fe(III) electron transfer at the iron oxide-water interface. *Environ. Sci. Technol.* **38**, 4782–4790.

Zachara J. M., Fredrickson J. K., Smith S. C., and Gassman P. L. (2001) Solubilization of Fe(III) oxide-bound trace metals by a dissimilatory Fe(III) reducing bacterium. *Geochim. Cosmochim. Acta* **65**, 75-93.

Zhang J.-W. and Nancollas G. H. (1990) Mechanisms of growth and dissolution of sparingly soluble salts. *Rev. Mineral. Geochem.* **23**, 365-396.